ELECTRICALLY INDUCED PHOTONIC TRANSITIONS IN SILICON WAVEGUIDES AND RESONATORS

A Dissertation

Presented to the Faculty of the Graduate School

of Cornell University

in Partial Fulfillment of the Requirements for the Degree of

Doctor of Philosophy

by

Lawrence Dah Ching Tzuang

August 2015

ELECTRICALLY INDUCED PHOTONIC TRANSITIONS IN SILICON WAVEGUIDES AND RESONATORS

Lawrence Dah Ching Tzuang, Ph.D.

Cornell University 2015

Photonic transition occurs in optical structures that have a time-varying refractive index. The photons experiencing a photonic transition can hop from one optical mode to another, which not only leads to a redistribution of photon numbers in each of the optical modes, but also an extra imparted non-reciprocal phase for the photons. On the other hand, photonics become increasingly important especially in the telecommunication industry because electrical interconnects have clearly reached its limits, and the demand of high performance active silicon photonics devices such as modulators and isolators become greater. In this thesis, I will show both in theory and experiment, by inducing photonic transitions using basic silicon photonics modulators, CMOS compatible high frequency modulators and isolators can be realized. In addition, I will also show in theory that the non-reciprocal phase associated with photonic transitions can be utilized to generate an effective magnetic field for light. This effective magnetic field not only adds an extra degree of control to the flow of light, but also supresses optical backscattering, which is particularly important since the silicon waveguides made nowadays are both low loss and sensitive. In this thesis, I will also show, both in theory and experiment, a pratical path to realize such an effective magnetic field using silicon resonators.

BIOGRAPHICAL SKETCH

Lawrence Dah Ching Tzuang was born on April 25, 1985 in Austin, TX. Lawrence was brought back to Taiwan soon after he was born. He was raised in Hsinchu, Taiwan, where numerous semicounductor companies were established. Graduated from National Hsinchu Senior High School, where he demonstrated a home-made radio-frequency antenna made out of cardboards and copper sheets for the school's science fair with guidance from his father. Later, Lawrence graduated from National Tsing-Hua University, where he received his M.S. degree in Materials Science and Engineering. Lawrence then joined Professor Si-Chen Lee's group at National Taiwan University to study the interaction between far-field light and surface plasmons supproted by thin metal films. After his two years of study, he earned his M.S. degree in Electronics Engineering, and he gained significant interest in optics and photonics, as well as experiences in clean room fabrication. At Cornell, he studied and performed silicon photonics research in the Cornell Nanophotonics Group led by Professor Michal Lipson. Lawrence's PhD research focuses on photonic transitions using silicon photonics to enable high frequency modulation and to break time-reversal symmetry.

To Jung Jung and Aria –

ACKNOWLEDGEMENTS

Coming to Cornell to pursue my PhD degree is one of the best decision I've ever made in my life. In the Cornell Nanophotonics Group, I have the great opportunity to work with the greatest people that help each other professionally and care each other personally. Outside of work, I enjoyed the scenes of the Finger Lakes Region, and I'm especially delighted by the kindness of people I met in Ithaca.

My deepest thanks goes to my advisor, Professor Michal Lipson, who brought me to Cornell in the first place. At the time when I was still uncertain about my decision for which school to attend, her approachable personality and the confidence level she have in her research is what really drew my attention. From the first till the last day in the group, I am constantly grateful not only for her unlimited support, but also the amount of freedom she provided in my research that made my work possible. I am also fascinated by the amount of collaboration and support with outside the group she provides, which really facilitates my research. Through numerous meetings and presentation rehearsals, I also learned how to interact with other scientists and engineers in a professional manner, which really helps me become a better all rounded photonics researcher/engineer. I also especially thank her for understanding me in a personal level, and the amount of support she provided for our family outside of work.

I want to thank my parents for their support for my PhD study. We skype and facetime a lot, which helped me went through the toughest times. My fater visited me 4 times and my mom visited me 3 times. Considering the fact that Ithaca is such a small town sitting in the middle of nowhere, this is really a remarkable feat. I am also extremely grateful for my parents support for Jung

Jung and Aria, which is the one reason I can fight through my PhD program and focus on my research. I also want to express my deepest thanks to my wife, Jung Jung. She is very supportive for my decision to come to the United States for graduate studies directly after I finished my military service, which already limited our time to being together. Also, she brought Aria to the world, and has taken great care of her, which allows me to focus more on the research. The joy and laughter she and Aria brought to the family support me to the finish line.

I would also like to thank my committee members, Professor Clifford Pollock and Professor Alex Gaeta, for their support and guidance of my research and also expanding my knowledge in the relative areas.

I also want to thank Professor Shanhui Fan from Stanford University for his support for my research project. The insights and comments he provided really help bringing my work to the top. I also want to thank Dr. Kejie Fang and Qian Lin, as we spend numerous hours on the phone discussing potential designs and physical limitations to our scheme.

I am also thankful for the members (both former and current) in the Nanophotonics Group. Dr. Mohammad Soltani gave me tremendous guidance in the very begininning of my research, as we spent countless hours looking for insights from fundamental equations. I also learned a lot of clearn room fabrication from Dr. Jaime Cardenas, Dr. Lian-Wei Luo and Dr. Hugo Lira. I'd like to thank Dr. Carl Poitras for his constant support from proposal writing to equipment acquiring for my research. I would also like to thank my peers and friends that joined the group in the same year: Dr. Yoon Ho Daniel Lee, Dr. Austin Griffith, Dr. Keven Luke, and Dr. Shreyas Shah, for sharing opinions, ideas, and knowledges. I would also like to acknowledge other group members in the group that supported my research and created inspirations: Dr. Mian

Zhang, Avik Dutt, Aseema Mohanty, Chris Phare, Steven Miller, Brian Stern, Dr. Raphael St-Gelais, Romy Fain, Moshe Zadka, Ipshita Datta, Gaurang Bhatt, Xingchen Ji, Renato Ribeiro Domenequetti, Dr. Felippe Barbosa, Dr. Mohammad Amin Tadayon, and Brian Sahnghoon Lee.

Last but not least, I want to say thank you to all my friends I met in Ithaca. This includes friends from the Taiwanese community that bring joy to the cold Ithaca winters: Kai Yuan Chen, Green, Adrian Tung, Chung Po Wang, Po Chen, Julia Chen, and many others. I also want to thank Cecilia Chapa and Jaime for hosting our rehearsals and providing delicious food.

TABLE OF CONTENTS

Biographical Sketch . . . iii
Dedication . . . iv
Acknowledgements . . . v
Table of Contents . . . viii
List of Figures . . . x

1 Introduction **1**
1.1 Silicon photonics for digital optical communications . . . 1
1.2 Silicon photonics for microwave applications . . . 3
1.3 Silicon as an electro-optical material . . . 5
1.4 Conventional modulators for silicon photonics . . . 10
1.5 Summary . . . 12

2 Photonic transitions enabled by silicon photonics **13**
2.1 Introduction to photonic transitions . . . 13
2.2 Photonic transition implemented with silicon photonics . . . 20
2.3 Photonic transition applications in silicon photonics . . . 21
2.4 Summary . . . 24

3 Microring resonators perturbed in the time domain **25**
3.1 Introduction to microring resonators . . . 25
3.2 Time-dependent perturbation of a microring resonator . . . 29
3.3 Microring resonator based modulator . . . 31
3.4 Modelling silicon microring modulators using numerical methods 32
3.5 Design and fabrication of a silicon modulator . . . 38
3.6 Summary . . . 41

4 Microring modulators operating beyond the linewidth limit **42**
4.1 The linewidth limit and the power-frequency tradeoff . . . 42
4.2 Photonic transitions between adjacent FSR modes . . . 43
4.3 Device design and fabrication . . . 48
4.4 Experimental methods . . . 51
4.5 Results and discussions . . . 54
4.6 The effect of modulator patterns and RF phases . . . 59
4.7 Summary . . . 63

5 An Effective magnetic field for light **65**
5.1 Introduction to an effective magnetic field for light . . . 65
5.2 The theory of photonic transitions enabled effective magnetic field for light . . . 66
5.3 Design and fabrication . . . 71
5.4 Experimental methods . . . 77
5.5 Results and discussions . . . 80

5.6 Summary 82

6 Non-reciprocal topological states for light **86**
6.1 Toward realizing topological states induced by an effective magnetic field for light using silicon photonics 86
6.2 Photonic transitions between microring resonators 90
6.3 Design and fabrication 99
6.4 Experimental methods and results 103
6.5 Summary 114

7 Summary and future work **116**

Bibliography **118**

LIST OF FIGURES

1.1 A typical optical communication link. 2
1.2 A typical analog optical link. This is very similar to an optical communication link, but additional processing is added inside the link to provide RF functionalities. 4
1.3 An example of a rectangular silicon waveguide with an high refractive index inner core (silicon) and a low refractive index surrounding (SiO_2). For this particular waveguide with a width of 450 nm and height of 250 nm, it supports a single TE (transverse electric) mode (shown here) and a single TM (transverse magnetic) mode (not shown). 6
1.4 Doping profiles to enable modulation in silicon waveguides: (a) P++ and N++ doping applied on the sides of the waveguide while leaving the waveguide undoped. Carriers will be injected into the waveguide when applying a forward bias (b) P++ and N++ doping applied on the sides of the waveguide and the center of the waveguide is doped into a P-N configuration. When reverse bias is applied, the depletion width in the center of the P-N junction will increase thus depleting carriers away from the waveguide core. 9
1.5 Methods of making an efficient silicon modulator: (a) a Mach-Zehnder interferometer, where the modulation of the silicon waveguide is performed on one of the interferometer arm, and (b) a ring modulator, where light is modulated inside a resonator that shifts its resonance position. 10

2.1 Depiction of the analogy between (a) atomic transitions, where atoms are excited to a higher atomic energy level through electromagnetic excitation in a two-level system and (b) photonic transitions, where photons are excited to a higher level optical mode in a photonic two-level system. 14

3.1 Illustration of the top view of two different types of microring resonators: (a) a ring resonator, and (b) a racetrack resonator. . . 26
3.2 Normalized transmission for the (a) over-coupled, and (b) undercoupled microring resonators. 28
3.3 Illustration of the operation of a microring modulator in the frequency domain. 30
3.4 Simulated cross-sectional doping profile of a silicon microring modulator from SILVACO. The concentration for both the p- and the n-doping are aimed at $1 \times 10^{18}\ 1/cm^3$. The outer P+ and N+ doping are aimed at $1 \times 10^{20}\ 1/cm^3$ 33

3.5 Simulated cross-sectional doping profile of a silicon microring modulator from SILVACO. The concentration for both the p- and the n-doping are aimed at 1×10^{18} $1/cm^3$. The outer P+ and N+ doping are aimed at 1×10^{20} $1/cm^3$ 35
3.6 Simulated output transmission of a silicon microring modulator modulated with 1, 5, 20, and 30 Gbps electrical signal. The modulator used in the simulation has a Q_L of 28,900, and it is operating near the critical coupling regime 36
3.7 (a) Simulated time evolution of the output transmission of a silicon microring modulator modulated with 2, 5, 10, and 15 GHz pure sinusoid signal. (b) The modulation depth versus different pure sinusoid modulation frequencies. The modulator used in the simulation has a Q_L of 28,900, and it is operating near the critical coupling regime 37
3.8 Illustration of the cross-section of a typical depletion mode silicon modulator. 38
3.9 Illustrations of all the critical steps to fabricate a depletion mode silicon modulator (cross-section). 40

4.1 (a) Depiction of the optical spectra of the FSRC approach (left) and the standard ring modulator (right) under a sinusoidal modulation with frequency f_M. In our FSRC approach, the FSR matches f_M, while in the standard ring modulator, FSR >> f_M. The energy diagram is also depicted in the bottom to show the photonic transitions between the adjacent FSR mdoes. (b) Illustration of the FSRC scheme. The ring has a circumference L and a segment length S subjected to refractive index modulation. . . 43
4.2 Calculation of (a) coupling coefficients between two FSR modes with indices m and n normalized to the maximum resonance frequency modulation $\Delta\omega_0$ when S = L) and (b) the modulation responses of the FSRC modulators (colored) and of the standard modulators (black and grey) with Q_L = 16,000 and Q_L = 60,000. . 47
4.3 Optical microscope image of the fabricated device. (b) Illustration of the crosssection of the modulated region 50
4.4 Illustration of the test setups for (a) measuring the modulator EO response, and (b) detecting the modulation sidebands of the silicon modulators. 52
4.5 Measured (circles) and theoretical (solid) EO response of the FSRC modulator (red) and the standard microring modulator (black). The detail of the test setup is shown in Fig. 4.4(a). 53

4.6 Measured optical spectra for (a) the FSRC modulator, and (b) the standard microring modulator under different modulation frequencies. The optical transmission spectra through the bus-waveguide is shown in the insets. Based on the insets, the loaded quality factor $Q_L \approx 16{,}000$ 55
4.7 Theoretical intrinsic power consumption for the standard silicon ring modulator (black) and the FSRC modulators (colored) with different Q_L and S 57
4.8 Illustration of a segmented microring modulator. In this particular example, there are a four modulator segments, and each segment are applied with an individual RF signal with RF phase ϕ_i. 61
4.9 Calculated $|\mu_{nm}|$ versus different number of modulator segments for the coupling between itself (black), nearest adjacent FSR (red), and second nearest adjacent FSR (green) modes. 62

5.1 (a) The imparted RF phases for photonic transitions in a photonic two-level system (the higher energy level (light grey) and the lower energy level (dark grey)). (b) A direction-dependent phase based on the photonic transition in a photonic two-level system. (c) An effective magnetic field for photons is achieved by interleaving the two photonic levels into a two-dimensional square lattice with lattice constant Λ. 68
5.2 Illustrations of (a) an atomic Ramsey interferometer, (b) a photonic Ramsey interferometer, and (c) a photonic Ramsey interferometer where the two modulators have different RF phases ϕ_L and ϕ_R. 72
5.3 Design and fabrication of a photonic Ramsey-type interferometer. Simulated mode profile for both (a) the even-mode and (b) the odd-mode which coexist in a silicon coupled-waveguides structure. (c) Cross-sectional view of the coupled-waveguides. A set of PN and NP diodes is doped in this coupled-waveguides to modulate the refractive index. (d) Top view of the carrier density (N) distribution of the coupled-waveguides along the x-axis (the slab is omitted for simplicity). The width of the depletion region (grey) changes over time as a sinusoidal signal is applied to the diodes. The applied sinusoid voltage (V) is shown in red. (e) Illustration of a photonic Ramsey-type interferometer implemented by a silicon coupled-waveguides structure. The insets show the microscope image and the simulated light transmission through a pair of multi-mode interference devices located at the outer ends of the interferomter. 75

5.4 The dispersion relation of the even and the odd mode in a silicon coupled-waveguides structure. (a) Simulation of the frequency separation of even- and odd-mode for the waveguide geometry defined in Fig. 5.3(c). (b) A depiction of the dispersion curves for both even (blue) and odd (red) modes at the RF modulation regions (solid) and at the middle modulation-free region (dashed). The modulation frequency f_M ideally should match the frequency separation between the two modes (Δf). 77
5.5 Experimental setup that measures the non-reciprocity and the interference fringes for the photonic Ramsey-type interferometers. (a) The two signal generators are synchronized to ensure correlated phase between the two RF signals, and these signals are monitored through the oscilloscope. Fibers connecting to point A and B from the laser and the photodetector (PD) are interchangeable to measure the forward and backward light transmission without moving the setup. (b) Setup configured to obtain higher RF power using an RF amplifier. 78
5.6 (a) Examples of the measured (circles, normalized to the maximum curve fitted value) and theoretically fitted (solid lines) optical transmission for light traveling from left to right (L $\rightarrow$ R, blue) and right to left ($R \rightarrow L$, red) for devices with different L_f as a function of the phase difference between the two signals applied to the modulators ($\Delta\phi = \phi_L - \phi_R$). The error bar represents one standard deviation from the measurement mean resulting from optical alignment fluctuation. (b) Measured (circles) and theoretical (solid) difference between the $\Delta\phi$ when the transmission is maximum for $L \rightarrow R$ ($\Delta\phi_{L\rightarrow R}$) and $R \rightarrow L$ ($\Delta\phi_{R\rightarrow L}$) versus different L_f values. The gray region indicates the error of the theory curve when a 5 % process variation is introduced. (c) Measured and theoretically fitted optical transmission for light traveling from left to right (blue) and right to left (red) for L_f = 350 μm with increased population in the odd mode Podd (shown as percentages) achieved by increasing the applied RF power. . . 84
5.7 Wavelength dependence of the interference effect for the photonic Ramsey-type interferometer. (a) Measured (gray circles, normalized to the maximum curve fitted value) and theoretically fitted (solid) optical transmission of light traveling from left to right and from right to left versus $\Delta\phi$ for different laser wavelengths of 1560, 1565, 1570, and 1575 nm with L_f = 350 μm. (b) Theoretical (dashed line) and measured (circles) phase of the fringes for both $L \rightarrow R$ and $R \rightarrow L$ with varying wavelength. . . . 85

6.1 (a) Examples of geometric disorders and (b) sidewall roughness induced scattering loss contributed by fabrication imperfections. 87

6.2 Examples of different effective magnetic field distributions (green area) all achieved by simply changing the phases (ϕ) of the RF modulations that are responsible for the photonic transitions between adjacent lattce sites. Each lattice site is represented by one of the two photonic levels (blue: higher energy level, purple: lower energy level). 89
6.3 (a) Illustration of one unit cell of Fig. 6.2. (b)(c) Coupled-waveguides-resonator: Non-reciprocal phase ring resonator that supports an even and an odd mode. (b) Light is incident on the left bus waveguide, which couples only to the even mode of the coupled-waveguides-resonator. The dynamic modulation in the ring induces coupling from the even mode to the odd mode of the coupled-waveguides-resonator, and the odd mode couples out to the right waveguide and the phase of the modulation is imprinted on the output. Note that the even mode cannot couple to the right waveguide. (c) Similarly, when going from right to left, incident light couples to the antisymmetric mode, and the dynamic modulation couples the odd mode to the even mode, which then couples out to the left waveguide. The opposite phase is imprinted on the output from right to left. 91
6.4 (a)-(c) Illustration of different coupled-waveguide-resonator schemes, and examples of (d) broad and (e) narrow linewidth relative to the frequency separation between the two optical modes. 94
6.5 (a) Example spectrum of a CWR shown in Fig. 6.3 and 6.4(a). The blue curves correspond to the even mode resonances, and the purple curves correspond to the odd mode resonances. (b) The dispersion curves of the even and the odd modes in the CWR. The dashed lines corresponds to the resonance condition of the modes (blue for the even mode and purple for the odd mode.) . 96
6.6 (a) Definitions of light amplitudes (a for even mode and b for odd mode) at various part of a CWR resonator unit cell, and example spectra (blue for the even mode and purple for the odd mode) when the resonance frequency detuning between the two modes are (a) negligible and (b) large. 98
6.7 The construction of a photonic topological insulator using the proposed coupled-waveguide-resonators shown in Fig. 6.3. . . . 100

6.8 (a) The transmission from the blue waveguide into the CWR for different gap widths, and the transmission from the purple waveguide into the CWR for different gap widths. (b) The cross-section of the CWR at the waveguide-CWR coupling region. Here the gap is defined as the distance between the edge of the CWR and the edge of the blue (or purple) waveguide. The mode profile of the even and the odd mode for the CWR are also shown. 101
6.9 (a) The simulated frequency difference between the even and the odd mode in a coupled-waveguide structure. (b) The simulated amplitude coupling and loss (1/m) for the modulation region where the coupled-waveguide is doped into a PN diode and operating with the depletion mode. 102
6.10 (a) The proposed CWR structure and SEM snapshots of the coupling region and the modulation region. (b) Optical microscope image of a CWR without doping and metal connections. The inset shows the coupling region. (c) The transmission spectra of the CWR when coupling through the left (even mode, blue) and the right (odd mode, purple) waveguides. 104
6.11 (a) Microscope image of an active CWR. (b) The test setup for measuring the transmission of the through and the drop ports of an active CWR. 106
6.12 The optical power transmitted through the CWR (a) through and (b) drop ports. 108
6.13 The experimental setup for the beat note measurement of a single CWR resonator. 110
6.14 The measured transmission spectra of the through port (black, transmission from port 3 to port 4), the drop port beat note (blue, transmission from port 3 to port 1), and the drop port beat note when chip input is reversed (yellow, transmission from port 1 to port 3) for l_c = (a) 11 μm, (b) 22 μm, and 33 μm. The right hand side of the figures show the estimated transmission and theoretical curve fits (solid). 113
6.15 Theoretical calculation of the drop port transmission with different waveguide coupling strength ($\sqrt{1-t^2}$) and mode coupling strength (C = $|\kappa| \times l_{mod}$) of a CWR for RTL = (a) 65 %, (b) 32 %, and (c) 16 %. The red dot corresponds to the case for the CWR in Fig. 6.14(a) with negligible detuning between the resonance wavelengths of the even and the odd mode. The bottom figures are the simulated transmission in the through (blue) and the drop (purple) ports for the condition set at the red dots. 114

CHAPTER 1

INTRODUCTION

1.1 Silicon photonics for digital optical communications

Silicon photonics [1–4] have become increasingly important in the photonics industry [5, 6] because it can be used as an integrted platform that provides scalable high bandwidth optical networks. Recent years, with the soaring demand of bandwidth (information transmitted per unit time) worldwide, thanks for the increasing amount of online social activities, video streaming, cloud services, online businesses, etc., researchers in both the academia and the industry are searching for ways to meet the satisfied performance without sacrificing cost and volume needs. Optical communication becomes a viable option because of the success of low loss optical fibers and the unlimited bandwidth (the optical frequencies are > 100,000 times higher than the radio-frequencies (RF)) it provides. In few years ago, the photonic industry are mostly building devices for long-haul telecom links based on III-V materials [7,8], which are incredibly versatile materials that can be used to not only make lasers, but also provide active controls and guide light efficiently. In contrast, silicon photonics is a relatively new area. It attracts the attention of the industry mainly because it allows co-design of optical devices using silicon with electronic components. In addition, it is cost effective because of the use of larger than 12-inch wafers instead of standard 2 inch standard III-V wafer. Furthermore, the mature CMOS manufacture capabilities and silicon-compatible packaging makes silicon photonics the ideal candidate to meet the cost and volume needs for future datacenter interconnects with extremely dense I/O (input and output) data ports.

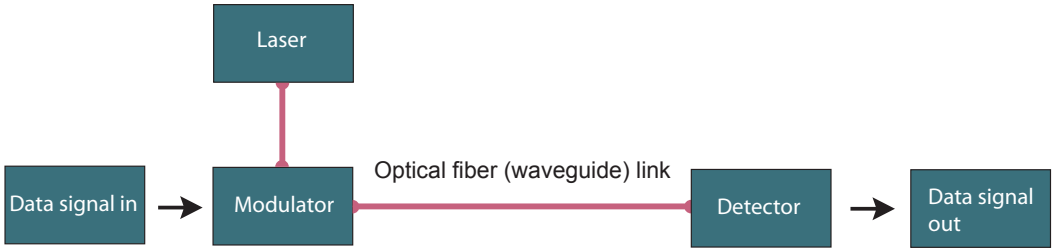

Figure 1.1: A typical optical communication link.

In addition to datacom applications, for future chip-to-chip interconnects, silicon photonics addresses the fundamental bottleneck for electrical interconnects as they are limited to power (reach), bandwidth, and crosstalk. With the ability to place optical components right next to the electrical circuitry, silicon photonics provide lower electrical loss and better on-chip integration [9–13]. Another major challenge for conventional electrical interconnects is the crosstalk. Because the electrical signal have much larger wavelength than optics, generally, more overlap between the modes in adjacent electrical wires is expected for the same interconnect density. Adding up the factors of crosstalk and power loss of electrical interconnects, silicon photonics, which can be integrated directly on a single chip with electronics, becomes the potential solution for chip-to-chip interconnects.

One of the most critical silicon photonic components to construct a successful digital communication link is the modulator and the detector. As shown in the simplified optical link in Fig. 1.1, data in the form of electrical signals are transformed into optical signals via a modulator. Then, the signal is sent out through optical fibers or waveguides that reaches the detector on the other end of the link. The detector then brings the information in the optical domain back to the electrical domain, and then the data signal is read in the form of electrical

signals. Coherent light that carries the information can be created either on-chip or off-chip by an external laser and fed into the link. In reality, the modulator building block in this drawing consists of an array of modulators, each with a dedicated operation wavelength to achieve wavelength-division multiplexing (WDM) to maximize the spectral efficiency of the optical link. Ideally, the modulator and detector have both high EO (electrical to optical) and OE (optical to electrical) efficiency and low insertion loss to minimize the total power consumption as well as maintain signal integrity. Part of this thesis will be discussing the theory and design of silicon EO modulators.

1.2 Silicon photonics for microwave applications

Microwave photonics, or RF photonics, are optoelectronic devices or systems that processes microwave signals [14–20]. These signals are typically narrow bandwidth analog signals and they are carried by high RF frequency carriers. The processes include functionalities such as time delay, communication, phase shifting, filtering, frequency conversion, etc. RF photonics has gained a lot of attention mainly because the attenuation of electrical interconnect increases dramatically with increasing carrier frequency. Another huge advantage for merging RF and optics is to process analog signal in high bandwidth optical fibers, without using slow and complicated electronics. In addition, photonics can also be used to generate high frequency RF signals through beating two coherent optical sources.

In the heart of RF photonics, again, lies the EO and OE components, namely the modulator and the detector, respectively. Fig. 1.2 shows a block diagram

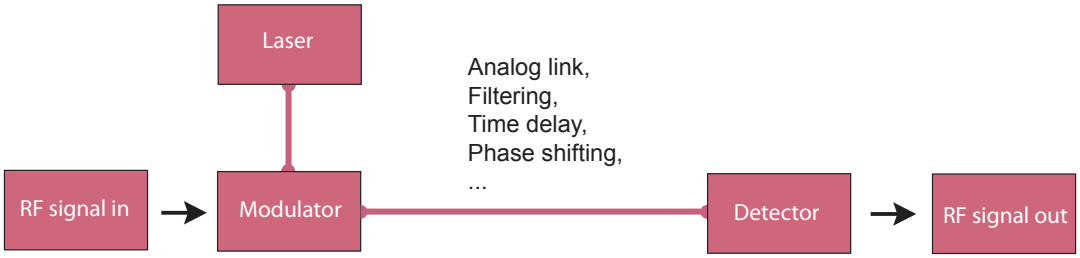

Figure 1.2: A typical analog optical link. This is very similar to an optical communication link, but additional processing is added inside the link to provide RF functionalities.

of a typical analog optical link. It looks very similar to the digital communication optical links, other than RF specific functionalities can be added between the modulator and the detector. Although the bandwidth for analog signals is generally narrow, the modulator and the detector are expected to work at very high carrier frequencies to further increase the data bandwidth. These frequencies include the recently released 60 GHz frequency band (1.25 Gb/s data rate using the 60- or the 70-GHz band have been demonstrated [21, 22]) and much higher than the 100 GHz frequency band (10 Gb/s data rate have been demonstrated [23]). The gain of the link improves the signal-to-noise ratio (SNR), which means the EO and OE conversion efficiency is critical. In addition, the fidelity of RF signals after being transmitted through a modulator is characterized through linearity measurements, and there are recent progresses on dealing with the non-linear nature of common silicon modulators [24–28], which is beyond the scope of this thesis. In this thesis, I will focus on the theory and design of silicon EO modulators to operate at very high carrier frequencies.

1.3 Silicon as an electro-optical material

Silicon is an ideal candidate for the applications mentioned in the previous two sections becuase it has great optical properties when operated around the telecom wavelength (around 1550 nm). If we compare the refractive index of silicon to other low loss CMOS compatible materials such SiO_2 as and Si_3N_4, it has the highest refractive index at 3.45 (SiO_2: 1.46, Si_3N_4: 1.99). This indicates that silicon can confine light better in the waveguide, which not only leads to smaller waveguide crosstalk, which is important in compact and dense on-chip interconnect networks, but also more interaction between light and silicon, which means any optical effect in silicon is greater. For example, as shown in Fig. 1.3, for a typical silicon waveguide of width 450 nm and height 250 nm surronded by low refractive index SiO_2, the light is single mode (transverse-electric (TE) mode), and it is mostly confined in the silicon core, and much less in the outer SiO_2 cladding (confinement factor is about 90 %).

The silicon waveguide losses are quite low. For deeply etched silicon waveguides, the reported numbers are between 1 dB/cm to 2 dB/cm [24, 29–33], and they are generally enough for most applications. Ridge waveguides with relatively large widths of 1 - 5 μm exhibit lower loss down to 0.3 dB/cm [34–38] but limited in the minimum bending radius. The loss is mainly contributed from the roughness along the waveguide sidewalls (due to fabrication) instead of intrinsic absorption. Recently, an etchless process is developed to make silicon waveguides without using any etch processes [39–41], so that the waveguide boundaries are untouched during the fabrication process. While preserving high optical confinement, this process also leads to a very smooth sidewall, and the loss measured is very low at about 0.3 dB/cm. These waveguides are great

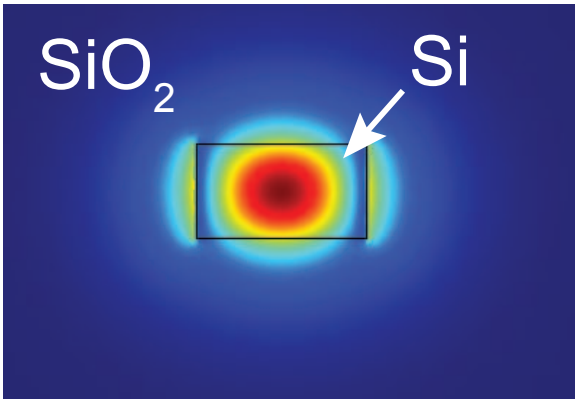

Figure 1.3: An example of a rectangular silicon waveguide with an high refractive index inner core (silicon) and a low refractive index surrounding (SiO_2). For this particular waveguide with a width of 450 nm and height of 250 nm, it supports a single TE (transverse electric) mode (shown here) and a single TM (transverse magnetic) mode (not shown).

for exploring non-linear effects in silicon (single crystalline silicon has a large $\chi^{(3)}$ coefficient) in the mid-infrared (IR) regime (silicon has much lower loss in the mid-IR) [42]. This indicates that silicon can be a very versatile photonics platform.

The common methods to change the refractive index of silicon are the following two ways: thermal-optic effect [43] and carrier dispersion effect [44]. Thermal-optic effect is a temperature dependent change on the material refractive index. The thermal optic coefficient for silicon is $dn/dT = 1.8 \times 10^{-4}$ at room temperature. The thermal response is usually slow in the order of microseconds. Therefore, it is not ideal for modulator designs, which requires > GHz modulation. However, it is suitable for applications such as switching [45] and controlling the resonance frequency of optical resonators [46], where high frequency tuning is not necessary. The other way of changing the refractive index

of silicon is through carrier dispersion effect. Carrier dispersion effect is a carrier density dependent change on the refractive index of silicon. The two main contributions to this effect is through the combination of plasma dispersion and bandgap shrinkage. For the plasma dispersion, the refractive index change is resulted from the shift in the plasma frequency when removing or injecting free carriers. For the bandgap shrinkage effect, it is resulted from the electron-electron or hole-hole interaction that causes a splitting in the dopng-induced energy levels especially when the free carrier density is high. The carrier dispersion effect is frequently used in silicon modulators in conjunction with PN diodes [47–59]. Here I want to note that Si_3N_4 only have thermal optic effect, but no carrier dispersion effect. In addition, it has both lower optical confinement (hence the heater are placed furtheraway from the waveguide) and thermo-optic coefficient (about 4.7×10^{-5} [60]), therefore, tuning Si_3N_4 is much less efficient than silicon. However, due to its attractive nonlinear properties and low optical loss capabilities Si_3N_4 waveguides [61–65] provides, three-dimensional hybrid scheme (Si_3N_4 and Si) has been explored [66] to bring efficient active controls for Si_3N_4 waveguides.

The carrier dispersion effect in silicon is very well documented for carrier densities below N = 1e19 $1/cm^3$ [44]. Based on Ref. [44], the generally accepted empirical equations for the change in loss and refractive index versus N are shown in the following:

$$\Delta n = -(8.8 \times 10^{-22} \Delta N_e + 8.5 \times 10^{-18} \Delta N_h^{0.8}), \tag{1.1}$$

$$\Delta \alpha = 8.5 \times 10^{-18} \Delta N_e + 6 \times 10^{-18} \Delta N_h \tag{1.2}$$

Immediately from Eqs. (1.1) and (1.2), we see that the change of refractive index

through the carrier dispersion effect must be associated with a change in loss. This leads to a significant conclusion: the ratio between the change in the refractive index and the increase in optical loss is a fixed constant. In other words, there will be inevitable loss when attempting to change the refractive index in silicon. This is a fundamental drawback of using silicon to modulate light as I will explain more later in this thesis. Another important thing we can derive from Eqs. (1.1) and (1.2) is that the change of refractive index is stronger for holes than electrons. This result means that the doping profile in the waveguide needs to be engineered to acheive maximum modulation efficiency [67].

The speed of the silicon refractive index change through a injection mode modulator is intrinsically limited by the minority carrier recombination lifetime [68]. By injecting carriers uniformly into the waveguide, the refractive index changes according to Eqs. (1) and (2). This is done by dopoing the waveguide into a P-I-N configuration, where I is the intrinsic region, and apply a forward bias accross the P-I-N diode (we call it injection mode [47, 48]) as shown in Fig. 1.4(a). Note that now the rectangular silicon waveguide sits on a thin silicon slab. This slab allows electrons and holes from the doping heavy P++ and N++ region to access the intrinsic waveguide. The minority carrier lifetime in a silicon waveguide has been reported to be 3 ns, and it is greatly reduced down to 12.2 ps when applying a negative bias voltage that quickly sweeps away the carriers [68]. This lifetime limits the modulation speed using injection mode to xx because the rise time is not fast enough. However, pre-emphasis techniques has been explored and > 15 Gbps modulation [58] is possible. For etchless waveguides, the carrier lifetime is even longer due to the fact that minimal electron trap sites exist along the pristine boundaries between silicon and the cladding material (SiO_2).

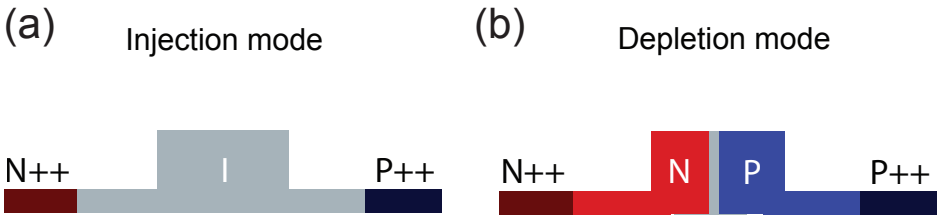

Figure 1.4: Doping profiles to enable modulation in silicon waveguides: (a) P++ and N++ doping applied on the sides of the waveguide while leaving the waveguide undoped. Carriers will be injected into the waveguide when applying a forward bias (b) P++ and N++ doping applied on the sides of the waveguide and the center of the waveguide is doped into a P-N configuration. When reverse bias is applied, the depletion width in the center of the P-N junction will increase thus depleting carriers away from the waveguide core.

The limitation of the carrier lifetime can be bypassed by using a depletion mode modulator. As shown in Fig. 1.4(b), this is done by pre-dope the waveguide into a P-N diode with its junction near the center of the waveguide (we call it the depletion mode). As a reverse bias voltage is applied, the junction depletion width opens, therefore locally changes the refractive index in the vicinity of the P-N junction. This phenomenon is purely a field effect, and the speed is limited only by the movement of the majority carriers, and no carrier lifetime limit is imposed. This method is the mainstream way to modulate silicon at a speed much higher than a few GHz [53, 54]. Speeds up to 40 and 50 GHz has been reported [69, 70], and it is only limited by the overall RC constant. However, one drawback of this method is that the modulation efficiency is much lower than that of the injection mode due to less overlap between the local refractive index change and the optical mode in the waveguide. In addition, because pre-doping is required, the waveguide loss is intrinsically higher.

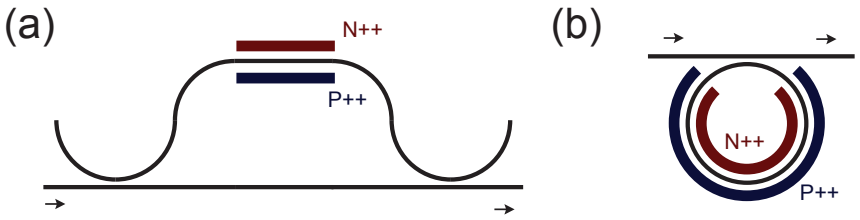

Figure 1.5: Methods of making an efficient silicon modulator: (a) a Mach-Zehnder interferometer, where the modulation of the silicon waveguide is performed on one of the interferometer arm, and (b) a ring modulator, where light is modulated inside a resonator that shifts its resonance position.

1.4 Conventional modulators for silicon photonics

The two mainstream schemes to build an efficient silicon modulator are the Mach-Zehnder interferometer (MZI) modulators and the resonator-based modulators. Both of the two methods typically use depletion mode P-N diodes integrated in the waveguide to provide the refractive index change to obtain high speed operation. The reason for this is that the bit rate of digital communication is usually larger than 10 Gbps (Giga bits per second), which is beyond the speed limit of injection mode modulators (discussed in Section 1.3). In addition, unlike III-V materials (direct bandgap) where absorption based modulators are the main technology, carrier dispersion effect for silicon is relatively weak (the absorption change is little). Therefore, efficient modulation in silicon is achieved by inserting P-N diodes in silicon interferometers or resonators.

Mach-Zehnder interferometer modulator is commonly used in silicon photonic chips in the industry [51,70] mainly because of its broad bandwidth and robustness against local temperature changes. The operation principle of a MZI modulator is shown in Fig. 1.5. Light is first split into two arms through a di-

rectional coupler, and refractive index modulation (as discussed in Section 1.3) is performed on only one arm that shifts its phase (or two arms in a push-pull fashion [71]). Then there is a second directional coupler that recombines the light in the two arms, and the net result is a spectral interference pattern for the output light. The period of the spectral interference pattern changes as the amount of phase shift applied on that one arm changes. This causes a change in the optical transmission for a particular laser wavelength. The state of the art silicon MZI modulator can be operated at frequencies as high as > 50 Gb/s [70] with a phase shifter length in the range of a few millimeters and a driving voltage of a few volts. The main limitation is the RF loss due to the long electrode length.

The other modulator scheme is to use microresonators. Microresonators are optical cavities that are engineered and fabricated on the integrated platform. It can be simply a Fabry-Perot (FP) resonator [72], a photonic crystal resonator [73], microdisks [74], or a circular waveguide ring (microring) [47,75]. In this thesis, I will be focusing on the microring resonators, as it has the following benefits: easier electrical access and fabrication, low optical loss, and small device footprint. One example of such a device is shown in Fig. 1.5(b). The main advantage of using microring resonators is that the interaction between light and the modulated region (as discussed in section 1.3) is enhanced, because light travels in multiple round trips before it escapes the resonator. The net result is a shift in the resonance position, and the optical transmission is subsequently changed. In this scheme, the modulation region can be designed much shorter than MZI modulators along with a much higher modulation efficiency. For example, the micrdisk modulator can have a disk diameter as small as 2 μm [76], and it is only limited by the radiation loss. The drawbacks of

resonator-based modulators are the extra requirement of stabilizing the resonance positions (thermal shifts or fabrication errors), thus adding more power to the total power consumption in a WDM optical link. More details about microrings and microring modulators will be further discussed in Chapter 2.

1.5 Summary

In this Chapter, the general overview of silicon photonics and its main applications are discussed. Then, the electro-optic effect in silicon and how this effect enables critical devices such as a silicon modulator are introduced. Various silicon modulator design schemes as well as their pros and cons are subsequently discussed. In the next chapter, I will discuss the physics of photonic transitions and how to induce this effect using silicon photonics

CHAPTER 2

PHOTONIC TRANSITIONS ENABLED BY SILICON PHOTONICS

2.1 Introduction to photonic transitions

Photonic transition is a physical phenomenon where photons couple from one discrete optical mode to another in an optical structure when subjected to refractive index perturbation [77–84]. What makes this phenomenon so interesting to researchers is its direct analogy to atom physics. In atom physics, atoms can have multiple energy levels, and it is well known that the electrons can *jump* between atomic energy levels by absorbing photons, causing a transition from a lower energy atom state to a higher energy atom state (see Fig. 2.1(a)). This process is reciprocal: by emitting photons, electrons can return from a higher energy state back to a lower energy state. To enable such atomic transitions, both energy and momentum have to be conserved. For example, the photon absorbed (or emitted) is matched to the frequency separation between the atomic states, and the photon momentum is also transferred to or removed from the atom during such atomic transitions. Such a transition happens because the electromagnetic radiation induces a dipole moment and introduces an oscillatory perturbation to the electron position. This perturbation will cause the electron to couple into other atomic eigenstates (levels). Therefore, for such transitions to occur, and if the energy and momentum should match as described above, the overlap integral (or the matrix element M_{fi}) of the wavefunctions that represent the corresponding initial ($|\psi_i\rangle$) and final atomic states ($\left|\psi_f\right\rangle$) has to be non-zero:

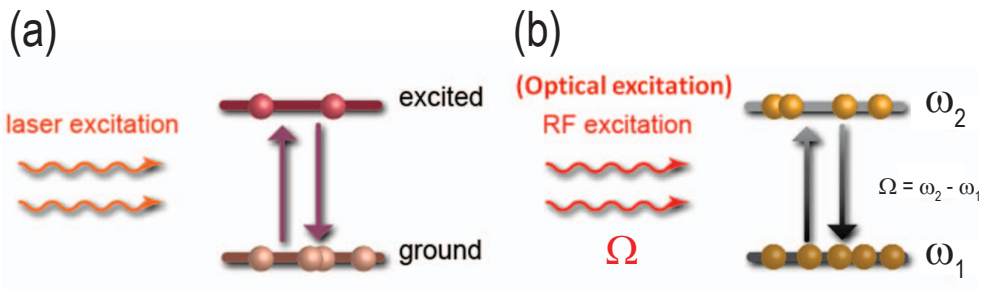

Figure 2.1: Depiction of the analogy between (a) atomic transitions, where atoms are excited to a higher atomic energy level through electromagnetic excitation in a two-level system and (b) photonic transitions, where photons are excited to a higher level optical mode in a photonic two-level system.

$$M_{fi} = \int_{\infty} \Psi_i^* V \Psi_f \, dv \neq 0 \tag{2.1}$$

where V is the dipole potential operator. Eq. 2.1 is also known as the transition rate or the Rabi oscillation frequency between the initial and final states. The non-zero transition, or say *coupling*, between the initial and final states also implies that these two states are now indistinquishable, and the atom will be oscillating between the two atomic states known as the Rabi oscillation [85].

The direct analogy between photonic transitions and atomic transitions can be found in a simple photonic two-level system. As shown in Fig. 2.1(b), we can arbitrarily create a photonic two level system by creating an optical structure that supports two optical modes. These modes can be of any eigensolutions for that particular optical structure. For example, it can be any two different spatial modes (including different polarizations) in a waveguide (or a photonic crystal) or two different round trip mode of an optical resonator. These modes could be continuous in photon energy ($\hbar\omega_{1(2)}$, where $\omega = 2\pi c/\lambda$ and c is the speed of light = 3e8 m/s) for different optical wavelengths (λ). However, but for any given

$\overrightarrow{k}$ vector ($2\pi/\lambda$), one can always find that the two chosen modes are separated in frequency equals to $\Delta E/\hbar$. Such a photonic two level systems resembles the atomic two level system in a way that the photons interact with another electromagnetic wave with frequency Ω (its photon energy $\hbar\Omega = \hbar\omega_2 - \hbar\omega_1$) to induce transitions either from the lower photonic level to the higher photonic level or vice versa. At first glance, it seems impossible for the photons that are in either of these two levels to interact directly with externally injected photons with a completely different optical frequency without using non-linear optical wave-mixing. However, this interaction can be created *indirectly*. As demonstrated in Ref. [86], by shining a visible pulsed laser on a silicon microcavity, the refractive index in the microcavity is perturbed, and light is coupled to other neighboring resonance modes (photonic states). The problem with this approach is that it requires precise free-space optical alignment for the injected photons to imping on the exact location, and either a pulsed laser or a modulator in the front end is required. As shown in Fig. 2.1(b), an alternative approach is to inject RF photons in the form of electrical signals that changes the refractive index of the optical structure that contains the photonic two-level system [78, 81]. In this case, that optical structure has to be an electro-optical device. The RF photons are chosen because they have much lower frequencies to match the speed of which the electro-optical device can respond to (usually a few to few tens of GHz). The photonic transition rate (or say the coupling coefficient) between the two optical modes resulted from time-dependent refractive index perturbation (equivalent to $\Delta\epsilon$) can be derived from the Maxwells equation:

$$\nabla \times E = -\mu_0 \frac{\partial H}{\partial t} \tag{2.2}$$

$$\nabla \times H = \epsilon_0 \frac{\partial(\bar{\epsilon} + \Delta\epsilon)E}{\partial t}, \tag{2.3}$$

here E (H) is the total electric (magnetic) field in this photonic two-level system, ϵ_0 (μ_0) is the vacuum permittivity (permeability), and $\bar{\epsilon}$ is the average (bias point) of the $\Delta\epsilon$. The $\Delta\epsilon$ term describes the sinusoidal change in the relative dielectric constant:

$$\Delta\epsilon = \delta\epsilon(x,y)cos(\Omega t - qz + \varphi) = \frac{1}{2}\delta\epsilon(x,y)[e^{j\Omega t - qz + \varphi} + e^{-j\Omega t - qz + \varphi}], \tag{2.4}$$

and the total Electric field can be written as:

$$E = a_1(z)E_1(x,y)e^{-jk_1 z + j\omega_1 t} + a_2(z)E_2(x,y)e^{-jk_2 z + j\omega_2 t}. \tag{2.5}$$

In Eq. (2.4), q is the $\overrightarrow{k}$ for the RF photons, and φ is the phase (the time or space origin) of this modulation. Eq. 2.4 assumes that the waveguide cross-sectional (in the x-y plane) dielectric constant is perturbed uniformly along the z-axis. The amplitude of this dielectric constant perturbation is $\delta\epsilon(x,y)$. In Eq. (2.5), $E_{1(2)}$ is the cross-sectional electric field of mode 1(2), $a_{1(2)}(z)$ is the amplitude of the electric field contributed from mode 1(2), $k_{1(2)}$ is the $\overrightarrow{k}$ vector of mode 1(2), and $\omega_{1(2)}$ is the frequency of mode 1(2). By plugging Eq. (2.3) into (2.2) yields:

$$\triangledown \times \triangledown \times E = -\mu_0\epsilon_0\frac{\partial^2}{\partial t^2}[\bar{\epsilon}E + \frac{1}{2}\delta\epsilon(x,y)(e^{j(\Omega t - qz + \varphi)} + e^{-j(\Omega t - qz + \varphi)})E]. \tag{2.6}$$

Now by plugging Eq. (2.5) into both the left- and the right-hand side of Eq. (2.6), assuming that $\Omega << \omega_{1(2)}$, eliminating the unperturbed terms, and assuming a slowly varying $a_1(z)$ and $a_2(z)$, we are left with:

$$\begin{aligned} &2jk_1\frac{\partial a_1(z)}{\partial z}e^{-jk_1 z + j\omega_1 t}E_1 + 2jk_2\frac{\partial a_2(z)}{\partial z}e^{-jk_2 z + j\omega_2 t}E_2 \\ &= \frac{1}{2}\omega^2\mu_0\epsilon_0\delta(x,y)(a_1(z)E_1e^{-j(k_1+q)z}e^{j(\omega_1+\Omega)t + j\varphi} + c.c. + a_2(z)E_2e^{-j(k_2+q)z}e^{j(\omega_2+\Omega)t + j\varphi} + c.c.) \end{aligned} \tag{2.7}$$

Then, we multiply both sides of Eq. (2.7) by E_1^*, integrate it over the entire x-y plane, and rearrange the coefficients, we get:

$$\begin{aligned}\frac{da_1(z)}{dz} &= -j\kappa_{11}a_1(z)cos(\Omega t + qz + \varphi) \\ &- j\kappa_{12}a_2(z)(e^{j(\omega_2-\omega_1+\Omega)t+j\varphi}e^{-j(k_2-k_1+q)z} + e^{j(\omega_2-\omega_1-\Omega)t-j\varphi}e^{-j(k_2-k_1-q)z}),\end{aligned} \tag{2.8}$$

where

$$\kappa_{11} = \frac{\omega^2\mu_0\epsilon_0}{2k_1}\frac{\iint_\infty \delta(x,y)E_1E_1^*\,dx\,dy}{\iint_\infty E_1E_1^*\,dx\,dy}, \tag{2.9}$$

$$\kappa_{12} = \frac{\omega^2\mu_0\epsilon_0}{4k_1}\frac{\iint_\infty \delta(x,y)E_2E_1^*\,dx\,dy}{\iint_\infty E_1E_1^*\,dx\,dy}. \tag{2.10}$$

If we further assume that the mode 1 and 2 have the same wavevector and $\delta(x,y)$ is a harmonic modulation, then $k_1 = k_2 = k$ and $q = 0$, Eq. (2.8) is simplified to:

$$\frac{da_1(z)}{dz} = -j\kappa_{11}a_1(z)cos(\Omega t + \varphi) - j\kappa_{12}a_2(z)(e^{j(\omega_2-\omega_1+\Omega)t+j\varphi} + e^{j(\omega_2-\omega_1-\Omega)t-j\varphi}). \tag{2.11}$$

Similary, again from Eq. (2.7), we multiply both sides by E_2^*, then integrate it over the entire x-y plane and rearrange the coefficients, we get:

$$\frac{da_2(z)}{dz} = -j\kappa_{21}a_1(z)(e^{j(\omega_1-\omega_2+\Omega)t+j\varphi} + e^{j(\omega_1-\omega_2-\Omega)t-j\varphi}) - j\kappa_{22}a_2(z)cos(\Omega t + \varphi). \tag{2.12}$$

where

$$\kappa_{22} = \frac{\omega^2\mu_0\epsilon_0}{2k_1}\frac{\iint_\infty \delta(x,y)E_2E_2^*\,dx\,dy}{\iint_\infty E_2E_2^*\,dx\,dy}, \tag{2.13}$$

$$\kappa_{21} = \frac{\omega^2\mu_0\epsilon_0}{4k_1}\frac{\iint_\infty \delta(x,y)E_1E_2^*\,dx\,dy}{\iint_\infty E_2E_2^*\,dx\,dy}. \tag{2.14}$$

Note that $\omega \approx \omega_{1(2)}$. The coupling terms κ_{11} and κ_{22} are the self-coupling terms, which simply means that the phase or loss for light are constantly changing due

to the perturbation. Therefore, we can drop the terms associated with κ_{11} and κ_{22} due to their negligible effect on the whole physical picture. Now if we assume that Ω, the frequency of the perturbation, matches the frequency separation between the two modes, namely, $\Omega = \omega_2 - \omega_1$, then Eqs. (2.11) and (2.12) becomes:

$$\frac{da_1(z)}{dz} = -j\kappa_{12}a_2(z)(e^{j(2\Omega)t}e^{j\varphi} + e^{-j\varphi}), \tag{2.15}$$

$$\frac{da_2(z)}{dz} = -j\kappa_{21}a_1(z)(e^{j\varphi} + e^{j(-2\Omega)t}e^{-j\varphi}). \tag{2.16}$$

We can now define $\kappa_{12} = \kappa_{21}^* = \kappa$. Note that Eqs (2.15) and (2.16) are exactly the form of coupled mode equations, meaning that mode 1 and mode 2 constantly exchange energy at the rate of κ, and κ is very similar to the form of Eq. (2.1). For the case where $2\Omega >> \kappa \times c/n_g$, where n_g is the group index of the optical modes, the exponential terms in Eqs. (2.15) and (2.16) oscillates very fast that it will not interfere with the power oscillation between a_1 and a_2. Therefore, we can drop those fast oscillation terms (this method is usually refered to as the rotating wave approximation):

$$\frac{da_1(z)}{dz} = -j\kappa a_2(z)e^{-j\varphi}, \tag{2.17}$$

$$\frac{da_2(z)}{dz} = -j\kappa^* a_1(z)e^{j\varphi}. \tag{2.18}$$

Eqs. (2.17) and (2.18) means that if we first put photons in the optical mode 1, over a period of time, depending on the rate of κ, some portion of the photons will be coupled into the optical mode 2. This happens only because the RF wave perturbs this photonic two level system in a way that both the energy and momentum is conserved. In direct analogous terms, κ is the Rabi oscillation frequency for this photonic two-level system. The solution of the coupled

equations can be expressed by a transfer matrix T that relates the a_1 and a_2 at positions z and $z = 0$:

$$T = \begin{pmatrix} cos(|\kappa|z) & jsin(|\kappa|z)e^{-j\varphi} \\ jsin(|\kappa|z)e^{j\varphi} & cos(|\kappa|z) \end{pmatrix}, \tag{2.19}$$

where

$$\begin{pmatrix} a_1(z) \\ a_2(z) \end{pmatrix} = T \times \begin{pmatrix} a_1(0) \\ a_2(0) \end{pmatrix}. \tag{2.20}$$

It is clear from Eq. (2.19) that the amplitude of light in the two optical modes fluctuates sinusoidally, but out of phase with each other, with frequency $|\kappa|$. If photons are initially residing in mode 1, at $z = \pi/(2 \times |\kappa|)$, all the photons will be coupled into mode 2. Here, I want to point out that there is an additional RF phase φ imparted on the photons that are experiencing the photonic transitions as implied in Eq. (2.19).

The photonic transitions break time-reversal symmetry. The fundamental reason why photonic transitions break time-reversal symmetry is revealed by looking at the perturbation term for either when the dielectric constant perturbation is traveling

$$\Delta\epsilon = \delta\epsilon(x, y)cos(\Omega t - qz), \tag{2.21}$$

or when the dielectric constant perturbation is harmonic ($q = 0$)

$$\Delta\epsilon = \delta\epsilon(x, y)cos(\Omega t + \varphi). \tag{2.22}$$

If we replace t with $-t$ in Eq. (2.21), we find that the cosine term becomes $cos(-\Omega t - qz)$. Therefore, all the Ω term change signs in Eq. (2.8). Therefore,

the phase will not cancel inside all the exponentials, which means that when light travels in the backward direction, photonic transitions are prohibited. This result is relatively easy to understand, since the perturbation adds an unidirectional momentum kick (similar to the Doppler's effect). For the case of harmonic modulation, if I replace t with $-t$ in Eq. (2.22) and recall that $\varphi = \Omega \times t_{origin}$, and t_{origin} is the *time origin* of the RF perturbation (with frequency Ω), then φ also flips sign. Therefore, the cosine term remains the same: $cos(-\Omega t - \varphi) = cos(+\Omega t + \varphi)$. This result means that the photonic transition will also happen when light is traveling backward, which makes sense because the energy is also matched in the backward direction. Nevertheless, this result does not mean that harmonic modulation does not break time-reversal symmetry. In fact, if we only look at Eq. (2.19), the imparted φ phase is of opposite signs when photons are coupled either from mode 1 to mode 2 or from mode 2 to mode 1. This indicates that a non-reciprocal phase can be induced using harmonic modulation as I will discuss this more in detail in Chapter 5.

2.2 Photonic transition implemented with silicon photonics

Photonic transitions can be generated on the silicon photonics platform. As I mentioned in the previous Section, the photonic transition occurs fundamentally by perturbing the refractive index. This does not impose any restrictions on the choice of the optical material. The refractive index perturbation can then be translated to refractive index *modulation* in silicon, and high speed silicon modulators are readily available as discussed in Chapter 1 (Section 4).

Aside from all the interesting applications that I will discuss in the next Sec-

tion, the main advantage of using silicon over other material platform is that the mode coupling coefficient (transition rate, see Eqs. (2.10) and (2.14)) can be optimized by locally adjusting the doping profile. This is extremely powerful because now we can design more complicated waveguide structures to support the ideal photonic two-level system without too many constraints. In addition, the coupling can be significant since the optical confinement in silicon waveguides is large. Moreover, the photonic two-level systems fabricated in silicon can be directly integrated with electronic circuits and components such that the device complexity can be scalable. However, the drawback of using silicon is again, as mentioned in Chapter 1, the associated optical absorption from the same free carriers that are used to generate the modulation.

2.3 Photonic transition applications in silicon photonics

The obvious application for photonic transitions is to convert light from one frequency to another, which is is potentially useful in future telecommunications to provide efficient wavelength channel routing. In silicon, this is usually done using optical non-linear processes such as four-wave-mixing [37,87–91], but the problem with non-linear processes is that it require rather long waveguides and high input power. Nevertheless, frequency conversion using silicon photonics is still quite unexplored because it is not a necessary function in current digital optical communication systems (it is uncommon to convert information between different wavelength channels). However, photonic transitions can be very well-suited for analog applications to generate or modulate RF signals at very high carrier frequencies. The reason is that although optical links provide almost infinite bandwidth, but typically, the optical bandwidth of silicon pho-

tonics is limited because of the EO conversions. For example, to overcome the weak effect of the carrier dispersion (See Chapter 1 Section 4) effect in silicon, one often have to use resonators (see Chapter 3), which is bandwidth limited by its resonance linewidth. By using photonic transitions, one can bypass this limitation and convert information from one optical frequency to another (see Chapter 4 for more detailed information).

The photonic transitions break time-reversal symmetry. This means that the design of non-reciprocal devices such as isolators and circulators are possible using this phenomenon. To minimize the amount of inputs and outputs on a silicon photonics chip to reduce packaging cost, on-chip laser is desirable. Therefore, on-chip isolators become inevitable to eliminate the detrimental back reflected light to protect the laser. Isolators and circulators are typically made by using magneto-optical (MO) materials [92–98]. These materials (e.g. Ce:YIG or bismuth-lutetium-neodymium substituted iron garnet (BiLuNd-IG)) are not standard CMOS materials, and they are both expensive and difficult to integrate on silicon. One example for using MO materials to make an isolator, is by directly depositing MO materials on top of a microcavity [97]. It induces a non-reciprocal phase to the light that is traveling inside the microcavity, and the forward and backward resonances become spectrally separated. Nevertheless, the MO effect becomes much weaker because the quality of the deposited film is not on par with single crystalline MO materials. In addition, the MO effect in the optical domain is still much weaker compared to RF frequencies, hence an MZI [92] or a resonator [97] (as mentioned in the example above) has to be used to enhance the effect of the non-reciprocal phase. Another way to break reciprocity is to based upon the optical $\chi^{(2)}$ and $\chi^{(3)}$ nonlinear effect [99–103]. However, now the degree of non-reciprocity is dependent on the light intensity,

which is not practical because the reflected light can be of any light intensity. Based on the above discussion, the method of using time-dependent refractive index to make non-reciprocal devices is still a very attractive option. Recent works have demonstrated isolation using silicon modulators without using MO materials but their designs remain rather complicated or lack of on-chip implementation [81, 104–108]. One work was done [81] by using a traveling wave RF refractive index modulation. This method is exactly what we discussed in Section 2.1 by inducing one-way photonic transitions with $q \neq 0$. The major drawback of this method is that one require matching the velocity of the RF wave (namely, the ratio between q and Ω) to the ratio between the energy ($\hbar\omega_2 - \hbar\omega_1$) and the momentum ($\hbar k_2 - \hbar k_1$) of the two photonic modes (levels). Unfortunately, usually these two ratios are drastically different and requires a very slow RF wave. A 3 dB isolation is achieved through careful design of segmented PN diodes and traveling-wave electrodes. However, the device has a huge optical loss > 30 dB. Another approach is to use cascaded phase modulators as demonstrated in [104, 106]. These cascaded phase modulators will cancel out all the optical sideband components in one direction but not the others. However, the device is very long, and more than two modulators is required to cancel out all the sideband components. There are other approaches proposed using MZI modulators [107, 108]. Unfortunately, there are no on-chip demonstrations for these schemes. Nevertheless, all the schemes I mentioned above do not induce a non-reciprocal phase shift that is directly coupled to light.

Since on-chip isolation is difficult to achieve without indirectly coupling photons to an effective magnetic field through MO materials, one natural question to ask is: *Can we generate an effective magnetic field that is directly coupled to photons without using MO materials?* In Chapter 5, I will demonstrate how to

use photonic transitions to induce an effective magnetic field directly coupled to light, and to use it to achieve isolation. Then, in Chapter 6, I will demonstrate how one can use this effect magnetic field to demonstrate a photonic topological insulator, and I will also show preliminary designs and results that can potentially realize this device.

2.4 Summary

In this chapter, I show the analogy between atomic transitions in a two-level system and photonic transitions in a photonic two-level system. The photonic transitions can be induced by modulating the refractive index in an optical structure that supports two distinct optical modes with different optical frequencies. The modulation has to provide both energy and momentum conservation for the photons in the two optical modes to couple. The advantage of using silicon photonics to induce such a transition is subsequently introduced. Then, the applications of silicon photonics enabled photonic transitions are discussed.

CHAPTER 3

MICRORING RESONATORS PERTURBED IN THE TIME DOMAIN

3.1 Introduction to microring resonators

Microring resonators are one of the fundamental building blocks in silicon photonics. They have relatively smaller size and stronger electro-optical interaction. The combination of small size and strong EO conversion means that, intrinsically, very low external modulation power is required.

A microring resonator is a circular waveguide that allows light to travel inside the ring for multiple round trips before it decays. As shown in Fig. 3.1(a), an additional waveguide (we call it the bus-waveguide) is evanescently coupled with the microring to allow external accessing. Like any other resonators (such as Fabry-Perot resonators), the resonance condition of the microring is satisfied if the round trip phase is multiple integers of 2π:

$$\frac{2\pi}{\lambda} n_{eff} L_{eff} = \beta L_{n_e ff} = 2\pi m, \tag{3.1}$$

where β is the effective wavevector of the optical mode, L_{eff} is the effective microring length (the length which the optical mode actually travels), m is a positive integer number, λ is the optical wavelength, and n_{eff} is the effective refractive index of the waveguide. Here we say the m_{th} order mode indicating how many 2π phases light gathers per round trip inside the resonator. The resonance frequency for adjacent ($\Delta m = \pm 1$) resonance modes is defined as the free-spectral-range (FSR), which is also equivalent to the frequency of light roundtrips. To show this, we can first write $\Delta\beta L_{eff} = 2\pi\Delta m$, then

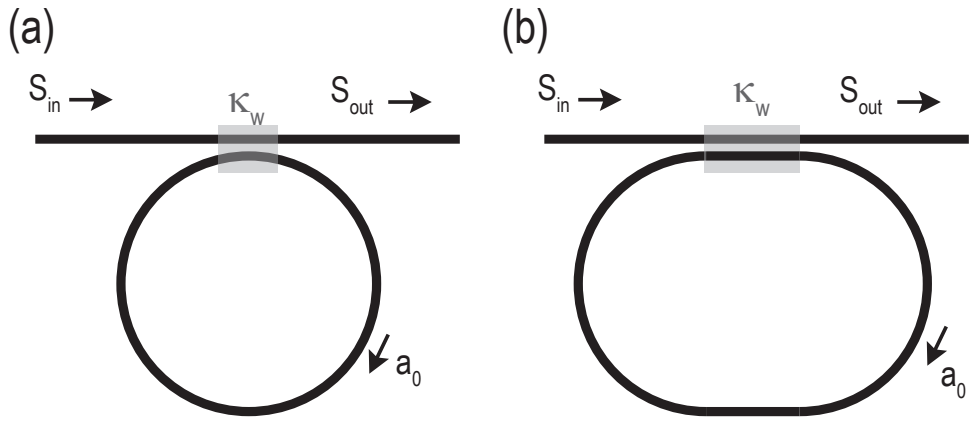

Figure 3.1: Illustration of the top view of two different types of microring resonators: (a) a ring resonator, and (b) a racetrack resonator.

$\Delta\beta/\Delta_f = 2\pi 1/\Delta f$, since we know that $2\pi/v_g = \Delta f/\Delta\beta$, we get $\Delta f = FSR = v_g/L_{eff}$. This indicates that the FSR can also be defined as the roundtrip frequency.

Note that the term *microring* does not impose any restrictions on the actual shape of the resonator as long as the waveguide forms a closed loop which Eq. (3.1) can be applied. Similar and common structures such as a racetrack (as shown in Fig. 3.1(b)) can also be treated as a variation of a microring resonator. A racetrack microresonator can provide a much larger coupling between the bus-waveguide and the resonator without overly reducing the coupling gap, which at times can be difficult to fabricate. If we define a_0 is the amplitude circulating inside the microring, τ_0 is the optical lifetime before light decays in the waveguide, and τ_c is the lifetime before light is coupled out to the bus-waveguide, one can write the following dynamical equation [109]:

$$\frac{da_0}{dt} = (j\omega_0 - \frac{1}{\tau_0} - \frac{1}{\tau_c})a_0 + \kappa_w S_{in}, \tag{3.2}$$

where $\omega_0 = 2\pi c/\lambda$, S_{in} is the input light amplitude from the bus-waveguide, and

κ_w is the coupling from the bus-waveguide into the microring. Note that τ_c and κ_w has to be related because the coupling is reciprocal:

$$|\kappa| = \sqrt{\frac{2}{\tau_c}}, \tag{3.3}$$

and the relation between S_{out} and S_{in} (transmission) can be written as:

$$S_{out} = S_{in} - \kappa_w^* a_0 \tag{3.4}$$

To get the transmission spectrum, we can Fourier transform both sides of Eq. (3.2) to obtain:

$$a_0(\omega) = \frac{\kappa_w}{j(\omega - \omega_0) + 1/\tau_0 + 1/\tau_c} S_{in}(\omega) \tag{3.5}$$

In Eq. (3.5), we have assumed that κ_w is independent of wavelength. Now by plugging Eqs (3.3) and (3.4) into Eq. (3.5), we obtain the transmission (T):

$$T = \frac{S_{out}(\omega)}{S_{in}(\omega)} = \frac{j(\omega - \omega_0) + 1/\tau_0 - 1/\tau_c}{j(\omega - \omega_0) + 1/\tau_0 + 1/\tau_c} \tag{3.6}$$

Eq. (3.6) is a Lorentzian function with the peak center at $\omega = \omega_0$, and its FWHM (full width at half maximum) is $2(1/\tau_0 + 1/\tau_c)$. If we further define the loaded time-constant $1/\tau_L = 1/\tau_0 + 1/\tau_c$, then the loaded quality factor (Q_L) of this resonator is defined as:

$$Q_L = \omega_0 \frac{Resonator\ Energy}{Power\ dissipated\ from\ the\ resonator} = \frac{\omega_0 \tau_L}{2} \tag{3.7}$$

The τ_c and τ_0 terms play a significant role to the extinction ratio (ER = T_{max}/T_{min}). The Lorentzian resonance with different τ_c and τ_0 based on Eq. (3.6) are plotted in Fig. 3.2. In Fig. 3.2(a), we see that when $\tau_c < \tau_0$ (over-coupled), which physically means that the loss of the microcavity due to coupling (to the bus-waveguide) is larger than the loss due to waveguide loss, both the ER becomes

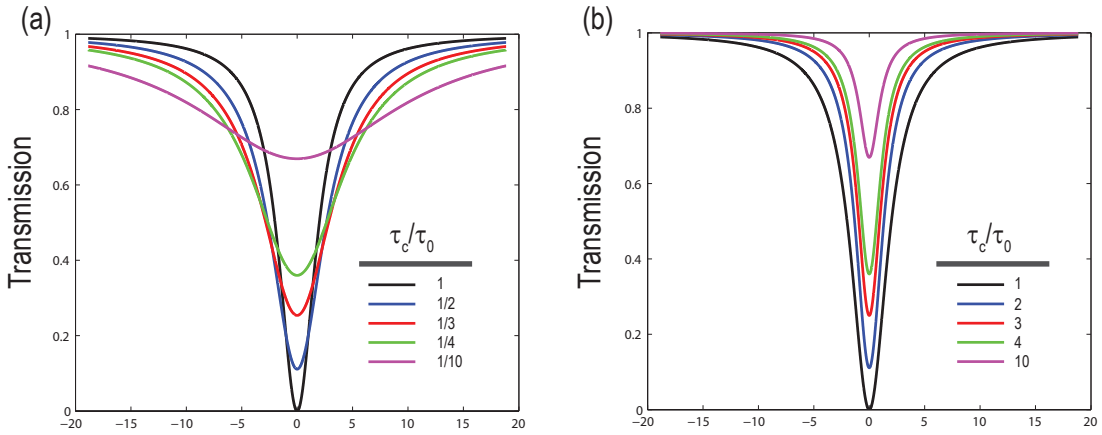

Figure 3.2: Normalized transmission for the (a) over-coupled, and (b) undercoupled microring resonators.

smaller and the FWHM of the resonance is broadened as τ_c becomes smaller. For the other case shown in Fig. 3.2(b), as $\tau_c > \tau_0$ (under-coupled), where the loss of the microcavity due to coupling is smaller than the loss due to waveguide loss, both the ER becomes smaller and the FWHM is narrower as τ_c becomes larger. In between of the two cases is $\tau_0 = \tau_c$, which is a conditon referred to as the *critical coupling*. Critical coupling is much desired in a number of scenarios mainly because of its large extinction ratio and maximum power enhancement.

The fact that light travels in the microring for multiple roundtrips before it decays implies that the power circulating inside the microring should be higher than the power from the bus-waveguide input. The power circulating inside the microring (P_{cir}) can be generally expressed as (note that a_0 is normalized to energy instead of power, meaning: $|a_0|^2$ = *total energy inside the resonator*):

$$|a_0|^2 = P_{cir} \times \frac{L_{eff}}{v_g} \tag{3.8}$$

where v_g is the group velocity, and the L_{eff}/v_g term simply means how much time light spent in the resonator per roundtrip. By combining Eq. (3.5) into Eq.

(3.8), we obtain:

$$\frac{P_{cir}}{P_{in}} = \frac{v_g}{L_{eff}} \frac{2/\tau_c}{(\omega - \omega_0)^2 + (1/\tau_L)^2} \tag{3.9}$$

where $P_{in} = |S_{in}|^2$, and as expected, the power enhancement is maximized when the input light is on resonance ($\omega = \omega_0$):

$$\left.\frac{P_{cir}}{P_{in}}\right|_{\omega=\omega_0} = \frac{v_g}{L_{eff}} \frac{2\tau_c}{(1 + \tau_c/\tau_0)^2} \tag{3.10}$$

Equation (3.10) indicates that the maximum power enhancement is achieved at the critical coupling condition with:

$$\left.\frac{P_{cir}}{P_{in}}\right|_{\omega=\omega_0,\tau_c=\tau_0} = \frac{v_g\tau_c}{2L_{eff}} = \frac{\tau_c}{2} FSR = \frac{1}{\pi} \frac{FSR}{\Delta f|_{FWHM}} = \frac{1}{\pi} Finesse \tag{3.11}$$

To get Eq. (3.11), we have to recall that the free-spectral-range (FSR) is the frequency of light roundtrips inside the microring. Here a new term is defined: Finesse, in Eq. (3.11), which describes the ratio between the FSR and the linewidth of the resonances. The final conclusion is that the higher the Finesse, more power is built-up in the resonator.

3.2 Time-dependent perturbation of a microring resonator

A resonance frequency shift ($\Delta\omega(t)$) is expexcted when the dielectric constant is changing inside a microring resonator based on Eq. (3.1). If we define the electric field inside the resonator as:

$$E = a_0(t) e^{(j\omega_0 - 1/\tau_0 - 1/\tau_c)t} E_0(x, y), \tag{3.12}$$

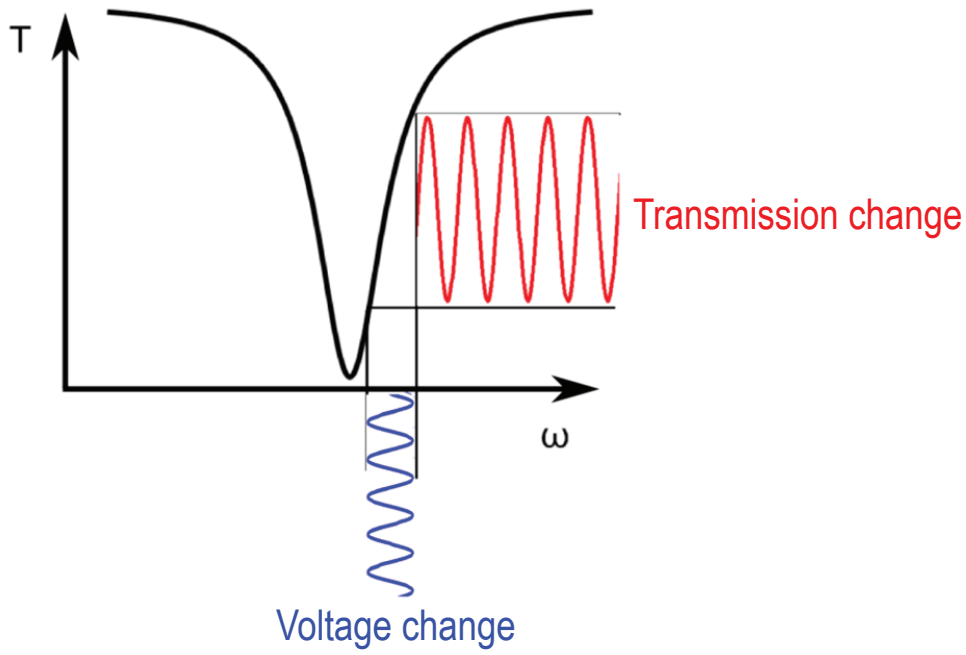

Figure 3.3: Illustration of the operation of a microring modulator in the frequency domain.

By plugging Eq. (3.12) into the Maxwell's equations (Eqs. (2.2) and (2.3)), eliminating the unperturbed terms and the higher order terms, eventually we get:

$$\frac{d\bar{a}_0}{dt} = (j(\omega_0 + \Delta\omega_0(t) - \omega_L) - \frac{1}{\tau_0} - \frac{1}{\tau_c})\bar{a}_0 + \kappa_w S_{in}, \tag{3.13}$$

where $\bar{a}_0(t)$ is the slowly varying amplitude change of $a_0(t)$ (the fast oscillating nature of light is omitted in this equation), and ω_L is the laser frequency. Eq. (3.13) shows that a dielectric constant perturbation will detune the resonance frequency (relative to the laser frequency).

3.3 Microring resonator based modulator

A microring modulator is a device that when electrical signal is applied, it will shift its resonance position while light is traveling in it. The net effect is that the transmission of the ouput light at the laser wavelength changes according to the amount of resonance shift applied and controlled by the electrical signal, and the output light is modulated with the exact same intensity profile as the applied electrical signal voltage [59]. An example of such a device made with silicon is shown in Fig. 1.5(b). To futher show the effect, as depicted in Fig. 3.3, when a sinusoid voltage is applied to the micoring modulator (blue), the resonance is also subjected to a sinusoid shift accordingly, which results in an optical transmission change at the output (red). This input electrical signal does not need to be a sinusoid. For digital communications, a series of square pulses indicating '1's and '0's are generally used. The benefits of using microring resonators are its highly efficient modulation, thanks to its sharp spectral resonance profile, and its extremely compact size. The size of the micro-resonator is limited by its minimum bending radius (without sacrificing too much radiation loss), which can be as small as around 2 μm [74] for silicon microdisks.

The integrity of the reproduced signal from the electrical to the optical domain is limited by the resonance linewidth of the microring, the RC constant of the electrical components that induce the refractive index change, and the non-linearity of the modulation. It is intuitive to say that the speed of the microring modulator is limited by the photon lifetime inside the resonator (which is τ_L). This is in fact true for any resonator systems, and the reason is that one cannot modulate light more than once while it is still traveling in the resonator [110, 111]. Therefore, we can only expect good signal integrity for the

cases when $f_M < 1/\tau_L = \Delta f_{FWHM}$, and f_M is the modulation frequency [112]. In Chapter 4, I will demonstrate how this condition can be relaxed in a microring modulator. The other bandwidth limitation is the RC bandwidth of the device, which can be calculated by using the following expression: $f_M < 1/(2\pi RC)$. The third limitation is the non-linearity of the modulator. The non-linearity is a measure of the extent on how the change of optical transmission does not linearly follow the change of the voltage shift. This metric is more important for analog signals, where a non-linear response of a modulator will give rise to spurious frequency components that lies inside the signal bandwidth and distorts the transmitted signal. There are on-going efforts on minimizing the nonlinear signal distortions in silicon modulators [26–28]. For digital signals, only on and off states are detected; Therefore, device non-linearity is much less relevant.

3.4 Modelling silicon microring modulators using numerical methods

Based on all the previous discussions, a dynamical model can be created, which can be solved numerically, for the depletion mode microring modulator (again, we are interested in the depletion mode mainly because it can be modulated at higher RF frequencies).

The first step is to characterize the static (DC) response of a silicon microring modulator with a cross-sectional waveguide dimension and doping profile illustrated in Fig. 1.4. The width of the waveguide is 450 nm, the height of the waveguide is 250 nm, and the silicon slab thickness is 50 nm. The slab waveguide is embeded in SiO_2, and it allows only one TE-polarized mode. The center

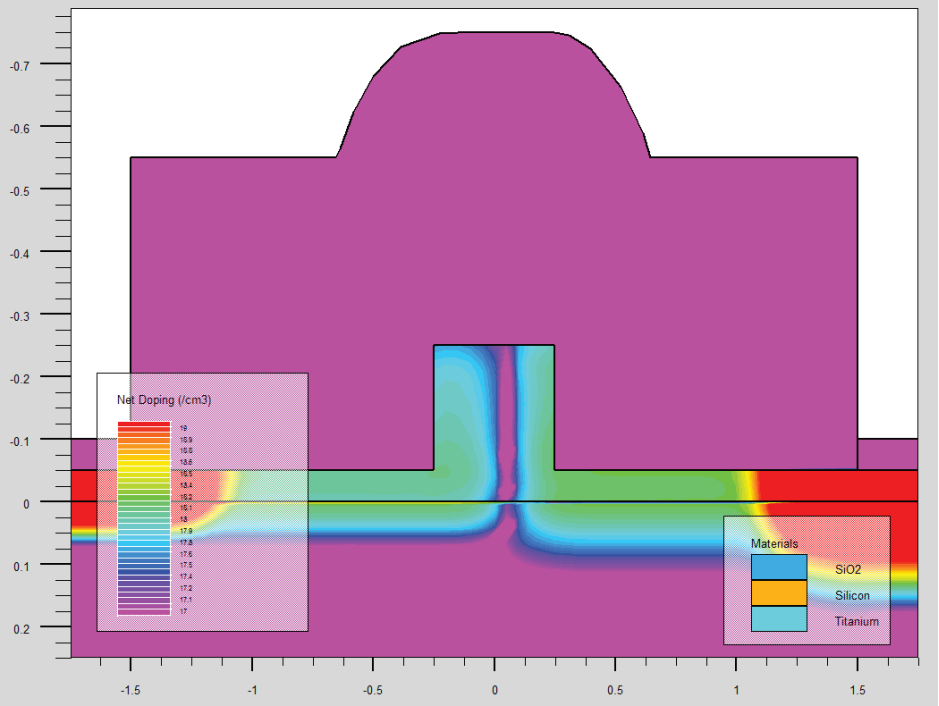

Figure 3.4: Simulated cross-sectional doping profile of a silicon microring modulator from SILVACO. The concentration for both the p- and the n-doping are aimed at $1 \times 10^{18}\ 1/cm^3$. The outer P+ and N+ doping are aimed at $1 \times 10^{20}\ 1/cm^3$

of the PN junction is set 100 nm away from the center and toward the N region to increase the modulation efficiency [67]. Both the P and the N concentration are set to $1 \times 10^{18}\ 1/cm^3$, which is a pretty good balance between optical loss and refractive index change (see Eq. (1.1) and (1.2)). The simulated doping profile can be obtained from a commercially availabe software: SILVACO, and the result is shown in Fig. 3.4. The doping profiles for different reversed-bais voltages are also obtained. Based on these simulated carrier profiles, both the distributions of the refractive index and the induced optical loss are subsequently calculated using another commercial software: COMSOL. Now by solving the mode profiles using these distributions, we can simultaneously get the n_{eff} and

the modal loss (imaginary part of the n_{eff}). Getting the modal loss is important because that will define the lineshape of the resonance and influence the modulation efficiency. The resonance profiles for each of the bias-voltages can then be calculated by plugging in both the $\Delta\omega_0$ based on the Δn_{eff} referenced to n_{eff} at zero volts (now static) and the τ_0 contributed from both the modal loss and the fabrication loss (α_{fab} = 4 dB/cm) into the steady-state solution of Eq. (3.13). The simulated DC response of a silicon microring modulator is shown in Fig. 3.5. From Fig. 3.5(a), we see that the results are exactly as predicted: the resonance frequency red-shifts and the laser (vertical red line) is biased on different places on the Lorentzian resonance profile as different negative voltages are applied. The bias voltage leads to a change in the output transmission as shown in Fig. 3.5(b). One can see that the transmission quickly rises from 0.1 to 0.8 within a change of 2 volts. Note that in this case, the loaded Q_L is 28,900, the resonance linewidth is about 7 GHz, and we have assumed that the resonator is critically coupled at zero volts.

To analyze how the photon lifetime affects the digital signal integrity, we can numerically solve Eq. (3.13) by using Euler's method. By defining a very small time-step ($\Delta t << \tau_L$, otherwise the solution will not converge), we can modify Eq. (3.13) (I removed the bar on a_0 just to simplify):

$$a_{0,i} = a_{0,i-1} + (j(\omega_0 + \Delta\omega_0(t) - \omega_L) - \frac{1}{\tau_0} - \frac{1}{\tau_c})a_{0,i-1}\Delta t + \kappa_w S_{in}\Delta t, \tag{3.14}$$

where $t = i \times \Delta t$. From Eq. (3.14), by giving an initial value for S_{in}, $a_{0,i}$ can be solved in i steps. In each of the i steps, the new $a_{0,i}$ is calculated based on the value obtained in the previous step ($a_{0,i-1}$). Then, the optical transmission (T) of the microring modulator can be directly obtained from Eq. (3.4). By using the same parameters for the DC response simulations (see Fig. 3.5), we should

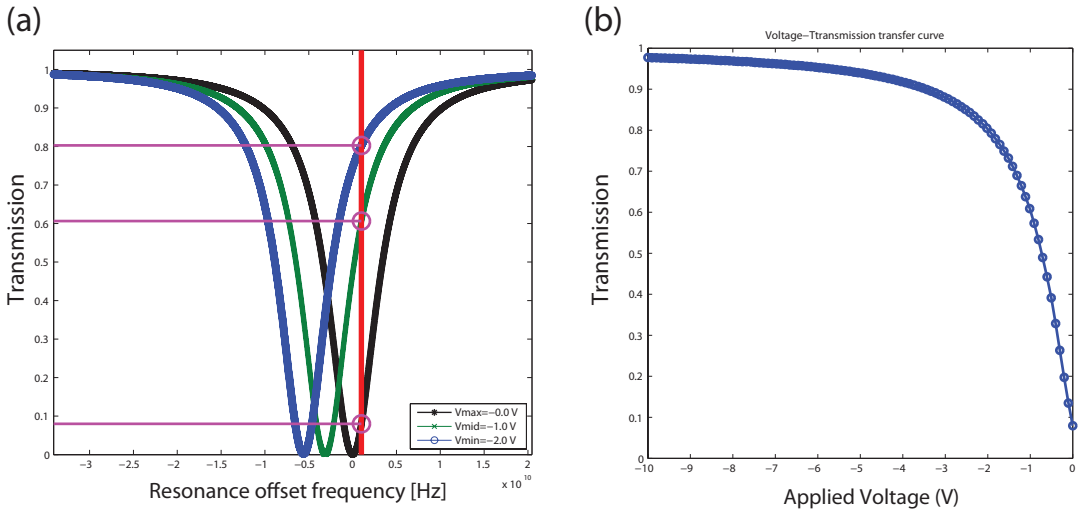

Figure 3.5: Simulated cross-sectional doping profile of a silicon microring modulator from SILVACO. The concentration for both the p- and the n-doping are aimed at 1×10^{18} $1/cm^3$. The outer P+ and N+ doping are aimed at 1×10^{20} $1/cm^3$

expect strong signal degredation when the modulation frequency is beyond the resonance linewidth (7 GHz). In fact, in Fig. 3.6, we show that the square pulses that represent the digital 1's are indeed significantly distorted as the modulation speed is much larger than the 7 GHz linewidth. Note that the input signals are also slightly distorted at frequencies larger than 20 Gbps because the electrical time constant (RC) of the device have been taken into account. To really show the 3 dB bandwidth of the device EO response, again, we can use equations (3.14) and (3.4) to calculate T with pure sinusoid input voltages at multiple RF frequencies. In this calculation, we assume that the laser frequency is detuned from the resonance frequency by half the resonance linewidth, which gives the maximum modulation efficiency (steepest part of the Lorentzian profile). In addition, we assume a small signal modulation that results in a resonance frequency change of about 0.5 % of the resonance linewidth. The transmission for each individual frequencies (f_M) is a similar plot to Fig. 3.6, but a sinusoid

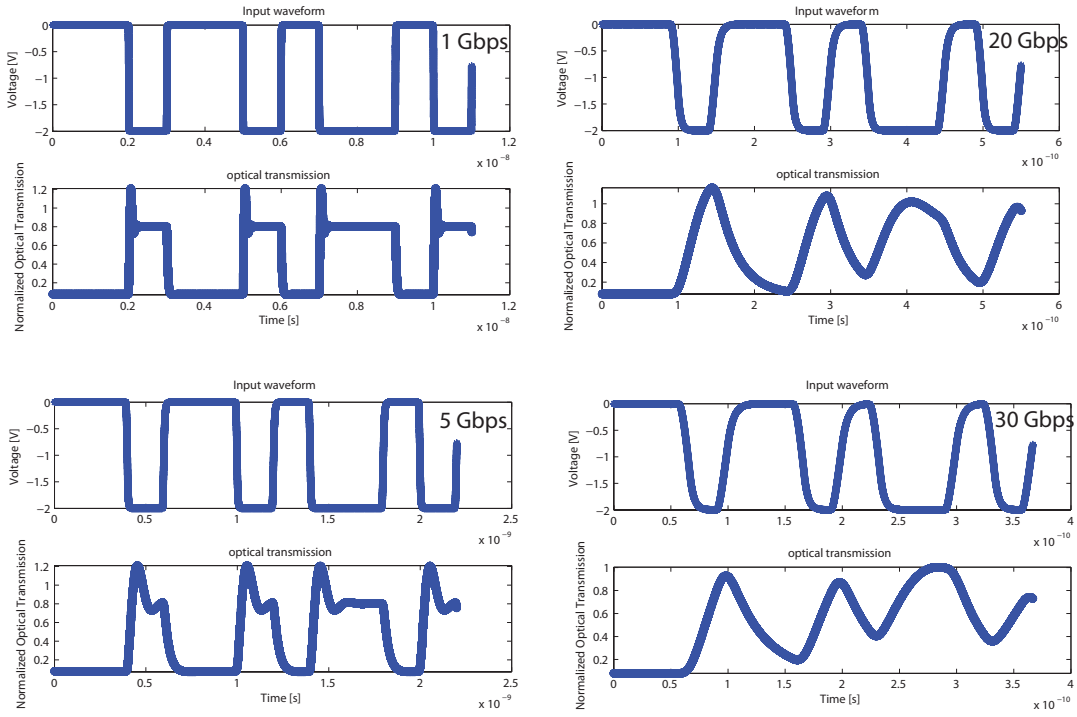

Figure 3.6: Simulated output transmission of a silicon microring modulator modulated with 1, 5, 20, and 30 Gbps electrical signal. The modulator used in the simulation has a Q_L of 28,900, and it is operating near the critical coupling regime

fluctuation as shown in Fig. 3.7(a). One can immediately see that as predicted, the amplitude of the fluctuation decreases with increasing frequency. From this figure, we can define the modulation depth as:

$$\Delta_M = \frac{T_{max} - T_{min}}{T_{max} + T_{min}}, \tag{3.15}$$

where $T_{max(min)}$ is the maximum (minimum) transmission. The modulation depth verses the modulation frequency is plotted in 3.8(b). From this figure, the 3 dB bandwidth is about 11 GHz. This number is much higher than the predicted 7 GHz, based on the resonance linewidth measured in Fig. 3.5(a), because the laser is biased on the slope of the resonance. However, the trend should be the same: the higher the Q_L, the smaller the 3 dB bandwidth. Therefore, there is

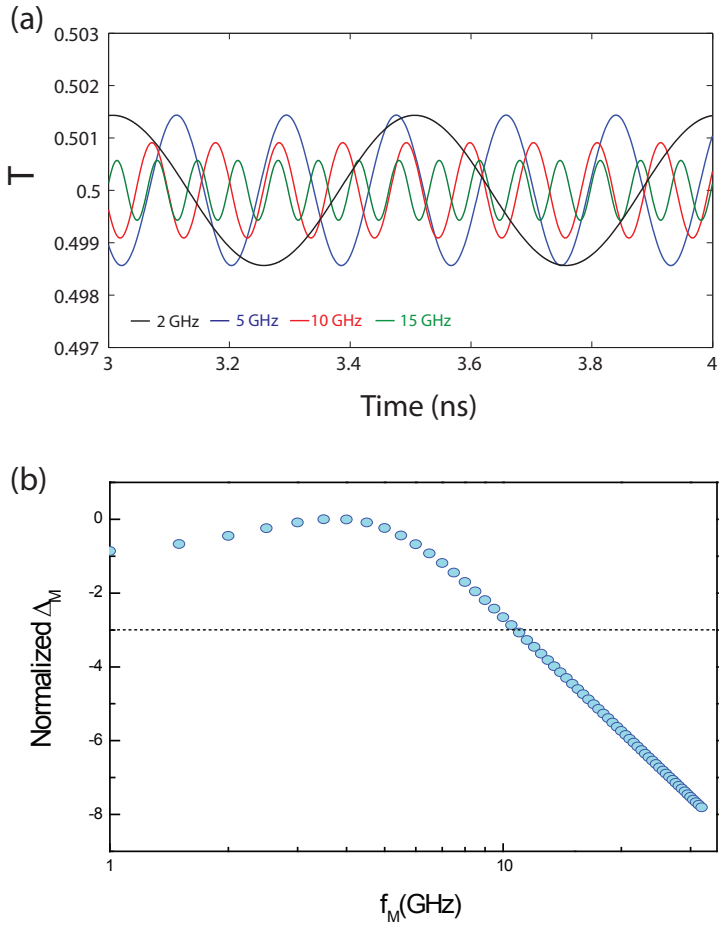

Figure 3.7: (a) Simulated time evolution of the output transmission of a silicon microring modulator modulated with 2, 5, 10, and 15 GHz pure sinusoid signal. (b) The modulation depth versus different pure sinusoid modulation frequencies. The modulator used in the simulation has a Q_L of 28,900, and it is operating near the critical coupling regime

always a fundamental tradeoff between modulation RF power and frequency. The higher the Q_L, the narrower the Lorentzian, which leads to smaller bandwidth; Therefore, the modulation is more efficient that leads to lower RF power. On the other hand, for a smaller Q_L, the broader the Lorentzian, which means a larger bandwidth, but it leads to higher RF power.

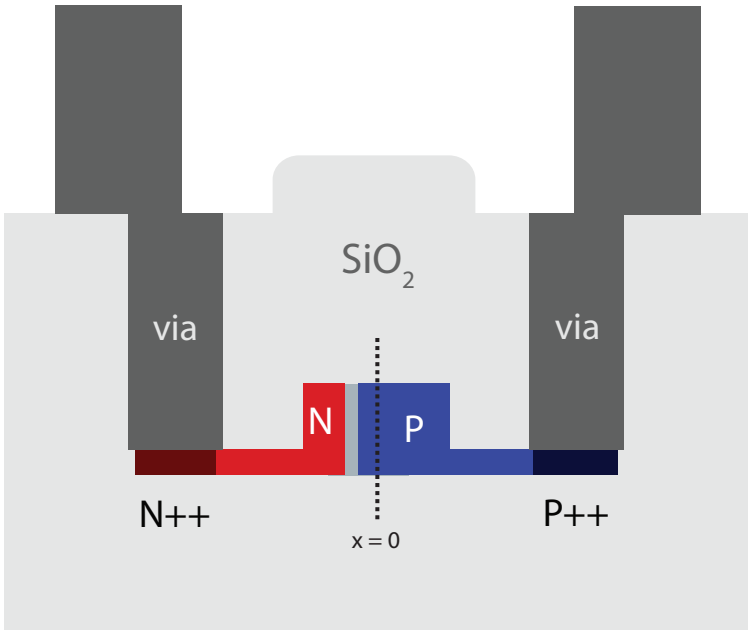

Figure 3.8: Illustration of the cross-section of a typical depletion mode silicon modulator.

3.5 Design and fabrication of a silicon modulator

The general goals of designing a silicon modulator is to maximize both the modulation efficiency and the modulation frequency, and to minimize the waveguide loss. Fig. 3.8 illustrates an example cross-sectional profile including the metal vias. The waveguide dimensions can be anything in general, but with some constraints further discussed in thie section. This cross-sectional profile can be implemented in either microring modulators or to induce photonic transitions in straight silicon waveguides. Here we still focus on the depletion mode modulator for the reasons discussed in the previous Sections. The vias are metals that connect the silicon slab to the metal wires and pads on top of the SiO_2 cladding. To increase the modulation efficiency, the center of the PN juction has an offset of about 100 nm into the N-doping. From Eq. (2.1), wee see that the

hole-density change ΔN_h has a much larger influence to Δ_n versus the electron-density change ΔN_e. Therefore, as the depletion width (grey) grows, the optical mode in the waveguide sees more change in the P-doping than the N-doping. To increase the modulation frequency, we need to lower the overall device series resistance (R_s). This can be done by 1) improving the quality of the ohmic contact between the vias and the silicon slab, and 2) shortening the distance between the via and the waveguide edge. For 1), the ohmic contact is achieved through introducing a silicide layer between the metal and the via, this will be further discussed later in this section. For 2), the side effect of shortening the distance between the via and the waveguide edge is that it would introduce extra loss from the interaction between light and the vias. Therefore, there is an optimum distance between the via and the waveguide edge. For a waveguide width of 450 nm, height of 250 nm, and slab thickness of 50 nm, that distance is typically around 800 nm to 1 μm. Thicker slabs could also improve R_s, but at the cost of more light leakage into the slab that overlaps with the vias and the high doping regions (N++ and P++), which means that the vias have to be pushed further away from the waveguide and the radiation loss is higher when bending the waveguide to form a ring.

The depletion mode silicon modulator is fabricated with general CMOS compatible processes on an SOI (silicon-on-insulator) wafer. The fabrication steps are depicted in Fig. 3.9, and are explained in the following: First we pattern the e-beam resist to on top of an SOI wafer (Fig. 3.9(a)); Subsequently, the silicon layer is etched down (reactive ion etch (RIE)) and leaving a thin silicon slab. After the waveguide is formed, a photoresist layer is patterned on top, and the silicon slab is etched away (RIE etch) in specific places (Fig. 3.9(b)). This step is mainly to remove the slab to avoid both the electrical cross-talk

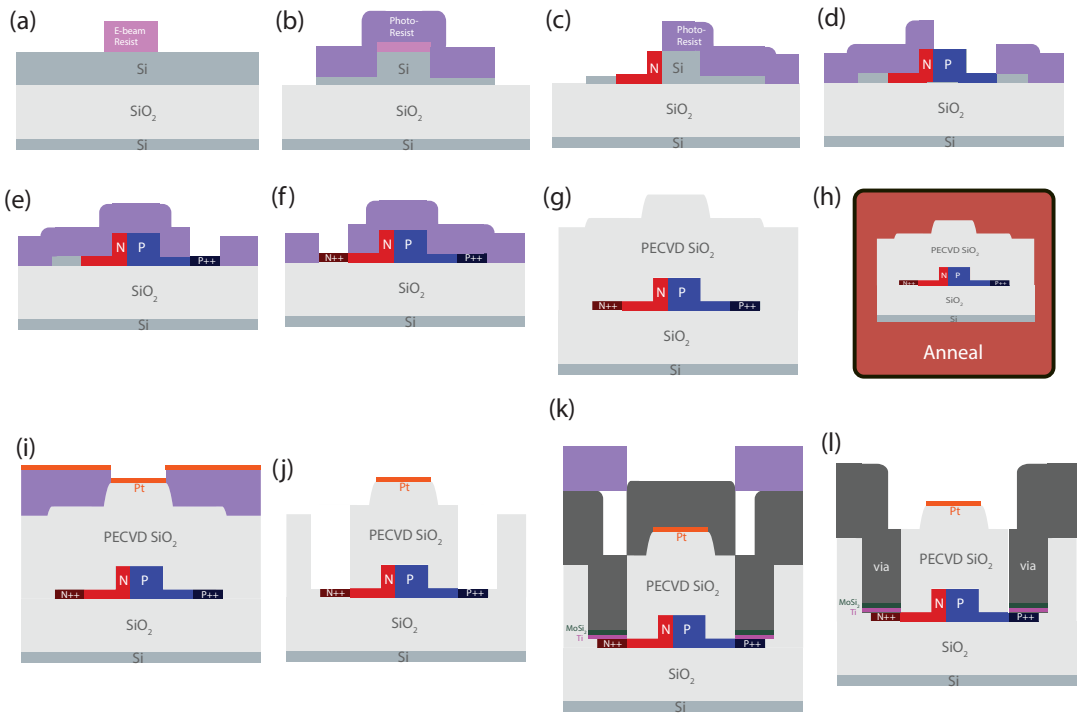

Figure 3.9: Illustrations of all the critical steps to fabricate a depletion mode silicon modulator (cross-section).

and parasitic capacitances, and to ensure good coupling from the chip facet to the tapered waveguide [113]. Next, in four separate photolithography steps, we define the patterns for the four dopings (N, P, P++, and N++ in Fig. 3.9(c), (d), (e), and (f), respectively). Here, phosphorous is used for the N-doping and boron is used for the P-doping. After the four doping steps, the wafer is cladded with PECVD (plasma enhanced chemical vapor deposition) SiO_2 (Fig. 3.9(g)). Then, the wafer is placed inside a furnace, then an RTA (rapid thermal anneal), for recrystallization and dopant activation, respectively (Fig. 3.9(h)). After the dopants are activated, a thin layer of platinum is sputtered and lift-offed to form the heaters (Fig. 3.9(i)). The heaters are optional, and they are used to induce a thermo-optic static phase shift in silicon. After the heater is formed, the SiO_2 cladding is etched (RIE) to reveal the silicon slab and form the trenches for the

vias. This step is critical because if the cladded SiO_2 is not completely removed, the metal-silicon interface will have a dielectric barrier that prevents good electrical contact. Therefore, a subsequent BOE (buffered oxide etch) dip is necessary to remove all the remaining SiO_2. After the BOE dip, in three consecutive steps, $MoSi_2$, titanium, and aluminum are sputtered everywhere on top of the wafer as well as inside the SiO_2 trenches. The $MoSi_2$ is a silicide layer (about 40 nm) to form good ohmic contact between the silicon and the metal, and the titanium layer (about a few nanometers) is to provide good adhesion between the aluminum and the SiO_2. The sputtered aluminum is about 1.6 μm thick for a SiO_2 claddint thickness of 1 μm. Then, another photoresist layer is patterned on top of the aluminum, and the aluminum is subsequently etched to form all the electrical connects and test pads.

3.6 Summary

In this chapter, I discussed the physics of a microring resonator, and how a silicon microring resonator can be used as a modulator. A theoretical model is also provided to show the dynamics of a silicon microring modulator. Last, I show how to design and fabricate a silicon modulator that can be implemented not only in a silicon microring modulator, but also in other silicon devices that require a time-dependent refractive index perturbation (such as devices to induce photonic transitions as discussed in Chapter 2).

CHAPTER 4

MICRORING MODULATORS OPERATING BEYOND THE LINEWIDTH LIMIT

4.1 The linewidth limit and the power-frequency tradeoff

Achieving simultaneous low power and high frequency operation of silicon microring modulators is challenging because the modulation frqequency is fundmentally limited by the resonance linewidth [110–112]. The reason for this linewidth limitation is discussed quite extensively in Chapter 3. The net result is that in order to increase the modulation frequency f_M, one needs to increase the resonance linewidth (by introducing extra loss inside the resonator). However, this linewidth broadening also means that the modulation efficiency is compromised because the slope of the Lorentzian profile is more gradual, and more power is required to drive the modulator. Therefore, the design of a microring modulator is always restricted to this power-frequency tradeoff. While microring modulators demonstrated so far [46,54,55,59,76] have attractive features such as compactness, low drive voltage, low power consumption, but this tradeoff hinders their utilization in extremely high frequency (30-300 GHz) microwave photonic applications. These applications include high speed analog communication and signal processing [16,17,20], which are also introduced in Chapter 1.

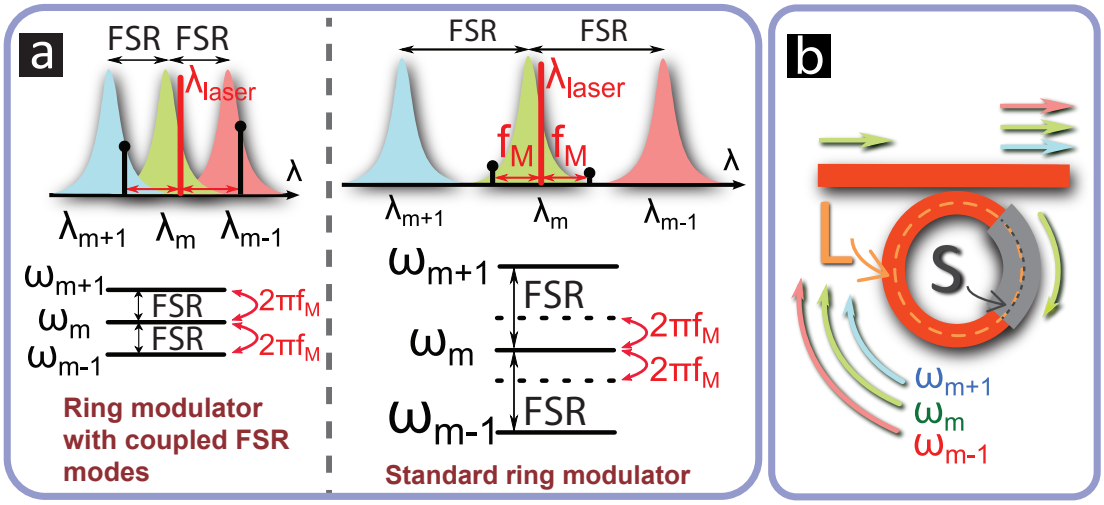

Figure 4.1: (a) Depiction of the optical spectra of the FSRC approach (left) and the standard ring modulator (right) under a sinusoidal modulation with frequency f_M. In our FSRC approach, the FSR matches f_M, while in the standard ring modulator, FSR >> f_M. The energy diagram is also depicted in the bottom to show the photonic transitions between the adjacent FSR mdoes. (b) Illustration of the FSRC scheme. The ring has a circumference L and a segment length S subjected to refractive index modulation.

4.2 Photonic transitions between adjacent FSR modes

In this section, I will show you that microring modulators can be operated at RF carrier frequencies much higher than the resonance linewidth by using electrically induced photonic transitions between adjacent FSR modes [114]. The photonic transitions between the adjacent FSR modes can also be intepreted as *coupling* between neighboring FSR modes (FSRC, as discussed in Chapter 2). Comparing to recent works that have shown broadband modulation of silicon resonators [111, 115–117], this approach is inherently more power-efficient but narrow-bandwidth, and it is therefore more capable of dealing with analog systems. Although the FSRC phenomenon has been observed and employed in various contexts and optical materials for modulation or frequency conversion

purposes [86, 118–125], demonstrating this effect using silicon photonics is critical to enable high frequency analog applications that can be readily integrated with CMOS electronics.

The coupling between the FSR modes will allow signals to be transmitted through the neighboring FSR modes. In other words, the FSRC approach [114] is to match the modulation sidebands with the adjacent FSR resonances. Before I explain the operation of the FSRC modulators, it is benificial to first explain the resonance linewidth limit in the frequency domain (as opposed to explaining it in the time domain in Chapter 3). In a standard microring modulator, such as the ones mentioned in Chapter 3 (right of Fig. 4.1(a)), the modulation sidebands are filtered by the resonance linewidth and therefore they are not transmitted through the ring. This leads to significant signal distortion. This linewidth limit description is basically the same as the time domain description: light cannont be modulated faster than the resonator decay rate. Now for the FSRC modulator (left of Fig. 4.1(a)), the FSR is matched to f_M. As a result, the modulation sidebands are transmitted through the ring thus signal is preserved. In order to transmit the sidebands through the neighboring FSR modes, one needs to excite the spatial modes of the microring resonaotor at these sideband frequencies. This is achieved by inducing coupling between the resonance mode ω_m at the laser frequency and the adjacent FSR modes ω_{m+1} and ω_{m-1} at the sidebands (m is the mode number explained in Chapter 3). As shown by the enegy levels in Fig. 4.1(a), this FSR coupling is exactly identical as inducing photonic transitions inside a microring. The only difference between this scheme and transitioning between two-photonic levels shown in Chapter 2 is that now the microring supports infinite number of modes, and we are particularly interested in the photonic transitions from the mode m to modes $m+1$ and

$m-1$.

In order to induce efficient coupling (transitions) between the FSR modes, we break the orthogonality between the adjacent FSR resonance modes by modulating only a portion of the ring as shown in Fig. 4.1(b). If we recall from Chapter 2, the coupling between two optical modes due to refractive index modulation is defined by the overlap integrals (Eq. (2.10) and (2.14)). Since all the FSR modes are all orthoganal with each other, this means that the refractive index modulation cannot be uniformly distributed throughout the entire mircoring. As shown in Fig. 4.1(b), the coupling will be non-zero when modulating a portion of the ring ($S < L$ where S is the modulation segment length, and L is the ring circumference). Since the derivation of Eq. (2.10) and (2.14) ignores the resonating nature of a microring, we can prove this by deriving the time-domain coupled mode equations. First we assume that the total electric field inside the microring contributed from all the FSR modes is:

$$E = \sum_n a_n(t) e^{(j\omega_n - 1/\tau_0 - 1/\tau_c)t} E_m(x,y,z), \tag{4.1}$$

where $\omega_n = \omega_0 + n \times FSR$, and $E_m(x,y,z) = E_m(x,y) \times exp(jk_m z)$ (z is the direction along the circumference of the microring). Here, we assume that both the waveguide loss (τ_0) and the coupling loss from the microring into the bus-waveguide (τ_c) are constants. Then, by plugging Eq. (4.1) into Maxwell's equations (Eq. (2,2) and (2.3)) with a small dielectric constant perturbation ($\delta\epsilon(x,y,z,t)$), eliminating the unperturbed terms and the higher order terms, we get:

$$\frac{d\bar{a_m}}{dt} = (j(\omega_m - \omega_L) - \frac{1}{\tau_0} - \frac{1}{\tau_c})\bar{a_m} + j\sum \mu_{mn}\bar{a_n} + \kappa_w S_{in}. \tag{4.2}$$

Note that this equation is very similar to the single FSR mode equation (Eq.

(3.13)), but now the couplings from all the FSR modes are considered in the μ_{mn} term:

$$\mu_{nm} = -\frac{\frac{\omega_n}{4}\iiint_{\infty}\delta\epsilon(x,y,z,t)E_nE_m^*\,dx\,dy\,dz}{\frac{1}{2}\epsilon_m\iiint_{\infty}E_mE_m^*\,dx\,dy\,dz}, \tag{4.3}$$

where $\delta(x,y,z,t)$ is the dielectric constant modulation. For the special case when n = m, Eq. (4.3) becomes:

$$\mu_{nm}\Big|_{m=n} = \frac{S}{L}\Delta\omega_m, \tag{4.4}$$

which is the self-coupling term that simply describes the resonance frequency shift for each individual FSR modes. Here, $\Delta\omega_m$ is defined as the maximum shift of the resonance frequency induced by the given $\delta\epsilon$. For example, the maximum shift happens when the whole microring is modulated, then $S = L$, and Eq. (4.4) becomes $\Delta\omega_m$. If we further assume that $E_n(x,y) \approx E_m(x,y)$, $\epsilon_m \approx \epsilon_n \approx \epsilon$, and $\omega_0 \approx \omega_m \approx \omega_n$ Eq. (4.3) can be written as:

$$\mu_{nm} = -\frac{\omega_0}{2\epsilon L}\int_0^L \delta\epsilon(z,t)e^{j(m-n)\frac{2\pi}{L}z}\,dz, \tag{4.5}$$

where $k_m = m\times 2\pi/L$. From Eq. (4.5), since m and n are integers, we can directly see that $\delta\epsilon$ cannot be a constant function of z. This means that the coupling between the FSR modes is non-zero only if there is a spatially non-uniform modulation. In the case when a portion of the ring is modulated, Eq. (4.5) becoms:

$$\mu_{nm} = -\frac{\omega_0\delta\epsilon(t)}{2\epsilon L}\int_0^S e^{j(m-n)\frac{2\pi}{L}z}\,dz = \frac{\Delta\omega_0(t)}{L}\int_0^S e^{j(m-n)\frac{2\pi}{L}z}\,dz. \tag{4.6}$$

For a sanity check, when m = n, Eq. (4.6) indeed degenerates to Eq. (4.4). Also from Eq. (4.6), we see that all the coupling coefficients are complex numbers and they all must satisfy:

$$\mu_{nm} = \mu_{mn}^*. \tag{4.7}$$

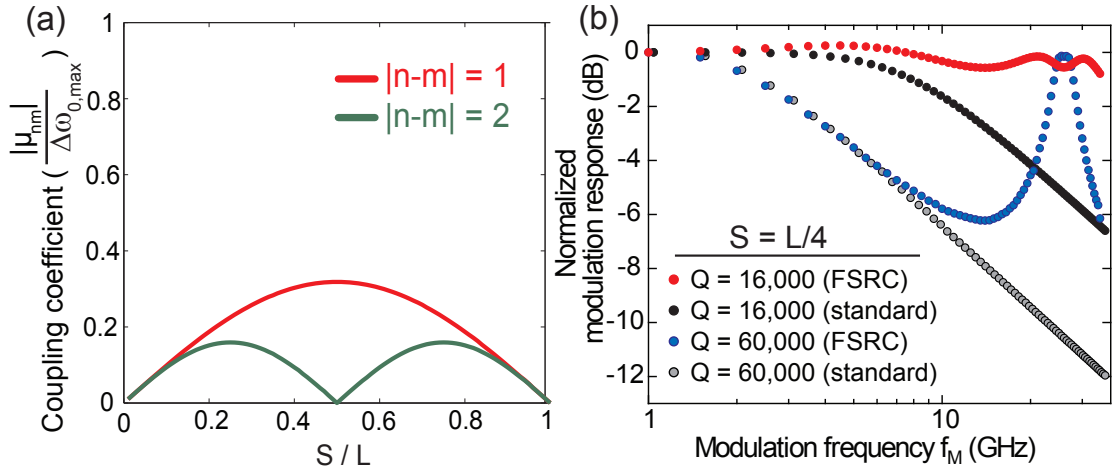

Figure 4.2: Calculation of (a) coupling coefficients between two FSR modes with indices m and n normalized to the maximum resonance frequency modulation $\Delta\omega_0$ when S = L) and (b) the modulation responses of the FSRC modulators (colored) and of the standard modulators (black and grey) with Q_L = 16,000 and Q_L = 60,000.

Fig. 4.2(a) shows the $|\mu_{nm}|$ calculated from Eq. (4.6) normalized to $\Delta\omega_0(t)$. From this figure, we see that the coupling coefficients (or the rate of the phtonic transitions) varies not only when S/L changes, but also for different set of FSR modes. For example, the largest coupling is obtained when $S = L/2$ for $|m-n| = 1$, and for $|m-n| = 2$, its largest coupling is slightly smaller, and it happens when $S = L/4$. This result indicates that the coupling is strongly dependent on the electrode *pattern* of the modulator.

The FSR coupling modulator is suitable for high RF carrier frequency and narrow-bandwidth modulation. In Fig. 4.2(b), the modulation responses (normalized to the response at 1 GHz) for both the FSRC modulator ($S = L/4$ and FSR = 26 GHz) and the standard modulator (FSR = 750 GHz) with different Q_L are numerically calculated. The calculation is achieved by solving Eq. (4.2) using Euler's method (see Eq. (3.14) and Chapter 3 for details). The transmis-

sion through the microring modulator has taken into account for 9 adjacent FSR modes (m, $m\pm1$, $m\pm2$, $m\pm3$, $m\pm4$), which corresponds to 9 linear differential equations (see Eq. (4.2)). Note that 9 modes are considered because the laser not only couples to the first nearest FSR modes ($m \pm 1$), but it also couples to the second (and higher) nearest FSR modes ($m\pm2, m\pm3, ...$) through either direct or cascaded coupling. The coupling coefficients between these 9 resonance modes are determined from Eq. (4.6). In Fig. 4.2(b), we see that for Q_L = 16,000, the response for the standard (black) modulator has a sharp roll-off beyond the resonance linewidth, and the response for the FSRC modulator (red) remain relatively flat up to the FSR frequency. In contrast, when the Q_L is high (= 60,000), the modulation response improves but only over a narrow bandwidth at around $f_M \approx$ FSR. This shows that the FSRC method can achieve very high Q_L and f_M product, and completely breaks the power-frequency tradeoff. If we pick a very high Q_L of 60,000 for low power consumption, the f_M can also be as high as the FSR, but not the resonance linewidth. Of course, this method is narrow bandwidth as shown in Fig. 4.2(b), and signal distortion is still expected when performing digital data momdulation at high data rates. In addition, since the microring size scales with FSR (FSR = $c/(n_g L)$), this method will become promosing when f_M is very high as will be discussed in future sections.

4.3 Device design and fabrication

To demonstrate the FSR coupling modulator, an silicon microring modulator with an FSR of 26 GHz is designed and fabricated, then its performance is compared to a standard microring modulator. The optical microscope image of the fabricated the device is shown in Fig. 4.3(a). The radius of the microring is 445

μm in order to obtain an FSR of 26 GHz, and one quarter of the microring is covered with an electrode ($S = L/4$). In this quarter region, a PN diode is also formed inside the silicon waveguide as shown in Fig. 4.3(b) to provide fast modulation speed operating in the depletion mode (see Chapter 1 and 3 for details about the depletion mode microring modulator and the fabrication steps). The doping level of the P- and N- doping are 8×10^{17} $1/cm^3$, and that of the P+- and N+- doped regions are 1×10^{20} $1/cm^3$. I chose $S = L/4$ over $S = L/2$, which has both higher coupling and modulation efficiency as indicated in Fig. 4.2(a), to prove the concept of the FSRC modulator since $S = L/4$ not only has sufficient coupling, but it also provides higher electrical bandwidth (lower capacitance). Another reason for using S = L/4 is to keep the electrode length shorter such that the modulator can still be considered as *lumped*. This means that the electrical wavelength of the RF signal (λ_{RF}) has to be much larger than the modulator length (S). Therefore, we can write down the condition:

$$S_{eff} = \frac{1}{2}\frac{S}{L}\frac{c}{n_g FSR} << \lambda_{RF} = \frac{c}{n_{eff,RF} f_M}, \tag{4.8}$$

where $n_{eff,RF}$ is the effective index of the RF wave, and S_{eff} is the effective electrode length that accounts for the fact that signal is fed through the center of the electrode (see Fig. 4.3(a)). Since $FSR \approx f_M$, we can rearrange Eq. (4.8) and get:

$$\frac{S}{L} << 2\frac{n_g}{n_{eff,RF}} \tag{4.9}$$

From Eq. (4.9), since n_g is usually larger than $n_{eff,RF}$, but not by much, we can expect that S/L has to be much smaller than one. Therefore, for the case where $S = L/4$, we can expect the condition to be fulfilled with $S_{eff} \approx 0.1 \times \lambda_{RF}$. From

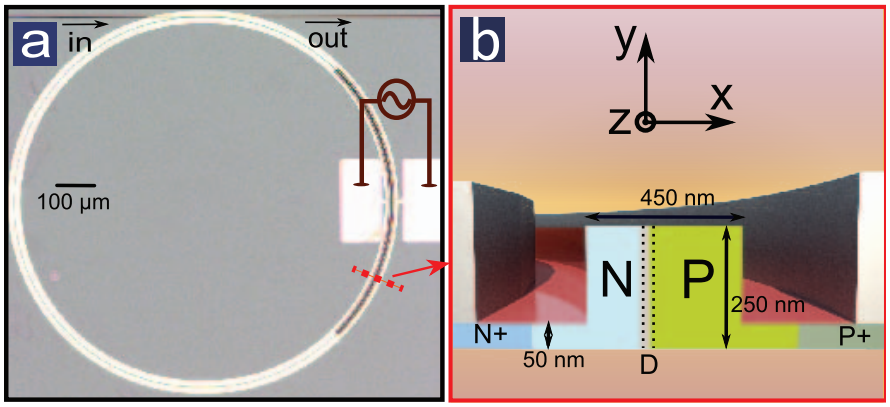

Figure 4.3: Optical microscope image of the fabricated device. (b) Illustration of the crosssection of the modulated region

eq. (4.9), a large n_g will help because it decreases the overall size of the resonator compared to the electrical wavelength. Alternatively, a long electrode can be splitted into small parts if longer a longer modulation length is desired, and each is driven with a separate driver.

The silicon microring has a cross-sectional dimension of 200 nm $\times$ 450 nm on top of a 50 nm silicon slab. This waveguide supports a single TE mode. Note that the current modulator design is no longer compact. However, the radius can be reduced if the modulator is designed at higher f_M. For example, the radius of the FSRC modulator $\approx$ 114 μm at FSR = 100 GHz, which is smaller than the size of regular silicon MZI modulators. We also fabricate a standard ring modulator with a small radius of 15 μm with a very large FSR of 750 GHz for comparison.

The other important criteria to observe the FSRC effect is to design and facbricate a microring modulator with 1) its modulation frequency higher than its FSR, and 2) its resonance linewidth is much smaller than the FSR. For the first point, we need to design the microring modulator to have smaller FSR that lies

inside the electrical 3 dB bandwidth. Since depletion mode silicon modulators have been demonstrated with $f_M > 50$ Gbps [70], we pick an FSR $\approx$ 26 GHz. In addition, based on 2), since we are dealing with very small FSRs, the resonance linewidth has to be much smaller than the FSR, otherwise, all the FSR modes naturally overlaps and the laser will couple to more than one FSR modes from the bus-waveguide. For a typical depletion mode silicon modulator, a Q_L of $\approx$ 15,000 [55] has been demonstrated with a resonance linewidth of around 15 GHz, which is still smaller than the designed FSR of 26 GHz.

4.4 Experimental methods

The experiment is performed with the use of both optical and high speed RF instruments/components. As shown in Fig. 4.4(a), to test the EO response of the silicon FSRC modulators, we use a 67 GHz Network analyzer (Agilent E8361C). One port of the network analyzer is connected with a bias-tee and a high speed RF probe (50 GHz, GGB Industries, Inc.) A source meter (Kiethley 2400) is connected to the bias-tee to source a bias voltage and measure the current at the same time. All the cables, connectors, and adapters are rated higher than 40 GHz. The probe is then touched down on the silicon chip. For the optical path, the coherent light source is a tunable laser (ANDO AQ4321A). Then light goes through a polarization control and filter, then it reaches the input facet of the silicon chip. Note that everything is fiber-coupled. The coupling between the optical fiber and the silicon chip is achieved by having a lensed fiber on the fiber side and a tapered waveguide on the chip facet. The details of the fabrication of the tapered waveguide can be found in [113]. The coupling between the output chip facet and the optical fiber is achieved in the same way. Later,

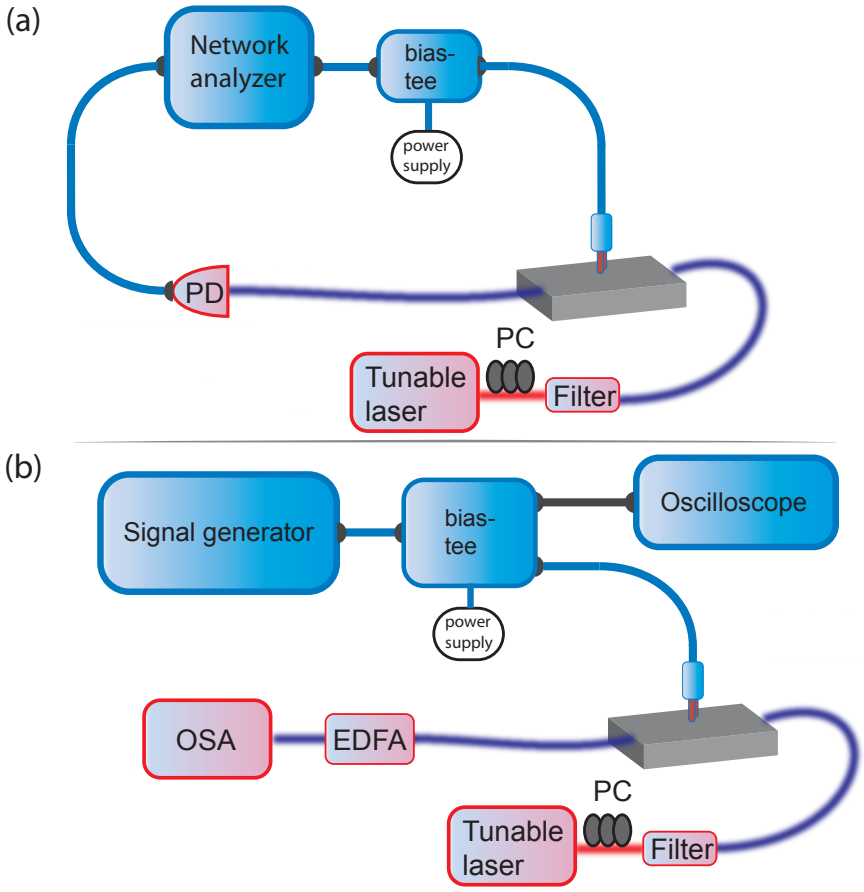

Figure 4.4: Illustration of the test setups for (a) measuring the modulator EO response, and (b) detecting the modulation sidebands of the silicon modulators.

the optical fiber goes into a high speed InGaAs photodetector (NewFocus 1014, 45 GHz.) The output of the photodetector is the converted electrical signal that corresponds to the slowly varying amplitude of the optical wave. This electrical signal is then connected back to the other port of the network analyzer. Here, the transmission measured from the network analyzer (S_{21}) is the EO response. To directly see the sidebands, we alternate the setup slightly as shown in Fig. 4.4(b). In this figure, for the electrical part, a signal generator is used to provide the pure sinusoid voltage instead of using a network analyzer. After the bias-

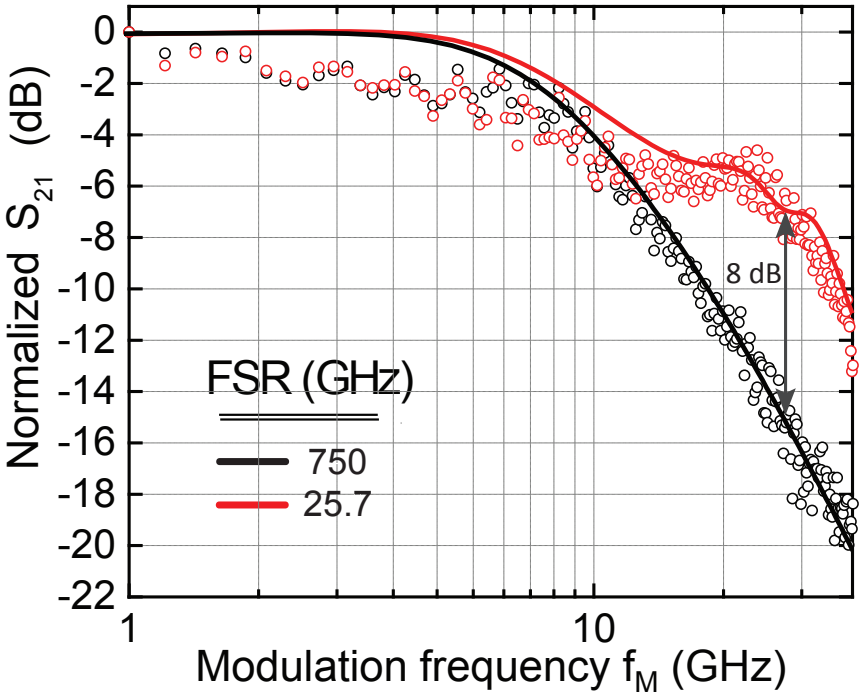

Figure 4.5: Measured (circles) and theoretical (solid) EO response of the FSRC modulator (red) and the standard microring modulator (black). The detail of the test setup is shown in Fig. 4.4(a).

tee, a small portion of the signal splits into the oscilloscope to view the signal. For the optical part, an the output light from the silicon chip is going through an EDFA (Erbium-doped fiber amplifiers) then into an OSA (optical spectrum analyzer, ANDO AQ6317B). The noise and resolution of the OSAs are generally poorer than electrical spectrum analyzers, therefore, a signal generator and an EFDA are used to achieve a stronger modulation. All other components are the same as shown in Fig. 4.4(a).

4.5 Results and discussions

The FSRC modulator exhibits an enhancement of the modulation at 20 GHz larger than the resonance linewidth of 11.7 GHz (calculated from a Q_L of 16,000). The modulation EO response (normalized to the response at 1 GHz) for both the FSRC modulator (red) and the standard modulator (black) are shown in Fig. 4.5. The applyied small signal RF wave is about -17 dBm, and the matrix element S_{21} is measured from the network analyzer. The laser wavelength is biased on the slope of one of the resonance curve. The detail of the measurement setup is discussed in the previous section and depicted in Fig. 4.4(a). The two response curves shown in Fig. 4.5 have similar traces at f_M up to the resonance linewidth of 11.7 GHz. This is expected because both the FSRC and the standard modulator have the same Q_L of 16,000 as shown in the insets of Fig. 4.6(a) and 4.6(b). However, when $f_M > 11.7$ GHz, the modulation response of the standard modulator decreases, with a sharp roll-off as expected. In contrast, the response of the FSRC modulator increases with a local maximum at 20 GHz. One can see a significant improvement in the normalized modulation response of 8 dB for the FSRC modulator compared to the standard modulator at 27 GHz (see the arrows indicated on the Fig. 4.5). Note that the data in Fig. 4.5 show steeper roll-offs when compared to the calculation in Fig. 4.2(b). This is attributed to the fact the devices are limited by the RC bandwidth (BW = $1/(2\pi RC)$). The measured electrical resistance and capacitance are 11 Ω and 190 fF for the FSRC modulator, respectively, and are 545 Ω and 17 fF for the standard modulator, respectively. These numbers correspond to an RC bandwidth (in a 50 Ω system) of 14 GHz and 16 GHz for the FSRC and the standard modulators, respectively. The theory curves (solid lines in Fig. 4.5) are calculated by incorporating the RC response

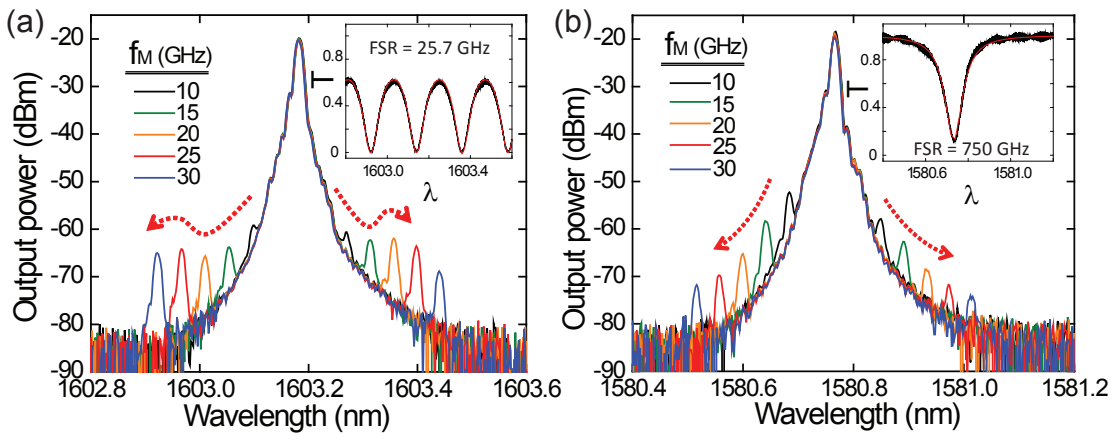

Figure 4.6: Measured optical spectra for (a) the FSRC modulator, and (b) the standard microring modulator under different modulation frequencies. The optical transmission spectra through the bus-waveguide is shown in the insets. Based on the insets, the loaded quality factor $Q_L \approx 16{,}000$

to the methods adopted to obtain the results shown in Fig. 4.2(b). One can see good agreements between the experiments and the theory curves. The RC effect can be mitigated by further improving the fabrication and optimizing the device structure to lower both the overall resistance and the capacitance. The measurements are only performed up to 35 GHz because of the limitations mainly contributed from the photodetector. However, this measurement demonstrates that it is indeed possible to use the photonic transitions between the FSR modes to modulate at f_M much higher than the resonance linewidth.

To prove that the enhancement of the modulation response shown in Fig. 4.5 is resulted from the photonic transitions between the FSR modes, the optical spectra of our devices under RF modulations are measured. The measurements are done by applying 5 dBm RF sinusoid signal (power higher than this will result in resonance drifting due to the thermal-optic effect) from the signal generator to the device (the detail of the test setup is shown in Fig. 4.4(b).) The

spectra for the FSRC and the standard modulator are shown in Figs. 4.6(a) and 4.6(b), respectively. In both figures, the broad peaks in the middle of the spectra are located at the laser wavelength biased on the slope of the resonance curve. The smaller peaks located on both the left and the right sides of the broad peaks are the modulation sidebands. In Fig. 4.6(a), which is the optical spectra for the FSRC modulator, the sidebands increase as f_M increases, and they reach local maxima at f_M = 20 GHz (orange) and at f_M = 25 GHz (red) on the right and left side of the broad peak, respectively. This result directly indicate that the sidebands of the FSRC modulator are coupled (*transitioned*) to the nearest neighboring FSR modes at ± 1 FSR away from the laser wavelength. The reason why the maximum of the right and the left sidebands occured at different f_M is because the laser is detuned from the center of the resonance wavelength. In fact, the laser is parked on the right-hand side of the resonance, such that the right sideband will first reach the nearest FSR on the right, then subsequently, the left sideband will reach the nearest FSR on the left. One important thing to note is that the Finesse of the resonator (see Chapter 3, FSR measured to be 25.7 GHz) is small so that the transmission did not reach 100 % (at ≈ 60 %). This resulted in a slight decrease of the modulation efficiency. For the standard modulator (Fig. 4.6(b)), the average power of the sidebands continue to drop from -55.17 dBm to -73.15 dBm as f_M increases from 10 to 30 GHz. This is because the FSR of the standard modulator is much larger than f_M and the sidebands are simply filtered outside of that single resonance.

For high modulation frequencies, the FSRC modulators have lower power consumption compared to the standard silicon microring modulators. Although the EO response of the FSRC modulator is much higher than the standard microring modulator, but the required RF power to drive the FSRC mod-

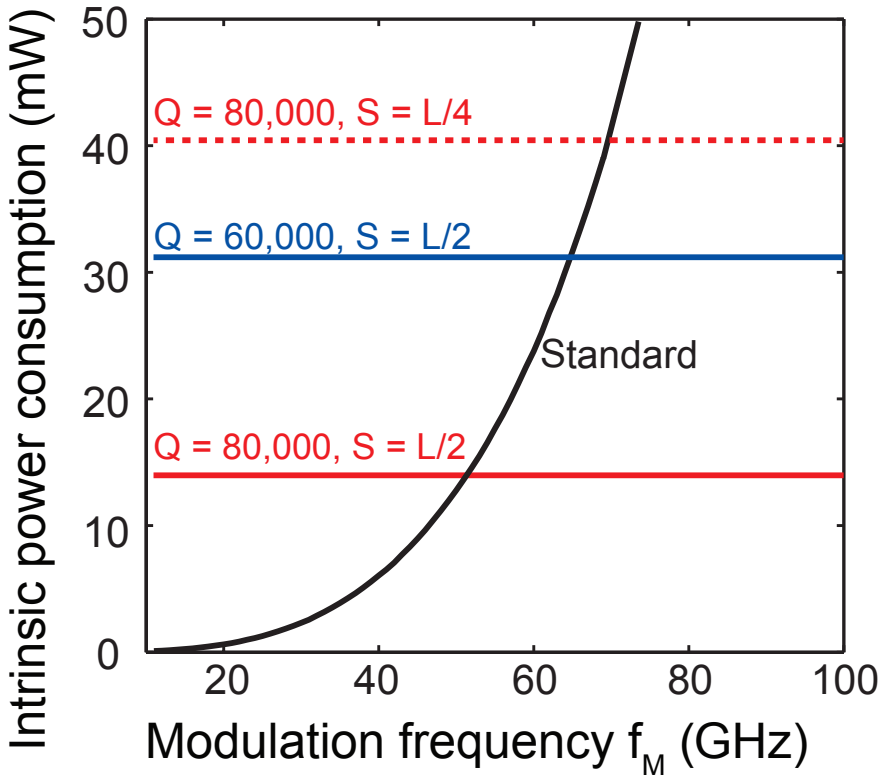

Figure 4.7: Theoretical intrinsic power consumption for the standard silicon ring modulator (black) and the FSRC modulators (colored) with different Q_L and S

ulator can be quite high due to its large ring radius (Fig. 4.3(a)) at low f_M. To show this effect, we plot the theoretical power consumption for both the FSRC modulator (red and blue) and the standard silicon microring modulator (black) at different f_M in Fig. 4.7. For this theoretical analysis, the power consumption is calculated from the following expression:

$$P_{RF} = \frac{1}{2} f_M C_d V_d^2 \tag{4.10}$$

where C_d is the PN diode capacitance, and V_d is the voltage required to shift the resonance frequency by one resonance linewidth in each cycle of a sinusoid modulation (assuming the laser is on resonance when no voltage is applied).

Note that the power consumption defined in Eq. (4.10) is the intrinsic power consumption, which defines the minimum power required to drive the modulator. For example, it does not take into account the power lost in the source and the impedance matching network. The waveguide and doping geometry adopted for the simulations are shown in Fig. 4.3(b). Both the voltage dependence of the carrier distribution and C_d are calculated using SILVACO. These simulated carrier distributions are then imported into COMSOL to calculated both the doping-induced loss and the resonance frequency shift to determine Q_L and V_d, respectively (details about the simulation are discussed earlier in Chapter 3). The standard silicon microring modulator in this analysis has a compact ring radius of 2.5 μm (this is about the smallest for a microring modulator without introducing too much radiation loss [126]), an uniform modulation ($S = L$, in reality, $S \leq L$ because the bus-waveguide also takes space), and a varying Q_L with its resonance linewidth matching the f_M (again, remember that standard modulators cannot modulate faster than the resonance linewidth). On the other hand, the FSRC modulator in this analysis has a varying ring radius such that the FSR is always matched to the desired f_M. In all cases, we include a 1 dB/cm scattering loss to account for the fabrication imperfections of the ring. For our proof-of-concept experiment shown in Figs. 4.5 and 4.6, where $S = L/4$ and Q_L = 16,000, the power consumption for the FSRC modulator is calculated as $\approx$ 600 mW. Note that this power can be significantly reduced by designing the modulator with higher Q_L and by operating the modulator at higher f_M. In Fig. 4.7, we see that when $f_M >$ 51 GHz, the $S = L/2$ FSRC modulator with a Q_L of 80,000 ($C_d \approx$ 214 fF and $V_d \approx$ 1.6 V) has lower power consumption than that of the standard silicon microring modulator ($C_d \approx$ 195 fF and $V_d \approx$ 2.3 V). This is true because in standard microring modulator designs, one needs to lower the

Q_L significantly to accomodate higher f_M. In addition, for higher f_M, the FSR = f_M condition is satsified with smaller rings, and hence smaller C_d. Therefore, the amount of carriers injected and extracted from the depletion region is reduced. Moreover, as shown in Fig. 4.7, the modulator with larger electrode ($S = L/2$) in fact consumes less power: $\approx$ 14 mW (Q_L = 80,000) versus $\approx$ 40.5 mW (Q_L = 80,000) for $S = L/4$ because the modulation efficiency increases as the electrode covers a larger portion of the microring. It is possible to achieve even smaller power consumption by increasing the electrode length. Nevertheless, when S is large (e.g. $S \geq L/2$) such that the electrode length is comparable to the RF wavelength (see Eq. (4.9)), the electrode needs to be further discretized into smaller segments. Alternatively, a waveguide with higher n_g needs to be employed.

4.6 The effect of modulator patterns and RF phases

Both the pattern of the modulator and the applied RF phases on the modulators have a significant impact on the modulator EO response. It has been revealed in Fig. 4.2(a) that the portion of modulation along the microring has a huge impact on the coupling strength (or the photonic transition rate) between adjacent FSR modes. This effect is also well described based on Eq. (4.5), where the $\delta\epsilon(z,t)$ must have a spatial frequency component that matches $(m-n) \times 2\pi/L$. Therefore, one can immediately see that the largest coupling between the directly adjacent FSR modes occurs when $\delta\epsilon = \exp(j2\pi/L)$. This condition is acheivable but difficult because now $\delta\epsilon$ have both a real (phase) and imaginary (loss/gain) part, and the ratio between these parts has to be 1. However, a reasonable approach is to only take care of the real part: $\delta\epsilon = \cos(2\pi/Lz)$. The net effect is it will couple to not only the left-adjacent FSR mode, but also the

right-adjacent FSR mode, and the net power coupling becomes halfed (because $\cos(2\pi/Lz) = 1/2 \times (\exp(j2\pi/Lz) + \exp(-j2\pi/Lz))$). Depending on the application, this effect may be an advantage if one wants to keep the sidebands on both sides of the carrier (for example: a modulator). Practically speaking, $\delta\epsilon = \cos(2\pi/Lz)$ is quite difficult to achieve. Therefore, modulating only a portion of the microring is used for demonstration purpose, since it is much easier to modulate a particular segment uniformly (as shown in the previous section). We see that based on this approach, and from Fig. 4.5, the maximum coupling is about $0.3 \times \Delta\omega_{0,max}$ when $S = L/2$. If we want to acheive an even larger coupling, we need to mimic a $\cos(2\pi/Lz)$ change of the dielectric constant using segmented modulators along the microring (see Fig. 4.8). In addition, the RF phase of each segment needs to be precisely tuned (which is not difficult). To prove this arguement, we can rewrite Eq. (4.5) in the following form:

$$\mu_{nm} = -\frac{\omega_0}{2\epsilon L} \sum_{i=1}^{n_{seg}} \int_{L_i} \delta\epsilon \cos(\omega_{mod} t + \phi_i) e^{j(m-n)\frac{2\pi}{L}z} \, dz, \tag{4.11}$$

where $\delta\epsilon$ is the amplitude of the modulation, ω_{mod} is the modulation frequency, ϕ_i is the phase (time origin) of the modulation, n_{seg} is the number of segments, and L_i is the modultion length for the i_{th} segment. Here we assume all the modulation segment lengths are the same: $L_i = L/n_{seq}$. Eq. (4.11) can be expanded into two terms (using trigometric identity):

$$\mu_{nm} = -\frac{\omega_0}{2\epsilon L} \sum_{i=1}^{n_{seg}} \int_{L_i} \delta\epsilon [\cos(\omega_{mod} t)\cos(\phi_i) - \sin(\omega_{mod} t)\sin(\phi_i)] e^{j(m-n)\frac{2\pi}{L}z} \, dz. \tag{4.12}$$

After rearranging Eq. (4.12), and use the relation $\delta\epsilon\omega_0/(2\epsilon) = \Delta\omega_0$ ($\Delta\omega_0$ is the amplitude of the resonance frequency shift if the whole microring is modulated

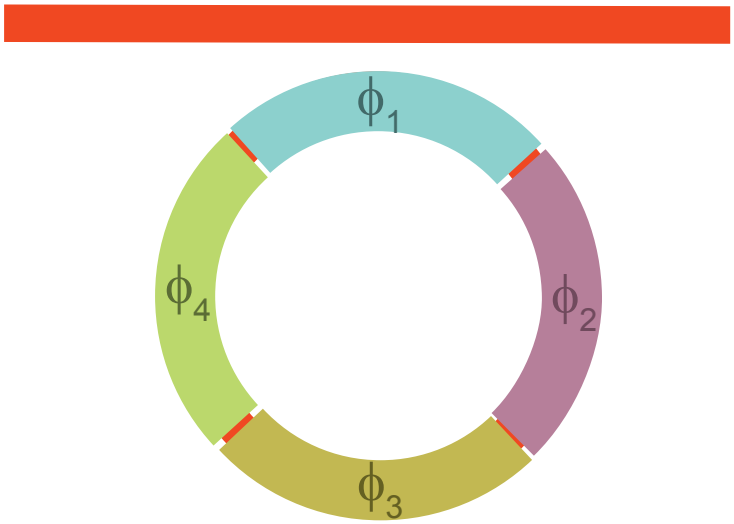

Figure 4.8: Illustration of a segmented microring modulator. In this particular example, there are a four modulator segments, and each segment are applied with an individual RF signal with RF phase ϕ_i.

uniformly), the following equation is achieved:

$$\mu_{nm} = -\frac{\Delta\omega_0}{L}\left[\cos(\omega_{mod}t)\sum_{i=1}^{n_{seg}}\int_{L_i}\cos(\phi_i)e^{j(m-n)\frac{2\pi}{L}z}dz - \sin(\omega_{mod}t)\sum_{i=1}^{n_{seg}}\int_{L_i}\sin(\phi_i)e^{j(m-n)\frac{2\pi}{L}z}\,dz\right]. \tag{4.13}$$

Eq. (4.13) can be treated as the substraction of two sinusoids, and each sinusoids have a constant associated. These constants can be defined as:

$$\Gamma = \sum_{i=1}^{n_{seg}}\int_{L_i}\cos(\phi_i)e^{j(m-n)\frac{2\pi}{L}z}dz, \tag{4.14}$$

$$\Psi = \sum_{i=1}^{n_{seg}}\int_{L_i}\sin(\phi_i)e^{j(m-n)\frac{2\pi}{L}z}\,dz. \tag{4.15}$$

From Eqs. (4.13)-(4.15), and using another trigometric identity $a\cos(x)+b\sin(x) = \sqrt{a^2+b^2}\cos(x-\arctan(b/a))$, the coupling strength between the adjacent FSR

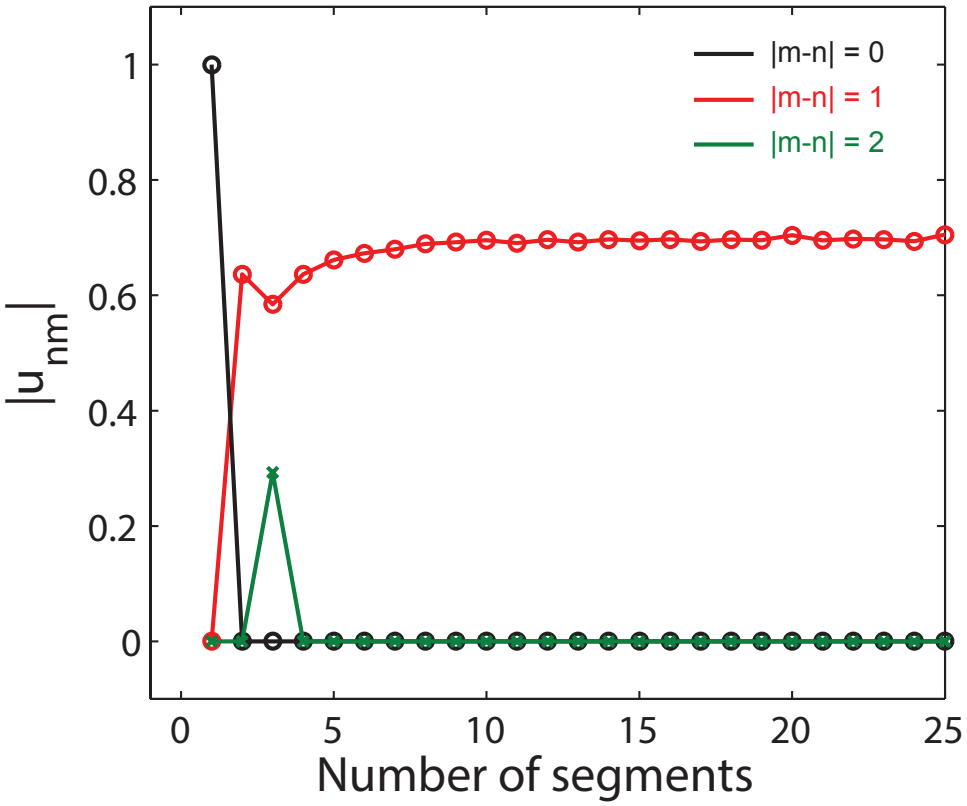

Figure 4.9: Calculated $|\mu_{nm}|$ versus different number of modulator segments for the coupling between itself (black), nearest adjacent FSR (red), and second nearest adjacent FSR (green) modes.

modes can be obtained as:

$$|\mu_{nm}| = \sqrt{\mathrm{Re}(\Gamma)^2 + \mathrm{Im}(\Gamma)^2 + \mathrm{Re}(\Psi)^2 + \mathrm{Im}(\Psi)^2} \tag{4.16}$$

The results are plotted in Fig. 4.9, where the phases for each of the segments are defined as (again, to mimic a $\cos(2\pi/Lz)$ change of the dielectric constant):

$$\phi_i = i \times 2\pi/n_{seg}. \tag{4.17}$$

From Fig. 4.9, the mode coupling between the nearest FSR modes ($|m - n| = 1$) increases quickly as the number of segments increases, and it also plateaued quickly as soon as it reaches $n_{seg} = 4$ (in fact, it is not very different between

2 and 4 segments). The curve for $|m - n| = 1$ saturates at around $0.7 = 1/\sqrt{2}$, which gives exactly half the power coupling. This result matches the discussion earlier in this section, in which the coupling has to be equally distributed into both sidebands (on the right- and left- hand side of the laser frequency) because the modualation term is pure real. Another interesting thing is that the self-coupling term ($|m - n| = 0$, means the amount of resonance frequency shift) is always 0 when the number of segments is not 1 ($n_{seg} = 1$ means uniform modulation, where both zero coupling between the FSR modes and maximum resonance frequency shift are expected). This is to be expected because of the way ϕ_i is defined (see Eq. (4.17)). For every light roundtrip inside the microring, the positive and negative change of dielectric constant is always equal, which leads to a cancellation of the net resonance frequency shift. Therefore, we would expect that the modulation response to be zero when f_M is smaller than the resonance linewidth. In other words, while all the microring resonances are all *static*, the couplings between the nearest adjacent FSR modes are very active. For $|m - n| = 2$, the coupling strength is always small except at 3 segments.

4.7 Summary

In this chapter, a method to modulate light in a silicon microring beyond the resonance linewidth is both theoretically and experimentally demonstrated. This physics of this method is also equivalent to inducing photonic transitions between the adjacent FSR modes. The experiment demonstrates a modulation at frequencies around 26 GHz, and it is much larger than the resonance linewidth at 11.7 GHz. The experimental results are proved that they are directly related to the photonic transitions by looking at the optical spectrum of the modulated

light. A discussion of how this method compares to the conventional silicon microring modulators are subsequently made using theoretical models, and it shows that the FSRC method will consume much less power compared to the conventional silicon microring modulators if both the Q_L and the operating RF carrier frequency is high. Lastly, the maximum coupling strength of this FSRC approach is theoretically explored, which indicates that both the modulator pattern and the applied RF phase are equally important. The aforementioned results show the advantage of using silicon waveguides. It is not only because it can be compact (higher refractive index compared to other electro-optical materials), but also the doping can be locally adjusted such that an arbitrary distribution of the refractive index change can be achieved. This advantage will be discussed and become more obvious in the next few Chapters.

CHAPTER 5

AN EFFECTIVE MAGNETIC FIELD FOR LIGHT

Photons are neutral particles that do not interact directly with a magnetic field. However, recent theoretical work [127–130] have shown that an *effective* magnetic field for photons do exist if the phase of light would change with its propagating direction. This direction-dependent phase indicates the presence of an effective magnetic field as shown for electrons experimentally in the Aharonov-Bohm experiment [131]. Here we replicate this experiment using photons on-chip. We construct an on-chip Ramsey-type interferometer [132–135] using silicon photonics to prove that this non-reciprocal phase exist. This interferometer has been traditionally used to probe the phase of atoms in a specific atomic states, and here we apply it to probe the phase of light in different photonic states. Later in this chapter, I will show the experimental observation of an effective magnetic flux for photons, which can be adjusted between 0 to 2π, corresponding to a non-reciprocal 2π phase shift within an interferometer length of 8.35 mm and an interfernce-fringe extinction ratio of 2.4 dB. This non-reciprocal phase achieved is comparable with monolithically-integrated magneto-optical (MO) materials shown in the literature [97].

5.1 Introduction to an effective magnetic field for light

The interaction of light and magnetic field would enable new physical phenomenon for photons such as bending the direction of light and one-way edge modes. Since photons are neutral particles, the interaction between photons and a magnetic field relies on using MO materials. It is known that MO materials are difficult to integrate on-chip and the MO effect is typically weak in the near-IR

and the visible wavelengths. One important application of using MO materials is to make isolators, which is a device that allows light transmission only in one direction. Isolator schemes using dynamic refractive index modulation instead of incorporating MO materials were demonstrated in both optical fibers [136] and more recently in on-chip silicon and InP waveguides [93–98]. Recent efforts have been exploring the designs of isolators without using MO materials [81,104,106–108]. Nevertheless, these works do not demonstrate an effective magnetic field for photons, and their performance is far lower than the MO materials. This leads to the fundamental question of whether one can generate an effective magnetic field directly coupled with photons in the optical domain while not limited to using MO materials. Recently, an effective magnetic flux for both RF photons and photon-phonon interaction was observed using a photonic Aharonov-Bohm interferometer [137,138]. However, the demonstration of such an effect in the on-chip optical domain will provide new functionalities for on-chip light manipulation. In the following sections, a method, and its theory, to generate such an effective magnetic field is discussed. Then an experimental demonstration is subsequently shown.

5.2 The theory of photonic transitions enabled effective magnetic field for light

As shown by Fang et al. [127,128], an effective magnetic field for photons could be created, if one could break the reciprocity of light such that its phase would depend on its propagation direction. The link between the magnetic field $\vec{B}$ (and its associated gauge potential ($\vec{A}$)) and the direction-dependent phase is equiv-

alent to the Aharomov-Bohm (AB) effect for electrons [131], where the electrons acquire a direction-dependent phase in the presence of a external magnetic field:

$$\Phi_{electron} = \frac{e}{h}\int_{r}^{r'} \vec{A}\cdot\, d\hat{r}, \tag{5.1}$$

where $\vec{B} = \nabla \times \vec{A}$, e is the unit charge, $\vec{A}$ is the vector potetnial ($\vec{B} = \nabla \times \vec{A}$) and h is the Planck constant. Notice that from Eq. (5.1), the phase $\Phi_{electron}$ is non-recirprocal, and the electrons will pick up a $-\Phi_{electron}$ when it is propagating backwards. In the presence of a magnetic field, the Hamiltonian for electrons *hopping* through the nearest neighboring lattice points (with lattice constant Λ) in space (discretized) can be written as:

$$H = \sum_{r',r} t_{r',r} b_{r'}^{\dagger} b_r, \tag{5.2}$$

and

$$t_{r',r} = -\frac{\hbar^2}{2m^*\Lambda^2} e^{j\Phi_{electron}} \tag{5.3}$$

In Eqs. (5.2) and (5.3), $b_{r'}^{\dagger}$ and b_r are the annihilation operators for lattice points r' and r, respectively, and m^* is the effective electron mass.

By inducing photonic transitions between two photonic states, the photons both pick up a phase with an expression similar to Eq. (5.1) and possess a Hamiltonian similar to Eq. (5.2) as it propagates in space, and an effective magnetic feld is generated. If we recall from Chapter 2, photonic transitions between photons in the two optical levels (or modes) occurs during dynamic refractive index modulation. In addition, based on Eqs. (2.17) and (2.18), the transitioned photons also picks up an RF *phase*, and this RF phase is fundamentally non-reciprocal. This is illustrated in Fig. 5.1 to further clarify. In Fig. 5.1(a), the imparted RF phase on the excited photons (transition from lower to higher energy

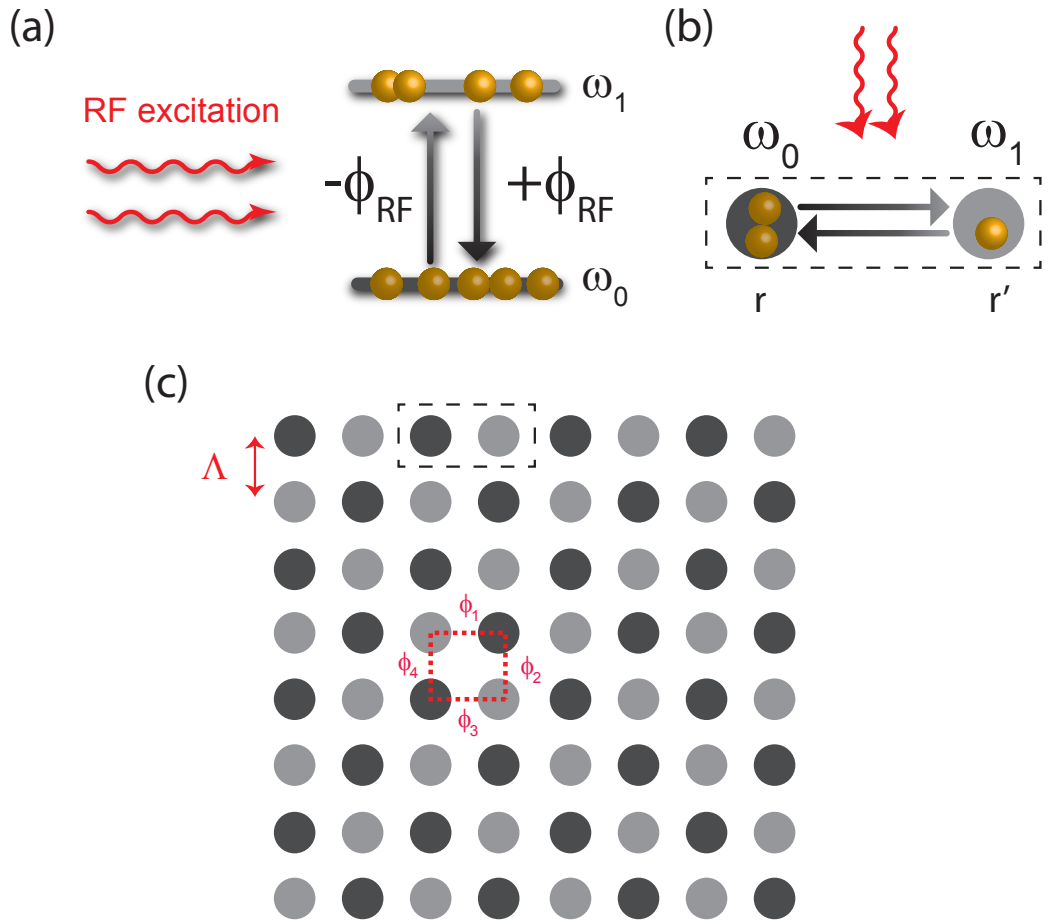

Figure 5.1: (a) The imparted RF phases for photonic transitions in a photonic two-level system (the higher energy level (light grey) and the lower energy level (dark grey)). (b) A direction-dependent phase based on the photonic transition in a photonic two-level system. (c) An effective magnetic field for photons is achieved by interleaving the two photonic levels into a two-dimensional square lattice with lattice constant Λ.

level) has an opposite sign of the de-excited photons (transition from higher to lower energy level). Therefore, if the two photonic levels are positioned in two distinct places in space, a non-reciprocal phase is naturally formed. For example, as shown in Fig. 5.1 (b), if we have the lower energy photonic state (dark grey) on the left, and the higher energy photonic state (light grey) on the right, then photons transitioned from left to right due to the RF excitation will pick up

a $-\phi_{RF}$ phase, while photons transitioned from right to left will pick up an opposite $+\phi_{RF}$ phase. As a result, a non-reciprocal phase very similar to electrons interacting with the $\vec{A}$ field is achieved, and we can write down an expression for the equivalent vector potential for photons ($\overrightarrow{A_{eff}}$) just like Eq. (5.1):

$$\Phi_{RF} = \int_{r}^{r'} \overrightarrow{A_{eff}} \cdot d\hat{r}, \tag{5.4}$$

Now, we can also write the Hamiltonian of the photons in this photonic two-level system (Fig. 5.1(b)) based on Eqs. (2.17) and (2.18) as:

$$H = \kappa e^{-j\phi_{RF}} \hat{a}_1^\dagger \hat{a}_2 + \kappa e^{+j\phi_{RF}} \hat{a}_2^\dagger \hat{a}_1, \tag{5.5}$$

where $\hat{a}_1$ and $\hat{a}_2$ are the annihilation operators for the lower and the higher energy photonic states, respectively. As a sanity check, if we plug Eq. (5.5) back into the Heisenberg equation of motion, we get the time domain version of Eqs. (2.17) and Eq. (2.18). Now Eq. (5.5) is very similar to Eq. (5.2) if the two photonic levels are arranged in a square lattice as shown in Fig. 5.1(c). In other words, Eq. (5.5) is the Hamiltonian that describes one unit cell (dashed black line) of the entire lattice, and the overall Hamiltonian for photons will have the form that look exactly like Eq. (5.2). Therfore, photons will have an effective magnetic field, meaning that photons traveling in this lattice (Fig. 5.1(c)) will *look* exactly like electrons traveling thorugh a space that is subjected to a real magnetic $\vec{B}$ field. Now, to define this effective magnetic field for photons, we start from determining the total phase (Eq. (5.4)) a photon acquires if it travels through a closed loop defined in Fiig. 5.1(c) (red dashed box):

$$\phi_1 - \phi_2 + \phi_3 - \phi_4 = \oint_{1\to4} \overrightarrow{A_{eff}} \cdot d\hat{l}. \tag{5.6}$$

Notice that now the individual integrals grabbed from Eq. (5.4) now becomes a

closed loop integral. Then based on the relation similar to the case for electrons:

$$\overrightarrow{B_{eff}} = \nabla \times \overrightarrow{A_{eff}}, \tag{5.7}$$

and by modifying Eq. (5.6) with the Stokes' theorem, then plugging Eq. (5.7) into Eq. (5.6), the following expression is obtained:

$$\phi_1 - \phi_2 + \phi_3 - \phi_4 = \iint_{plaquette} \overrightarrow{B_{eff}} \cdot \hat{n}\, dS = B_{flux,eff}, \tag{5.8}$$

where *plaquette* is the area enclosed by that smallest available loop (enclosed by the red dashed line), and $\hat{n}$ is the unit vector pointing out of that surface. The right hand side of Eq. (5.8) is exactly the form of a magnetic flux. As a result, the effective magnetic flux ($B_{flux,eff}$) is the total non-recirpocal phase a photon accumulated through a closed loop. In addition, the effective magnetic field for photons is pointing verticallly through the surface of the two-dimensional lattice shown in Fig. 5.1(c). Since $\overrightarrow{B_{eff}}$ must be considered uniform inside that smallest available loop (plaquette, red dashed line), we can then write:

$$\overrightarrow{B_{eff}}\Big|_{plaquette} = \frac{B_{flux,eff}}{\Lambda^2} \tag{5.9}$$

The interesting thing about B_{eff} is that its amplitude and distribution can be arbitrarily defined by the area (per *plaquette*) and the phases of all the photonic transitions inside this two-dimensional lattice. Therefore, light trajectory can be manipulated in a way that would be otherwise very difficult to achieve with electrons that interact with a real magnetic field. A few interesting light behaviour using the effective magnetic field is discussed in the next chapter.

Another interesting point to make is that even if the two photonic levels in Fig. 5.1(b) happened to be at the same location, (namely, $r = r'$), ϕ_{RF} is still finite

and $\overrightarrow{A_{eff}}$ becomes singular. This means that the effective magnetic flux exists no matter how the two photonic leves are distributed in space. However, the effective magnetic field becomes non-existent in this case because there are no enclosed areas that can be defined.

5.3 Design and fabrication

To prove the existence of a effective magnetic field for light, we first show that this non-reciprocal phase induced by the photonic transitions in a photonic two-level system [139]. The non-reciprocal phase induced by dynamic modulations is already been observed in RF photons [137] using a photonic Aharonov-Bohm interferometer. However, this experiment is performed with bulky RF cables and components, which is extremely difficult to integrate into a two-dimensional lattice such as shown in Fig. 5.1(c). Additionally, the non-reciprocal phase generated by MO materials are much weaker in the optical than the RF domain. Therefore, it is attractive if we can demonstrate this effect on-chip using micro-meter scale waveguide components in the optical domain. In this case, it is also ideal for using silicon photonics, not only because it can be directly integrated with CMOS electronics to provide complex phase controls, but also the waveguides can be doped into particular spatial geometries that provide efficient coupling between the two photonic levels.

Here the non-reciprocal phase of light is probed using a photonic Ramsey-type interferometer [132, 134]. The basic form of a Ramsey-type interferometer is shown in Fig. 5.2(a). In an atomic Ramsey interferometer, as an atom in the ground state enters the interferometer, the first laser (left) interacts with it, and

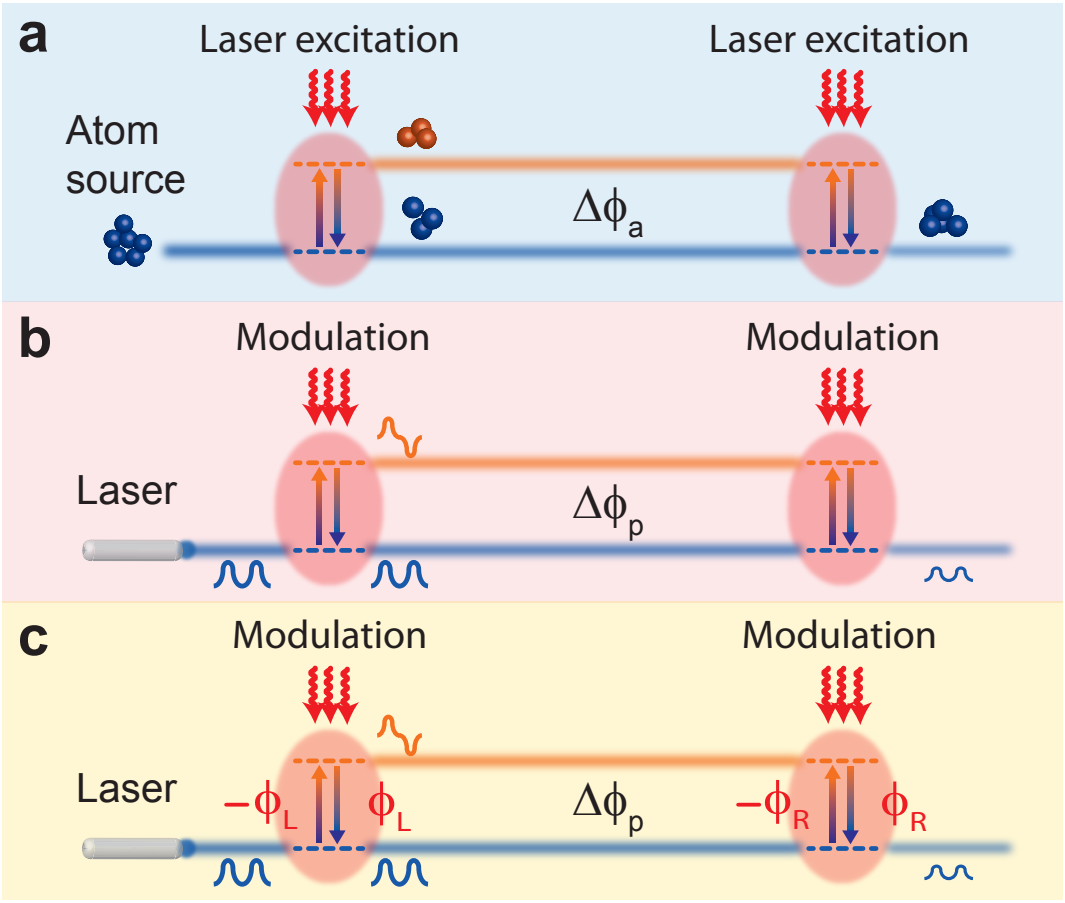

Figure 5.2: Illustrations of (a) an atomic Ramsey interferometer, (b) a photonic Ramsey interferometer, and (c) a photonic Ramsey interferometer where the two modulators have different RF phases ϕ_L and ϕ_R.

the atomic state is rendered in a linear superposition of a ground and excited state (see the atomic transition discussed in Chapter 2). Atoms in these two states have different propagation phases ($\Delta\phi_a$, due to rotation and gravitation for example). A second laser excitation, in phase with the first, once more transforms the atomic ground and excited states into linear superpositions. Thus, the probability of finding an atom exiting the interferometer in the ground state exhibits an interference profile depending on $\cos(\Delta\phi_a)$. On the other hand, in a photonic Ramsey interferometer (Fig. 5.2(b)), we replace the two atomic states

and laser excitations with two photonic states (in this case, even- and odd-mode in a waveguide (also shown in Fig. 5.3)) and modulators, respectively. As light in the even-mode (lower energy state) enters the interferometer, the first modulator (left) induces a refractive index perturbatiton and couples a portion of light fromthe even-mode to the odd-mode (higher energy state). This process is, again, referred to as the photonic transitions in Chapter 2. Note that this transition is classical in contrast to the atomic Ramsey interferometer. Following the excitation (i.e., coupling or transitioning), similar to the atomic case, the propagating light is in a superposition of both the even- and the odd-mode. The two modes then experience different phases ($\Delta\phi_p$) owing to their different propagation constants. A second modulator on the right couples part of the light in the odd-mode back into the even-mode and light exiting the interferometer in the even-mode exhibits an interference profile, as in the atomic version but now depending on $\cos(\Delta\phi_p)$.

The photonic Ramesy-type interferometer breaks the reciprocity of light and induces an effective magnetic field. This is achieved if the two modulators have different phases ϕ_L and ϕ_R (Fig. 5.2(c)). As mentioned earlier as well as in Chapter 2, the modulation phase will be imparted on the transitioned photons with respect to the phase of the local oscillator that drives the modulator. More importantly, the imparted phase on the transitioned photons is negative if excitation (transition from lower energy level to higher energy level) occurs or positive if de-excitation (transition from higher energy level to lower energy level) occurs. If the phases of both modulators are identical as shown in Fig. 5.2(b), then the effect of the imparted phases are cancelled. However, if the modulators have different phases (Fig. 5.2(c)), these imparted phases are detected and the transmission through the interferometer becomes direction-dependent. For

example, if light enters the interferometer from the left, the output of the interferometer is proportional to $\cos(\Delta\phi_p - \phi_L + \phi_R)$, and if light enters from the right, it is proportional to $\cos(\Delta\phi_p - \phi_R + \phi_L)$.

To show that the photonic Ramsey-type intereferometer creates a nonreciprocal fringe pattern, we can incorporate the transfer matrix shown in Eqs. (2.19) and (2.20) into our interferometer system. For obtaining the maximum visibility of our interference fringes, the modulator length has to satisfy $z = \pi/(4|\kappa|)$, which provides a 50 % transition between teh two photonic states. Therefore, the total transfer matrix of the photonic Ramsey-type interferometer becomes:

$$T_{L\to R} = T_R T_f T_L = \begin{pmatrix} \frac{1}{\sqrt{2}} & j\frac{1}{\sqrt{2}}e^{-j\phi_R} \\ j\frac{1}{\sqrt{2}}e^{-j\phi_R} & \frac{1}{\sqrt{2}} \end{pmatrix} \cdot \begin{pmatrix} e^{j\phi_1} & 0 \\ 0 & e^{j\phi_2} \end{pmatrix} \cdot \begin{pmatrix} \frac{1}{\sqrt{2}} & j\frac{1}{\sqrt{2}}e^{-j\phi_L} \\ j\frac{1}{\sqrt{2}}e^{-j\phi_L} & \frac{1}{\sqrt{2}} \end{pmatrix}, \quad (5.10)$$

where $T_{R(L)}$ is the transfer matrix for the right (left) modulator, and $\phi_{1(2)}$ is the freely propagation phase of mode 1(2) (1 represents the even mode, and 2 represents the odd mode, and $\Delta\phi_p = \phi_2 - \phi_1$). If light is injected in the reverse direction, the total transfer matrix becomes:

$$T_{L\to R} = T_L T_f T_R = \begin{pmatrix} \frac{1}{\sqrt{2}} & j\frac{1}{\sqrt{2}}e^{-j\phi_L} \\ j\frac{1}{\sqrt{2}}e^{-j\phi_L} & \frac{1}{\sqrt{2}} \end{pmatrix} \cdot \begin{pmatrix} e^{j\phi_1} & 0 \\ 0 & e^{j\phi_2} \end{pmatrix} \cdot \begin{pmatrix} \frac{1}{\sqrt{2}} & j\frac{1}{\sqrt{2}}e^{-j\phi_R} \\ j\frac{1}{\sqrt{2}}e^{-j\phi_R} & \frac{1}{\sqrt{2}} \end{pmatrix}. \quad (5.11)$$

The essence of Eqs. (5.10) and (5.11) is that although both ϕ_L and ϕ_R can be chosen arbitrarily, the phase difference between the two pathways now depends on a fixed $\phi_L - \phi_R$ value. If we also define a virtual loop in Fig. 5.2(c), then based on Eqs. (5.4) and (5.7), we can write:

$$\phi_L - \phi_R = \int_1^2 \overrightarrow{A_{eff}} \cdot dr + \int_2^1 \overrightarrow{A_{eff}} \cdot dr = \oint \overrightarrow{A_{eff}} \cdot dl = B_{flux,eff}, \quad (5.12)$$

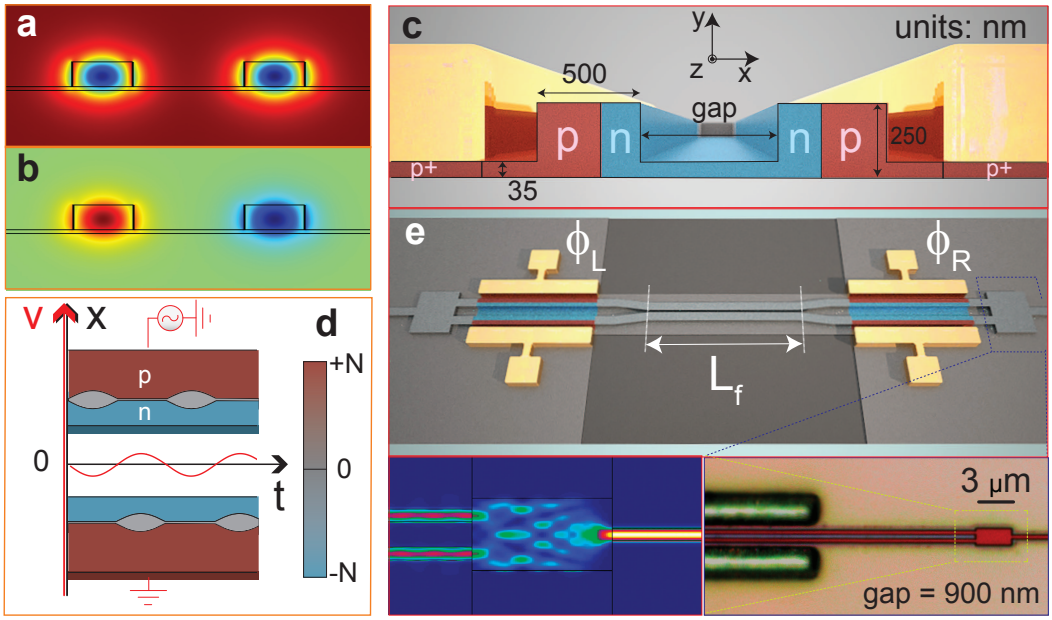

Figure 5.3: Design and fabrication of a photonic Ramsey-type interferometer. Simulated mode profile for both (a) the even-mode and (b) the odd-mode which coexist in a silicon coupled-waveguides structure. (c) Cross-sectional view of the coupled-waveguides. A set of PN and NP diodes is doped in this coupled-waveguides to modulate the refractive index. (d) Top view of the carrier density (N) distribution of the coupled-waveguides along the x-axis (the slab is omitted for simplicity). The width of the depletion region (grey) changes over time as a sinusoidal signal is applied to the diodes. The applied sinusoid voltage (V) is shown in red. (e) Illustration of a photonic Ramsey-type interferometer implemented by a silicon coupled-waveguides structure. The insets show the microscope image and the simulated light transmission through a pair of multi-mode interference devices located at the outer ends of the interferomter.

From Eq. (5.12), as we briefly discussed in the end of the previous section, we see that even though the photonic transitions in the photonic Ramsey-type interferometer are co-located spatially, we are still able to define an effective magnetic flux since ϕ_R and ϕ_L is always finite. Therfore, we can also say that the photonic Ramsey-type interferometer breaks the non-reciprocity because pho-

tons are coupled to this effective magnetic flux.

The photonic Ramsey-type interferometer is implemented by using the supermodes (even- and odd-modes) in a silicon coupled-waveguide structure. Their mode profiles are shown in Figs. 5.3(a) and 5.3(b), and the dimensions of the waveguide are shown in the cross-sectional view in Fig. 5.3(c). The modulators are formed by embedding PN and NP diodes in the waveguides (Fig. 5.3(c)). Figure 5.3(d) shows the top view of the carrier distribution under an applied sinusoid voltage (red). The width of the depletion region (grey) changes as signal is applied, which induces a change in the refractive index of the coupled-waveguides [114]. The PN-NP configuration [81] ensures that at any time instance, only one side of the coupled-waveguides experiences a depletion width change, which enables a non-zero coupling between the two supermodes (see Eqs. (2.9) and (2.10)). Figure 5.3(e) shows the overview of the interferomter. The two modulators, one on the left and one on the right, are identical, and only their modulation phases are different (ϕ_R and ϕ_L). The length of both modulators is 3.9 mm, which in simulation (using Eqs. (2.9) and (2.10)) provides and equal probability (50 %) to populate both supermodes. The gap of the coupled-waveguides varies along the interferomter. At the two edges where the modulator is placed, the gap is 900 nm to separate the two supermodes in frequency by a few GHz in the optical c-band as shown in Fig. 5.4(a). This is also the benefit of using coupled waveguides, becuase this frequency separation can also be easily tuned to a range of frequencies that is easy to modualte (i.e. RF frequencies) by simply changing the gap. In the middle of the interferometer, the gap is tapered (the taper length is 100 μm) down to 550 nm and extends for a distance L_f, such that the two supermodes experience different effective indicies Δn_{eff}, and the phase difference between the two supermodes becomes (see Fig. 5.4(b)):

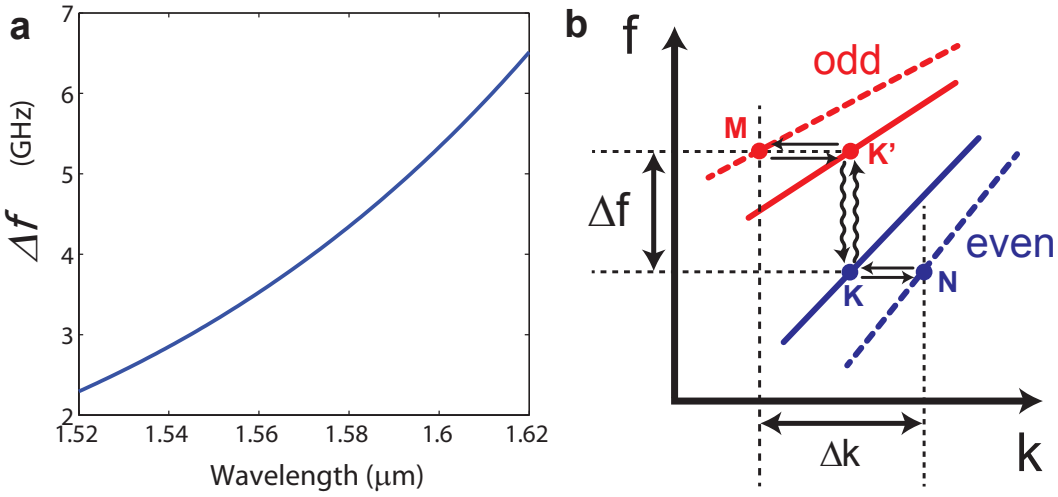

Figure 5.4: The dispersion relation of the even and the odd mode in a silicon coupled-waveguides structure. (a) Simulation of the frequency separation of even- and odd-mode for the waveguide geometry defined in Fig. 5.3(c). (b) A depiction of the dispersion curves for both even (blue) and odd (red) modes at the RF modulation regions (solid) and at the middle modulation-free region (dashed). The modulation frequency f_M ideally should match the frequency separation between the two modes (Δf).

$\Delta\phi_p = \Delta k \times L_f$ ($\Delta k = 2\pi\Delta n_{eff}/\lambda$, and λ is the optical wavelength). In the experiment, L_f varies from 175 to 350 μm for different fabricated devices. We also place multi-mode interference (MMI) devices at each ends of the interferometer so that only even-mode enters and exits the interferometer. A microscope image and a simulated power distribution of the MMI are shown in the insets of Fig. 5.3(e).

5.4 Experimental methods

The photonic Ramsey-type interferomter is fabricated using standard CMOS fabrication technologies. The details of the individual fabrication steps can be

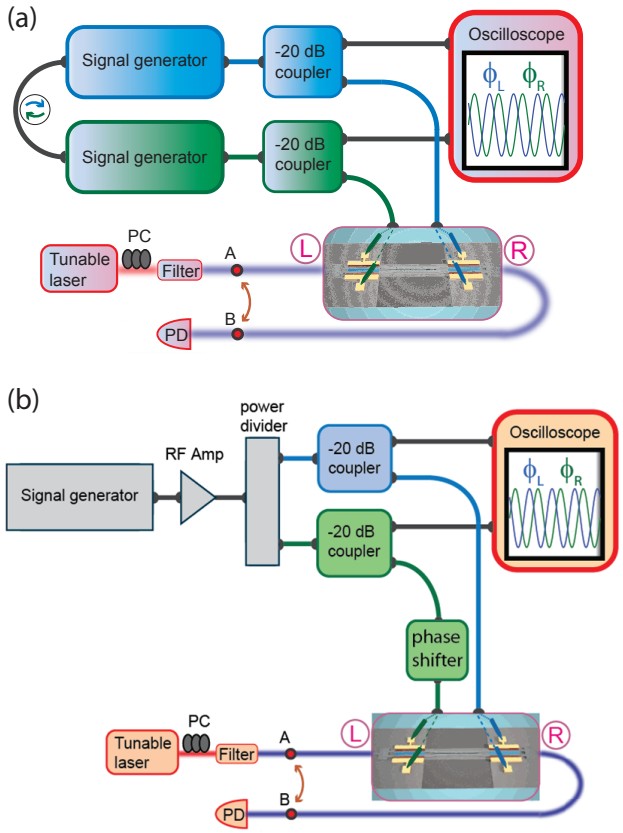

Figure 5.5: Experimental setup that measures the non-reciprocity and the interference fringes for the photonic Ramsey-type interferometers. (a) The two signal generators are synchronized to ensure correlated phase between the two RF signals, and these signals are monitored through the oscilloscope. Fibers connecting to point A and B from the laser and the photodetector (PD) are interchangeable to measure the forward and backward light transmission without moving the setup. (b) Setup configured to obtain higher RF power using an RF amplifier.

found in Chapter 3 (Section 5).

The experimental setup to measure the light transmission through a photonic Ramsey-type interferometer is shown in Fig. 5.5. In Fig. 5.5(a), the two signals applied to each of the modulators are provided by two signal generators with the same sinusoid frequency of 4 GHz to match the frequency separation

of the even- and odd-modes at a wavelength of 1570 nm (see Fig. 5.4(a)). 4 GHz is chosen because both signal generators provide the maximum output at this frequency. Another reason that we chose this f_M is becuase that it cannot violate both the rotating-wave-approximation (RWA) and the condition for harmonic modulation at the same time (see Chapter 2). To be more explicit, f_M has to be much larger than the Rabi oscillation frequency (which is the coupling constant when $f_M = \Delta f$):

$$f_M >> \frac{1}{4\pi}|\kappa| \cdot v_g \tag{5.13}$$

to satisfy the RWA, and:

$$f_M << \frac{4|\kappa|}{\pi}\frac{c}{n_{TLine}} \tag{5.14}$$

to have the RF wavelength much larger than the electrode length. Eq. (5.13) sets a lower frequency to the modulation frequency, which makes sense because the f_M cannot be arbitrary small while still maintaining a strong coupling between the two photonic levels. On the other hand, Eq. (5.14) sets the upper limit for f_M because the modulator needs to be considered as a *lumped* element to provide harmonic modulation (n_{TLine} is the effective index for the electrode transmission line). In our case, the modulator length (l_{mod}) is 3.9 mm, which is given by a $|\kappa| \approx 200$ 1/m. Therefore, based on Eqs. (5.13) and (5.14), a $|\kappa|$ of 200 1/m will lead to $1.1GHz << f_M << 30GHz$. The two signal generators, each set at 24 dBm, are synchronized to ensure a correlated phase, and for both signals, a 1 % of the RF power is dropped through a directional coupler into the oscilloscope. The correlated phases from the two signal generators are then monitored using the oscilloscope. For both signals, the other 99 % of RF power are delivered to their corresponding high speed RF probes that land on the device pads. For the optical setup, we couple light from a tunable laser into the waveguide

through a lensed fiber, and the light transmission through the device is coupled out through another lensed fiber. The output light is then collected by a photodetector. Forward and backward transmissions are measured by interchanging the fiber connectors connecting the laser and the photodetector. To increase the RF power to higher than 24 dBm, the setup shown above is slightly modified as depicted in Fig. 5.5(b). The sinusoidal RF wave from the signal generator is now amplified through an high power RF amplifier. Then, the wave splits into two RF arms and applied to the device through a pair of RF probes. We again drop -20 dB of power from each RF arm to monitor their phases. A phase shifter is added to one RF arm to control the phase difference between the two arms. The optical part of the setup is identical to Fig. 5.5(a). The maximum RF power achieved for each RF arm is about 34 dBm.

5.5 Results and discussions

The photonic Ramsey-type interferometer shows non-reciprocal fringe patterns indicating the existence of an effective magnetic flux from 0 to 2π corresponding to a non-reciprocal 2π phase shift of 8.35 mm (total length of the interferomter) and a fringe extinction ratio of 2.4 dB. Fig. 5.6(a) shows the optical transmission of the fabricated interferometers when light is propagating from left to right (L $\rightarrow$ R) and right to left (R $\rightarrow$ L). The two synchronized sinusoidal RF signals are applied such that ϕ_R and ϕ_L are correlated. We choose λ = 1570 nm to match f_M to the frequency difference between the two supermodes. As shown in Fig. 5.6(a), we see full periods of sinusoidal optical transmissions (fringe patterns) as $B_{flux,eff} = \Delta\phi$ ($= \phi_L - \phi_R$) varies from 0 to 2π. Note that the $B_{flux,eff}$ is defined by the modulation phases as discussed previously. The solid curves in

Fig. 5.6(a) are the theory curve fits (from Eqs. (5.10) and (5.11)), and they all match well the experiments. For all cases of L_f, we observe clear non-reciprocal transmission, where the $\Delta\phi$ that corresponds to the maximum transmission for $R \rightarrow L$ ($\Delta\phi_{R\rightarrow L}$) is different than that of $L \rightarrow R$ ($\Delta\phi_{L\rightarrow R}$). We further show in Fig. 5.6(b) a linear relationship between $|\Delta\phi_{R\rightarrow L} - \Delta\phi_{L\rightarrow R}|$ and L_f. This result is expected because $\Delta\phi_{R\rightarrow L}$ and $\Delta\phi_{L\rightarrow R}$ are both proportional to the phase difference between the two supermodes which is also proportional to L_f. The experiments (circles) match well with the theory (solid) and the data all lie within the theoretical window (gray) that accounts for ±5 % process variation (slab-thickness and gap of the coupled-waveguides). In Fig. 5.6(c), we see that the transmission extinction ratios for light propagating from left to right ($L \rightarrow R$) and right to left ($R \rightarrow L$) with increased coupling between the even- and the odd- modes, achieved by increasing the applied RF power. We show in Fig. 5.6(c) that as the RF powers increases, the extinction ratio for L_f = 325 μm increases from 0.6 dB to 2.4 dB corresponding to population in the odd mode increase from 3 % to 12 %, respectively. From these measurements, the power necessary for achieving maximum extinction (i.e. 50 % population in the odd mode) is estimated to be at least an order of magnitude larger than the theoretical value of 160 mW. This high power requirement in our experiments is due to both the RC cut-off (since the RC bandwidth of our device is around 2.5 GHz, smaller than the modulation frequency of 4 GHz) and the inefficiency of the PN diodes (the PN diodes are estimated to be only about 28 % of the efficiency of the designed value. In principle, redesigning the dispersion of the coupled-waveguides to operate at lower RF frequencies, optimizing the diode profile, and increasing the length of the modulator should further increase the extinction ratio. Note that the non-reciprocal fringes are purely resulted from the effective magnetic flux, and the

direct RF coupling between the two modulators are tested and verified to be less than -30 dB.

In order to confirm that the non-reciprocal fringes are resulted from the interference between the supermodes, the fringes at different wavelengths for L_f=350 μm are measured as shown in Fig. 5.7(a). This wavelength dependence of the fringe extinction ratio is due to the dispersion of the two supermodes - the frequency difference between the supermodes perfectly matches f_M at $\lambda \approx$ 1570 nm and not at other wavelengths. In Fig. 5.7(a), we also observe a slight shift of these fringe phases as λ changes. This is expected since Δn_{eff} for the supermodes are also wavelength dependent. In Fig. 5.7(b) we plot the theoretical (dashed line) and the measured (circles) wavelength dependence of $\Delta\phi_{L\to R}$ and $\Delta\phi_{R\to L}$ from 1560 nm to 1575 nm. One can see that the experiments and the theory agree well.

5.6 Summary

In this chapter, the theory and application of an effective magnetic field is discussed. The effective magnetic field for photons can be directly generated using photonic transitions. An experiment and its results are also shown to verify the existence of such an effect. This effect also creates a non-reciprocal phase for light, which can be implemented in applications such as on-chip isolators that prevent light propagating backwards. So far the presence of an effective magnetic *flux* have been demonstrated, but an effective magnetic *field* have not. The reason for this is that the photonic Ramsey-interferomter is a one-dimensional structure, in which we cannot define an area that this effective magnetic flux

penetrates through (see Eq. (5.8)). In the next chapter, I will discuss how an effective magnetic field for photons can be generated on-chip using basic silicon photonics components such as microring modulators and resonators.

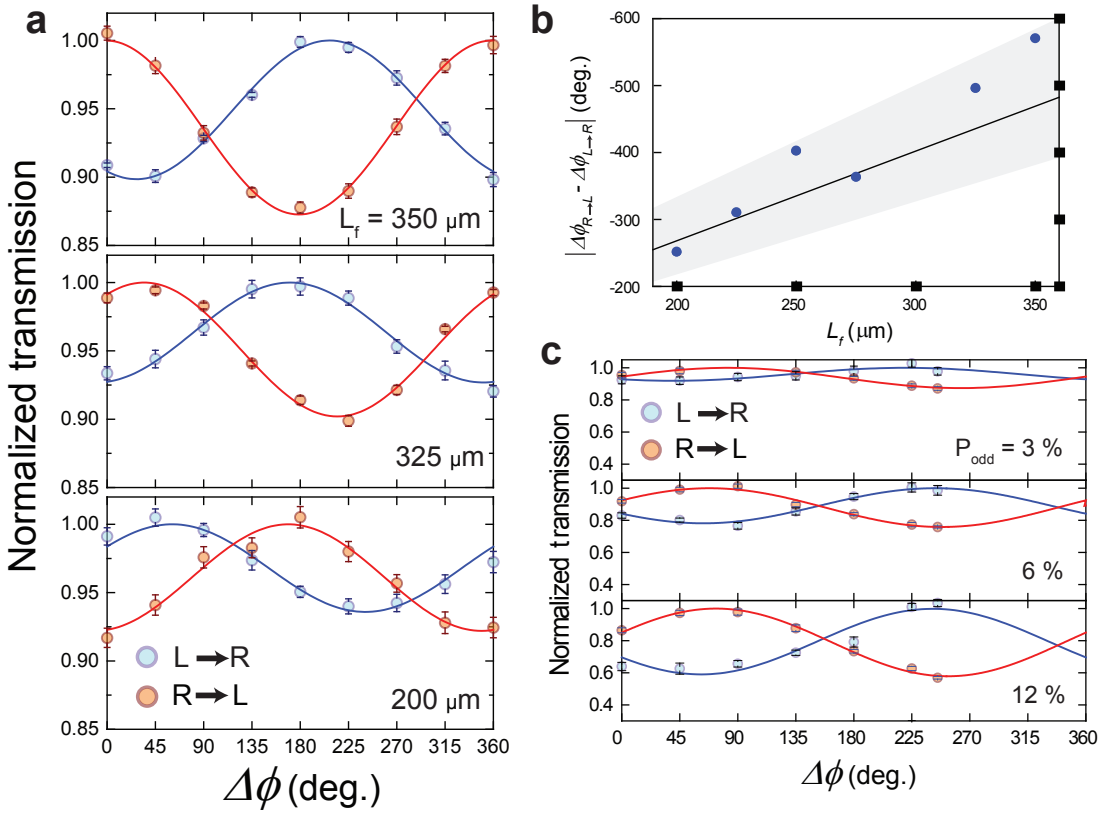

Figure 5.6: (a) Examples of the measured (circles, normalized to the maximum curve fitted value) and theoretically fitted (solid lines) optical transmission for light traveling from left to right (L → R, blue) and right to left ($R \rightarrow L$, red) for devices with different L_f as a function of the phase difference between the two signals applied to the modulators ($\Delta\phi = \phi_L - \phi_R$). The error bar represents one standard deviation from the measurement mean resulting from optical alignment fluctuation. (b) Measured (circles) and theoretical (solid) difference between the $\Delta\phi$ when the transmission is maximum for $L \rightarrow R$ ($\Delta\phi_{L\rightarrow R}$) and $R \rightarrow L$ ($\Delta\phi_{R\rightarrow L}$) versus different L_f values. The gray region indicates the error of the theory curve when a 5 % process variation is introduced. (c) Measured and theoretically fitted optical transmission for light traveling from left to right (blue) and right to left (red) for L_f = 350 μm with increased population in the odd mode Podd (shown as percentages) achieved by increasing the applied RF power.

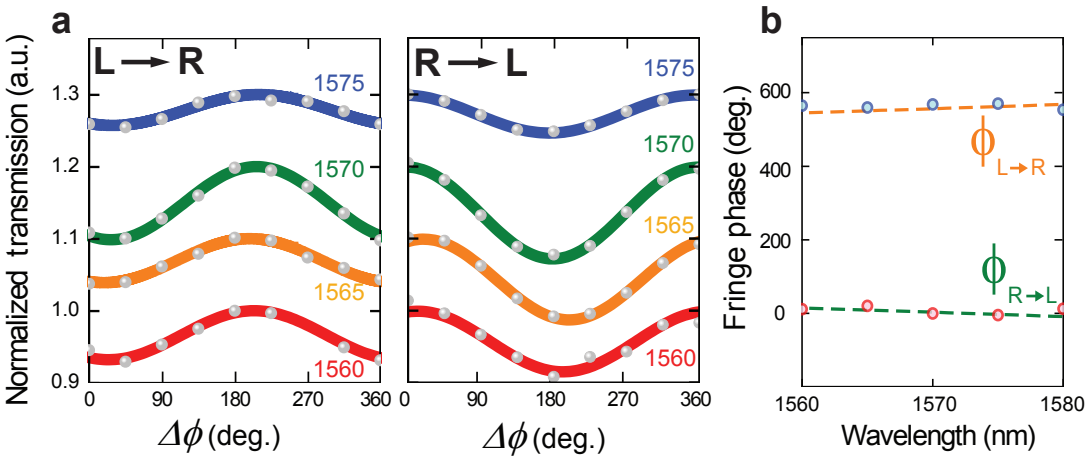

Figure 5.7: Wavelength dependence of the interference effect for the photonic Ramsey-type interferometer. (a) Measured (gray circles, normalized to the maximum curve fitted value) and theoretically fitted (solid) optical transmission of light traveling from left to right and from right to left versus $\Delta\phi$ for different laser wavelengths of 1560, 1565, 1570, and 1575 nm with L_f = 350 μm. (b) Theoretical (dashed line) and measured (circles) phase of the fringes for both $L \rightarrow R$ and $R \rightarrow L$ with varying wavelength.

CHAPTER 6

NON-RECIPROCAL TOPOLOGICAL STATES FOR LIGHT

6.1 Toward realizing topological states induced by an effective magnetic field for light using silicon photonics

Photonic topological insulators have been explored in various contexts and platforms not only to provide new physical insights, but also to remove disorders in large scale integrated photonics implementation. However, topological protection against the most significant limiting factor, namely, the in-plane scattering loss, has not yet been demonstrated. Photonic topological insulators gain a lot of interest [140–143] in the recent years because of its strong analogy with the electron topological states well known as the quantum hall effect (QHE) observed under strong perpendicular magnetic field. One of the signature effect of QHE is the observation of edge states, where electrons can conduct through the edges of a piece of 2D metal sheet, but not through the bulk (hence the name insulator). The edge states are independent of the topology of the piece of metal; For example, like a magnet, the edge states still exist if cutting the metal piece by half or even punching holes along the edge. Another important property of the edge state is that electrons only flow in one direction (counter-clockwise or clockwise depending on the direction of the magnetic field). In principle, if such edge states can be realized for photons, one can prevent the common disorders that often occur on the integrated photonic platform. As shown in Fig. 6.1, these disorders include geometric variations, such as wrong width or shape resulted from fabrication imperfection (Fig. 6.1(a)), and in-plane scattering, which is mainly induced by the roughness on the waveguide edges (Fig. 6.1(b)). Protec-

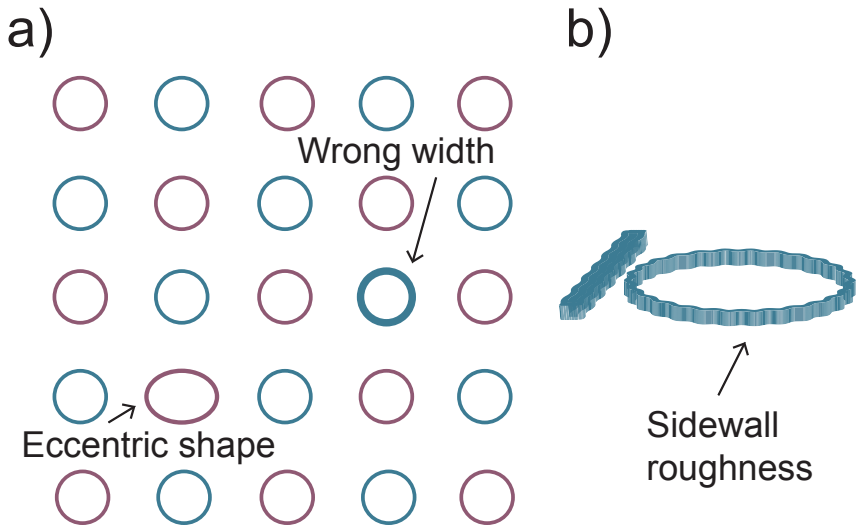

Figure 6.1: (a) Examples of geometric disorders and (b) sidewall roughness induced scattering loss contributed by fabrication imperfections.

tion against these disorders remains a challenge that limits the scalability of on-chip photonic devices. This is especially true for sensitive silicon nanophotonic devices, where the performance of optical delay lines, switches, and routers is almost an order of magnitde less than the fundamental limit because of the in-plane scattering loss [144, 145]. This is also true for low loss silicon ring resonators, such as the one demonstrated with the etchless platform [41], and in slow light devices [144], where backscattering loss is proportional to n_g^2. In addition, in-plane scattering loss is manifested by the coupling between forward and backward propagating light. Therefore, a photonic topological insulator, just like QHE, breaks time-reversal symmetry, and removes the backward propagating channel, thus forcing all the photons to move uniderctionally that in theory mitigates the in-plane scattering loss.

In recent years, there are efforts to replicate the topolical insulators on the optical platform by using an array of coupled silicon microring resonators or

chiral micro-structures [146–151], but these works are all based on passive components which they do not break time-reversal symmetry, and they do not provide full topological protection against backward in-plane scattering loss. The only known ways to break Lorentz reciprocity include nonlinear optics, time-dependent systems, and MO materials. Passive devices do not break time-reversal symmetry. For example, as demonstrated by Hafezi et al. [147], a photonic topological insulator can be realized if the optical phase is dependent instead of on the direction of light, but on the *spinning* direction inside each microresonators, and its direct analogy would be the quantum spin Hall effect (QSHE) rather the QHE, where there exist two edge states, one counterclockwise and one clockise for spin up and spin down electrons. Therefore, it will not protect against non-geometric disorders such as scattering.

Here I will show that a fully protected photonic topological insulator can be achieved by creating an effective magnetic field for light by inducing photonic transitions inside an array of microring resonators. As discussed earlier in Chapter 5, an effetive magnetic field can be generated by interleaving two photonic levels into a two-dimentional lattice (see Fig. 5.1(c)). The local effective magnetic field $\overrightarrow{B_{eff}}(r')$ can then be written as Eq. (5.8), which equals to the total RF phase accumulated for light to travel around the smallest loop enclosing $r = r'$ (we call it a *plaquette*). Therefore, if we want to mimic a electron topological insulator, which is achieved with a *uniform* magnetic field, then $\overrightarrow{B_{eff}}(r')$ also has to be uniform. This means, following Eq. (5.8), the total RF phase accumulated for every plaquette has to be the same. This can be fulfilled by having a specific phase distribution as shown in Fig. 6.2(a), and this phase configuration supports one way edge modes as discussed in detail in Ref. [128].

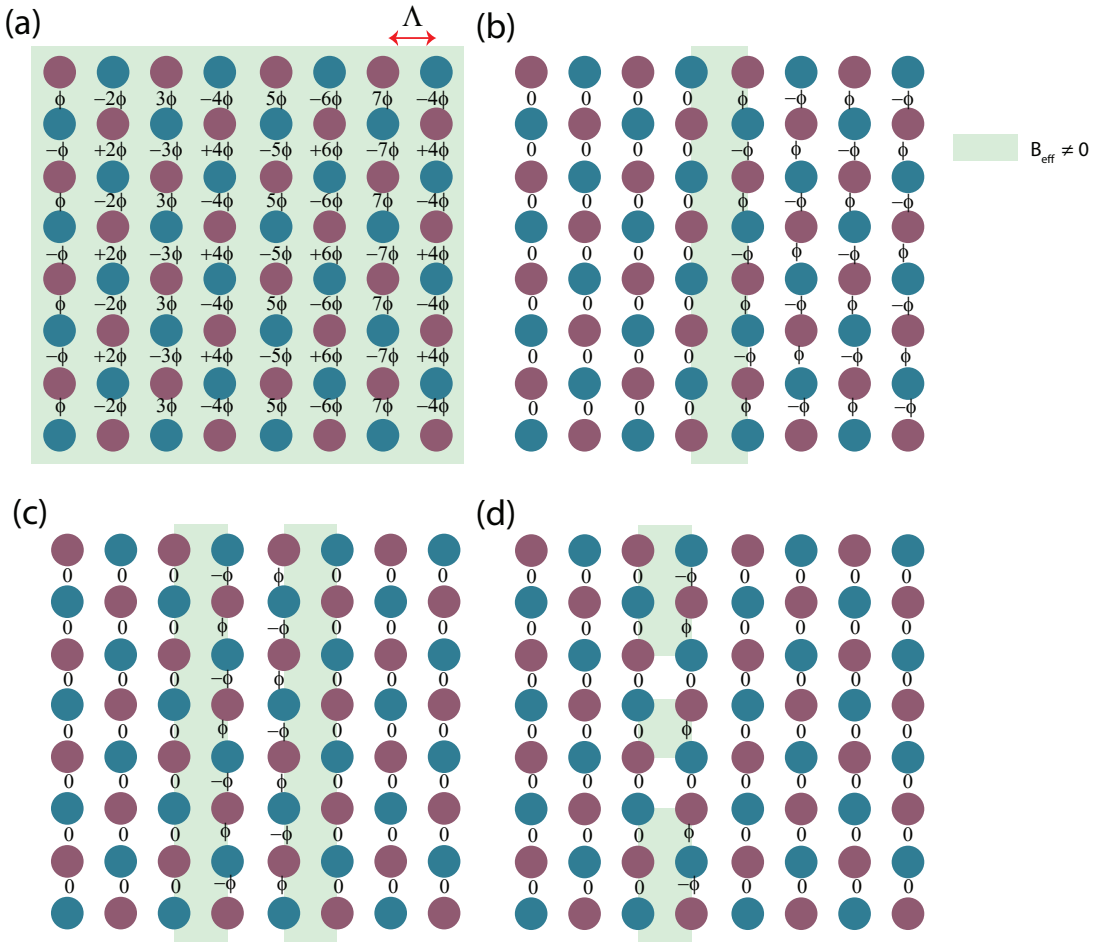

Figure 6.2: Examples of different effective magnetic field distributions (green area) all achieved by simply changing the phases (ϕ) of the RF modulations that are responsible for the photonic transitions between adjacent lattce sites. Each lattice site is represented by one of the two photonic levels (blue: higher energy level, purple: lower energy level).

The effective magnetic field can also be of arbitrary distribution, leading to interesting phenomenon such as light refraction [128] and wave guiding [129]. Since the RF phases of the modulation that induce the photonic transitions can be arbitrarily controlled without changing the pysical dimensions of the device, we can control the flow of light by simply tuning the RF phase. For example, by changing the RF phase distribution to Fig. 6.2(b), one can create a

one-dimensional slit of effective magnetic field, which leads to interesting light refraction at this interface. For certain input angles, the refraction will cause total internal reflection, then by bringing two such one-dimensional slits together, one can construct an effective magnetic field *waveguide* that guides light (see Fig. 6.2(c)), but only in one direction. This platform can also be used to simulate how electrons will interact with an arbitrary real magnetic field distribution. For the most simple example, we can replicate the electron AB effect by making an effective magnetic field *grating* as shown in Fig. 6.2(d), and observe the diffraction pattern on the other side of the grating. Note that In Fig. 6.2, all the green areas have an uniform effective magnetic field of:

$$\overrightarrow{B_{eff}} = \frac{\phi}{\Lambda^2}. \tag{6.1}$$

In the following sections, I will show a practical approach to create a fully protected topological insulator using silicon microresonators and modulators. The design criteria will be subsequently discussed, and an experimental demonstration will also be shown. Finally I will discuss the feasibility and applications for creating such a topological insulator on the silicon photonics platform.

6.2 Photonic transitions between microring resonators

To build a devicce that is protected against both geometric variations and scattering loss by generating an effective magnetic field for light, a single unit cell of a large scale photonic topological insulator has to be demonstrated. Photonic transition is the key mechanism to generate an effective magnetic field, and we have demonstrated this mechanism in Chapter 5. However, the photonic transitions achieved in Chapter 5, in which the photonic transitions (between the

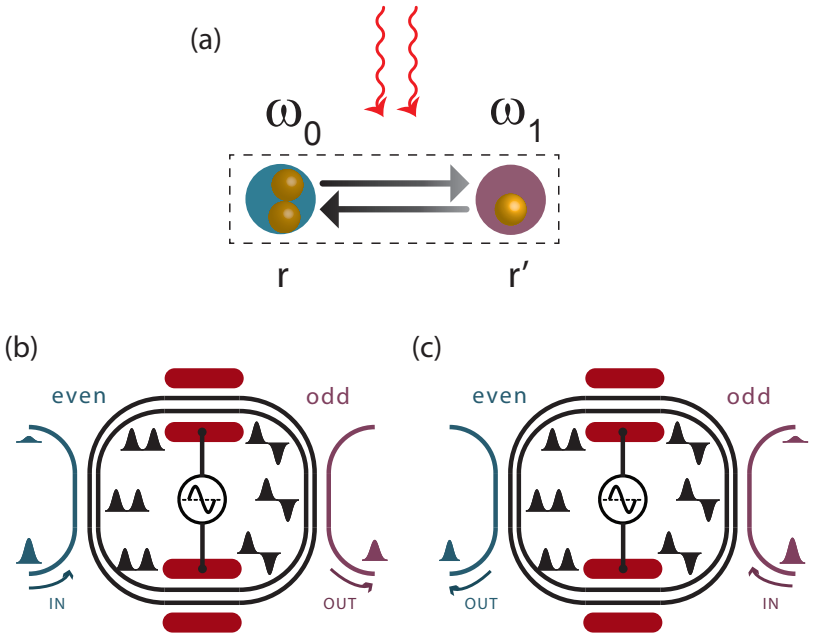

Figure 6.3: (a) Illustration of one unit cell of Fig. 6.2. (b)(c) Coupled-waveguides-resonator: Non-reciprocal phase ring resonator that supports an even and an odd mode. (b) Light is incident on the left bus waveguide, which couples only to the even mode of the coupled-waveguides-resonator. The dynamic modulation in the ring induces coupling from the even mode to the odd mode of the coupled-waveguides-resonator, and the odd mode couples out to the right waveguide and the phase of the modulation is imprinted on the output. Note that the even mode cannot couple to the right waveguide. (c) Similarly, when going from right to left, incident light couples to the antisymmetric mode, and the dynamic modulation couples the odd mode to the even mode, which then couples out to the left waveguide. The opposite phase is imprinted on the output from right to left.

even- and the odd-mode) occur in a straight coupeld-waveguides structure, cannot be easily incorporated into a compact array. In addition, in Chapter 5, the photons in the two photonic levels overlap entirely in space (the same waveguide), and these levels cannot be further interleaved into a lattice form.

Here I show that a unit cell of a large scale photonic topological insulator

can be realized by extending the concept of inducing photonic transitions between the even- and the odd- mode, as discussed in Chapter 5, using micrometer scale coupled-waveguides-resonators. As shown in Fig. 6.3(a), such an unit cell needs to have two spatially separated optical structures, and each structure have to support one photonic level (state). Then, the coupling between the two photonic levels (photonic transitions) has to be enabled *only* by a modulator. Based on these criteria, a possible scheme is illustrated in Figs. 6.3(b) and 6.3(c). In these figures, the blue and the purple waveguide (both single-mode waveguides) will represent the lower and the higher energy photon level, respectively, as they carry photons with different frequencies. The middle (black) ring is formed by a coupled-waveguide (just like the one used in Chapter 5) such that both an even mode and an odd mode are supported, and the photonic transitions between the even and the odd mode occur and enhanced in this coupled-waveguides-resonator (CWR) structure. In Fig. 6.3(b), the light is transmitted from the left to the right based on the following: lower frequency photons input from the blue waveguide will couple to the even mode in the CWR, and a portion (ideally 100 %) of it will be excited to the odd-mode in the CWR and couple out of the CWR into the purple waveguide. Similar story happens when light is going backwards (Fig. 6.3(c)): higher frequency photons input from the purple waveguide will couple to the odd mode in the CWR, and a portion (ideally 100 %) of it will be excited to the even-mode in the CWR and couple out of the CWR into the blue waveguide. To ensure that photons from the blue waveguide will only couple to the even-mode in the CWR, and the photons from the purple waveguide will only couple to the odd-mode in the CWR, the CWR gap is tapered at the coupling regions. The reason for this tapering will be exaplined shortly.

Since active silicon photonic resonators usually have a relatively low quality factor (broad linewidth compared to the modulation frequency (frequency separation between the even and the odd modes)), the coupling regions of the CWR have to be designed such that it can only couple its even mode to the blue waveguide and its odd mode to the purple waveguide. This can be further explained in Fig. 6.4. Instead of the CWR with the waveguide gap tapered at the coupling region (shown in Fig. 6.3 and 6.4(a)), there are in fact two or more designs that are possible to achieve similar effect as illustrated in Fig. 6.4(b) and 6.4(c). For the case in Fig. 6.4(b), since the coupled-waveguides naturally supports even and odd modes separated in frequency, and no special treatment at the coupling region is needed for the CWR. For the other case in Fig. 6.4(c), the CWR can be replaced by a coupled ring-resonator that also supports both an even and an odd mode. Unfortunately, the designs shown in Fig. 6.4(b) and 6.4(c) will introduce a lot of cross-talk between the two modes inside the black (middle) resonator if the Q is low. For example, as shown in Fig. 6.4(d), when the linewidth is broad (low Q), at a given resonance frequency for either the even or the odd mode, there will always be a substantial amount of photons coupled into the other mode. On the other hand, for high-Q system, this cross-talk is substantially reduced. For active silicon devices that often have a linewidth of 10 to 20 GHz, the frequency separation of the two modes has to be at least higher than these linewidths. In order to match the modulation frequency to this separation, the sinusoid modulation efficiency can drop substantially. Therefore, the most robust method is the design shown previously as well as in Fig. 6.4(a), where the coupling to the odd mode (even mode) is prohibited from the blue (purple) waveguide. This is achieved by tapering the gap of the CWR at the coupling-region to create a strong effective index mis-

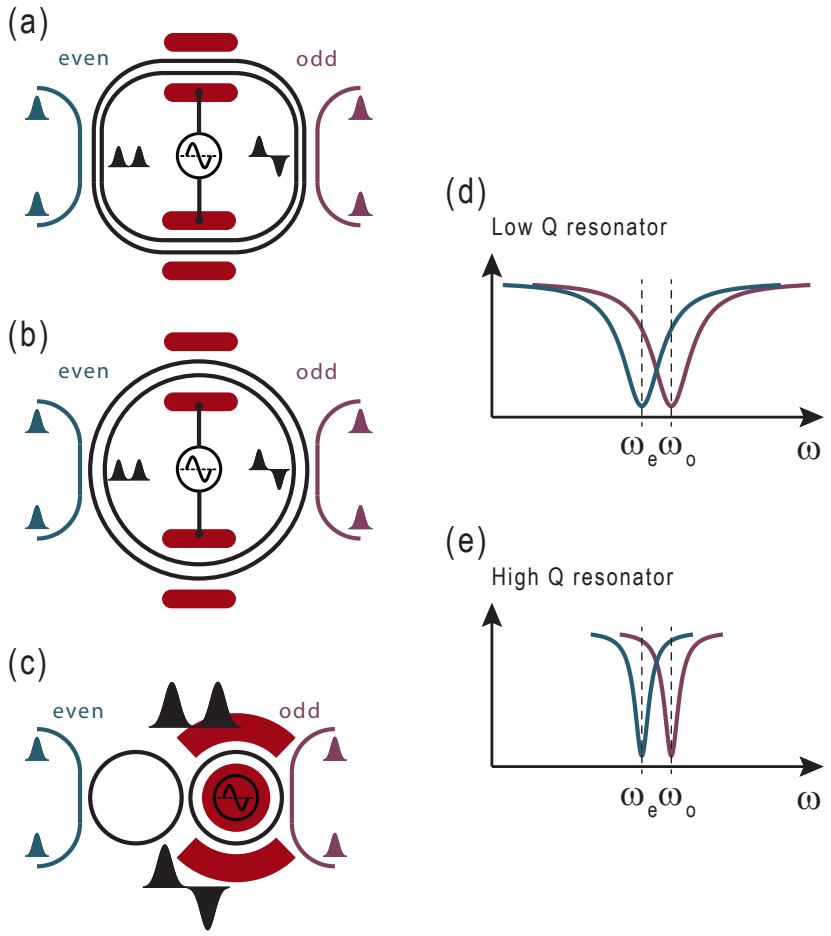

Figure 6.4: (a)-(c) Illustration of different coupled-waveguide-resonator schemes, and examples of (d) broad and (e) narrow linewidth relative to the frequency separation between the two optical modes.

match between the even and the odd modes, and by designing the widths of both the blue and the purple waveguides to match those indices. The details of the design will be revealed in the next section.

Another critical issue with the design is that both the even and the odd mode have to be on resonance in the CWR. This means that the resonance frequency separation between the two modes in the CWR have to match the modulation frequency. This is not the usual case since the even and the odd mode have

different group indices, and therefore different FSRs. The consequence of a different FSR is shown in Fig. 6.5(a). The detuning between the even and the odd modes is possibly deviated from the ideal modulation frequency and it depends on the operating wavelength. This condition is alleviated by the fact that we have a broad resonance linewidth. In addition, the resonance frequency detuning can in fact be designed by the total path length and the length of the coupling region of the CWR. For example, at the coupling region, the effective index of the two modes are greatly different than each other. Therefore, the large index mismatch creates an offset in the k vector between the two modes. Therefore, we can design the length of the coupling region to give us a matched *average* k vector (which is k_{ideal} in Fig. 6.5(b)) such that the two modes are separated at the desired frequency.

Now, the main question is whether this transmitted light carries the nonreciprocal modulation phase similar to the case when photonic transitions occured inside a straight waveguide (as in Chapter 5). The answer is yes, and note that in contrast to the demonstration in Chapter 5, the modulator will be much more compact (about 110 to 200 μm in modulator length comparing to 3,900 μm) and more efficient thereby making the CWR compact to enable large-scale systems. The origin of this result is that light travels inside the resonator for multiple roundtrips and interacts with the modulator multiple times. In addition, by shrinking the size of the modulators, the modulator capacitance is greatly reduced, leading to a higher electrical RC bandwidth.

The light transmitted through the CWR will gain an additional nonrecirpocal phase. To show this result, we can derive both the forward and backward transmission through a CWR using a matrix formula with light am-

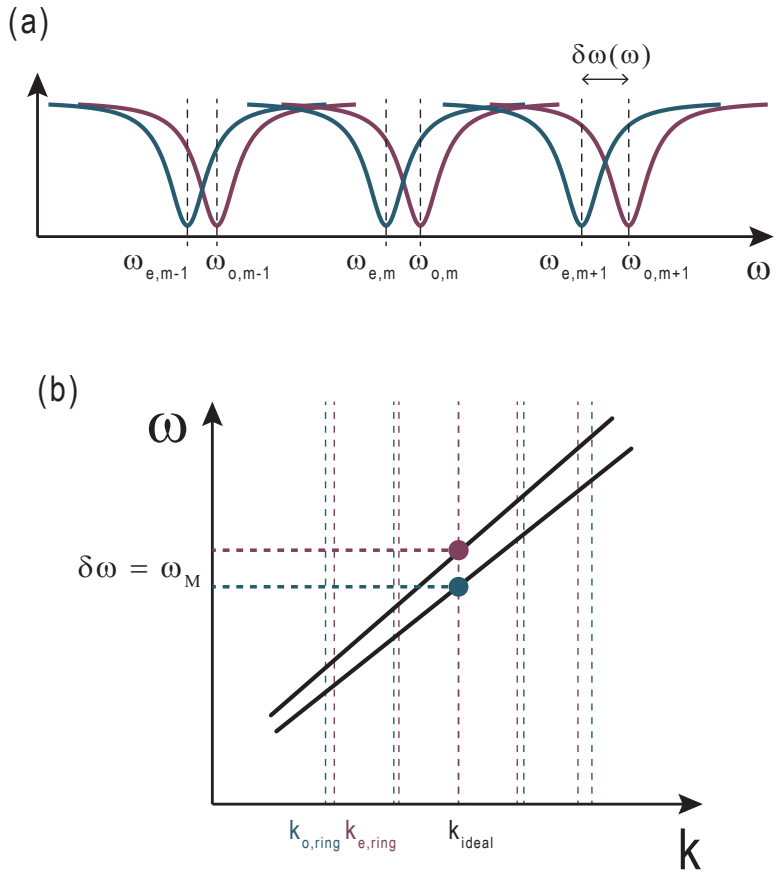

Figure 6.5: (a) Example spectrum of a CWR shown in Fig. 6.3 and 6.4(a). The blue curves correspond to the even mode resonances, and the purple curves correspond to the odd mode resonances. (b) The dispersion curves of the even and the odd modes in the CWR. The dashed lines corresponds to the resonance condition of the modes (blue for the even mode and purple for the odd mode.)

plitudes in the even mode (a_i) and in the odd mode (b_i) defined in Fig. 6.6(a). Using these definitions, we can obtain the following relations:

$$\begin{pmatrix} a_1 \\ a_3 \end{pmatrix} = \begin{pmatrix} t & jr \\ jr & t \end{pmatrix} \cdot \begin{pmatrix} a_0 \\ a_2 \end{pmatrix}, \tag{6.2}$$

$$\begin{pmatrix} b_1 \\ b_3 \end{pmatrix} = \begin{pmatrix} t & jr \\ jr & t \end{pmatrix} \cdot \begin{pmatrix} b_0 \\ b_2 \end{pmatrix}, \tag{6.3}$$

$$\begin{pmatrix} a_4 \\ b_2 \end{pmatrix} = e^{j\delta-\alpha} \begin{pmatrix} \cos(C) & je^{-j\phi}\sin(C) \\ je^{+j\phi}\sin(C) & \cos(C) \end{pmatrix} \cdot \begin{pmatrix} a_3 \\ b_4 \end{pmatrix}, \tag{6.4}$$

and

$$\begin{pmatrix} a_2 \\ b_4 \end{pmatrix} = e^{j\delta-\alpha} \begin{pmatrix} \cos(C) & je^{-j\phi}\sin(C) \\ je^{+j\phi}\sin(C) & \cos(C) \end{pmatrix} \cdot \begin{pmatrix} a_4 \\ b_3 \end{pmatrix}. \tag{6.5}$$

In the above equations, 2δ is the round trip phase (which is assumed to be equal for both the even and odd mode inside the CWR), $e^{-2\alpha}$ is the roundtrip transmission inside the CWR, C is defined as $|\kappa|\times l_{mod}$ (l_{mod} is the length of the modulator), ϕ is the modulation phase, and r is the amplitude coupling at the waveguide-CWR coupling section (where $r^2 + t^2 = 1$). Here we also assumed that δ, α and r for both even and odd modes are of the same values. Solving the above equations with $a_0 = 1$ and $b_0 = 0$ (left to right transmission based on Fig. 6.6(a)), we get:

$$b_1 = -je^{j\phi}\frac{r^2(e^{\alpha-j\delta} + e^{-\alpha+j\delta})\sin(C)}{(1+t)^2\sin^2(C) + (e^{\alpha-j\delta} - e^{-\alpha+j\delta}t)^2}. \tag{6.6}$$

For light transmission in the opposite direction with $a_0 = 0$ and $b_0 = 1$:

$$a_1 = -je^{-j\phi}\frac{r^2(e^{\alpha-j\delta} + e^{-\alpha+j\delta})\sin(C)}{(1+t)^2\sin^2(C) + (e^{\alpha-j\delta} - e^{-\alpha+j\delta}t)^2}. \tag{6.7}$$

By closely examining Eqs. (6.6) and (6.7), we can see the only difference between these two equations is the phase term ϕ, and this phase is opposite sign. This directly confirms that light transmitted through the CWR will acquire a non-reciprocal phase. This shows that the CWR can be potentially used in the unit

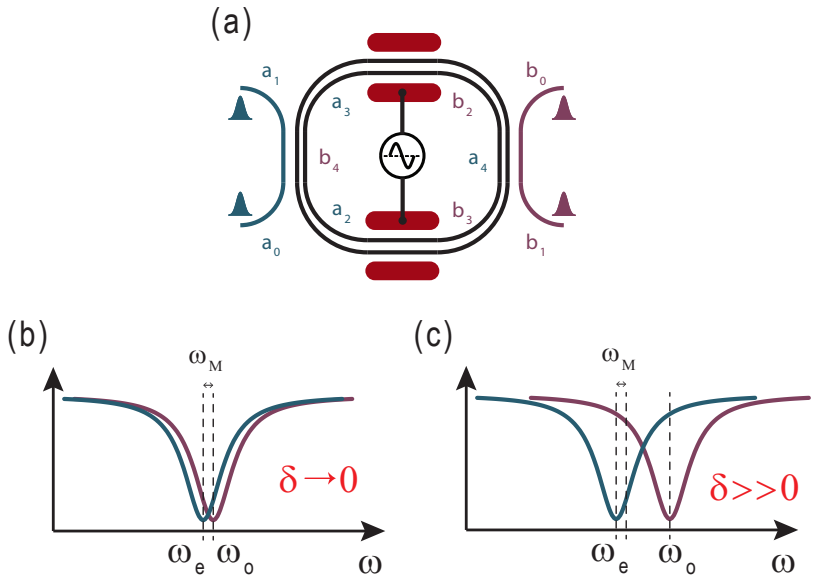

Figure 6.6: (a) Definitions of light amplitudes (a for even mode and b for odd mode) at various part of a CWR resonator unit cell, and example spectra (blue for the even mode and purple for the odd mode) when the resonance frequency detuning between the two modes are (a) negligible and (b) large.

cell (Fig. 6.3) to construct a large-scale resonator array for a photonic topological insulator (Fig. 6.2).

As noted previously, both the even and the odd mode have to be on resonance inside the CWR. Otherwise, as shown in Figs. 6.6(b) and 6.6(c), the photons either converted from the even to the odd or the odd to the even mode will decay very quickly. However, even if they decay quickly, the non-reciprocal phase still exists. This can be shown in a similar set of expressions:

$$b_1 = -ie^{i\phi}\frac{(e^{\alpha-i\delta_1}+e^{-\alpha+i\delta_2})r_1r_2\sin C}{(e^{\alpha-i\delta_1}-e^{-\alpha+i\delta_1}t_1)(e^{\alpha-i\delta_2}-e^{-\alpha+i\delta_2}t_2)+(1+t_1t_2+e^{i(\delta_1-\delta_2)}t_1+e^{-i(\delta_1-\delta_2)}t_2)\sin^2 C} \tag{6.8}$$

For light transmission in the opposite direction with $a_0 = 0$ and $b_0 = 1$:

$$a_1 = -ie^{-i\phi}\frac{(e^{\alpha-i\delta_2} + e^{-\alpha+i\delta_1})r_1 r_2 \sin C}{(e^{\alpha-i\delta_1} - e^{-\alpha+i\delta_1}t_1)(e^{\alpha-i\delta_2} - e^{-\alpha+i\delta_2}t_2) + (1 + t_1t_2 + e^{i(\delta_1-\delta_2)}t_1 + e^{-i(\delta_1-\delta_2)}t_2)\sin^2 C} \tag{6.9}$$

where δ_1 and δ_2 are the detunings of the even and the odd mode from the laser frequency. Equations (6.8) and (6.9) are dervied from a set of matrices similar to Eqs. (6.2)-(6.5), but with separate detunings (for even and the odd mode) included. Note that Eqs. (6.8) and (6.9) can be simplified to Eqs. (6.6) and (6.7) by assuming $\delta_1 = \delta_2 = \delta$. In the next section, I will discuss the design and fabrication of a CWR.

6.3 Design and fabrication

In this section, I will show the design of an unit cell for a photonic topological insulator using an array of coupled-waveguide-resonators. As shown in Fig. 6.7, we can connect all the blue and purple ring resonators by using CWRs to form a 2-dimensional lattice, and each type of resonator is on resonant at a different frequency matching the resonance frequencies of the even and the odd mode inside the CWR. Ultimately, we can apply a different modulation phase on each of the modulators that are incorporated in all the CWRs, and create an arbitrary phase distribution as shown in Fig. 6.2.

There are several critical design rules and requirements that needs to be fulfilled: 1) the asymmetrical coupling, meaning that the even mode in the CWR can only couple to the left (blue) waveguide, and the odd mode in the CWR can only couple to the right (purple) waveguide, 2) the modulation frequency

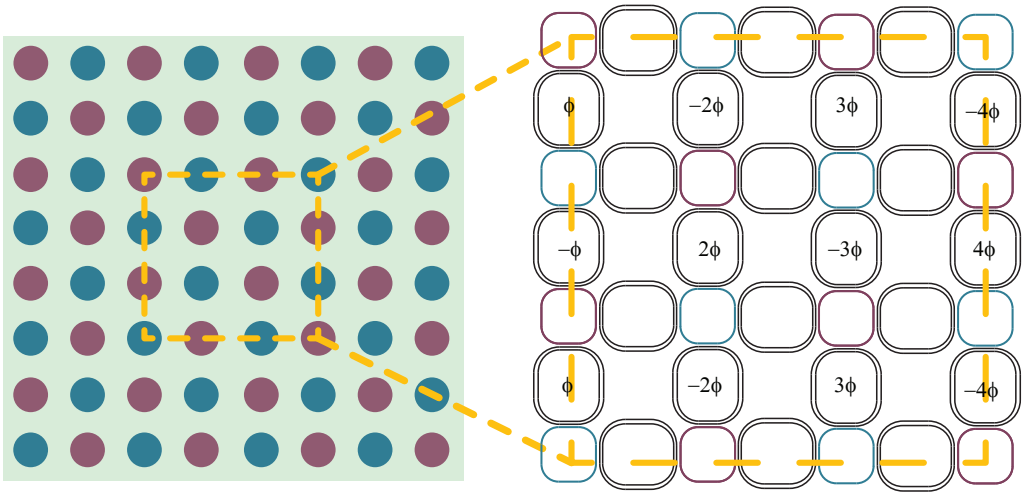

Figure 6.7: The construction of a photonic topological insulator using the proposed coupled-waveguide-resonators shown in Fig. 6.3.

f_M needs to match the frequency separation of the even and the odd mode inside the CWR, 3) coupling (photonic transition rate) to loss ratio inside the CWR has to be maximized, and 4) the resonance frequency of the even and the odd mode inside the CWR has to be matched to the frequency separation between the two modes. For point 1), it is achieved by inducing a strong phase mismatch between the even and the odd modes inside the CWR at the waveguide-CWR coupling regions. To be more specific, in the simulation results shown in Fig. 6.8, as the gap of the coupled-waveguides in the CWR reduces to 150 nm (see Fig. 6.8(b)) (while keeping the waveguide widths constant at 400 nm, height at 250 nm, and slab thickness at 70 nm), the effective index of the even mode $n_{eff,even}$ = 2.53, and $n_{eff,odd}$ = 2.43. Therefore, if we pick the blue waveguide (see Fig. 6.3) to have a width of 430 nm to match the $n_{eff,even}$, and the purple waveguide to have width of 375 nm $n_{eff,odd}$, then the blue waveguide can only couple to the even mode and the purple waveguide can only couple to the odd mode inside the CWR (see Fig 6.8(a)). To address point 2), the gap of the CWR at the

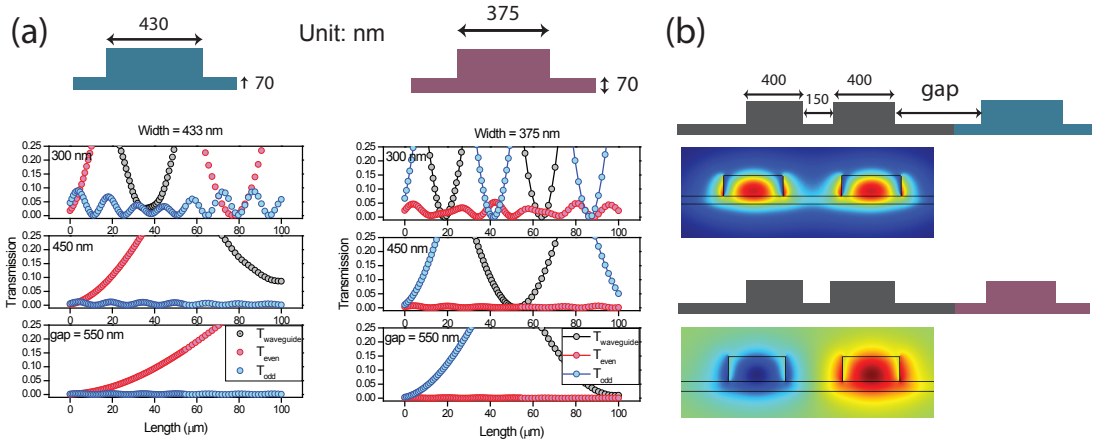

Figure 6.8: (a) The transmission from the blue waveguide into the CWR for different gap widths, and the transmission from the purple waveguide into the CWR for different gap widths. (b) The cross-section of the CWR at the waveguide-CWR coupling region. Here the gap is defined as the distance between the edge of the CWR and the edge of the blue (or purple) waveguide. The mode profile of the even and the odd mode for the CWR are also shown.

modulation regions has to be larger than that at the waveguide-CWR coupling regions (150 nm, as discussed above). To clearly show this, in Fig. 6.9(a), we calculate the frequency difference between the even and the odd modes versus different gap widths for the coupled-waveguides (again, width = 400 nm, height = 250 nm, and slab thickness = 70 nm). From Fig. 6.9(a), we see that the ideal gap is 1250 nm to get a $\Delta f = f_M$ = 4 GHz at the optical wavelength of 1550 nm, which is the same modulation frequency used in Chapter 5. As a result, there is a distinct mismatch of the values of the gaps between the waveguide-CWR coupling region (150 nm) and the modulation region (1250 nm). To bridge this mismatch, as already hinted in Figs. 6.3, the gap in the CWR is adiabatically tapered to the designed gap widths through the resonator bends to prevent both intrinsic coupling (between the even and the odd mode) and radiation (bending) loss. For point 3) the depletion mode silicon modulator is selected, and the

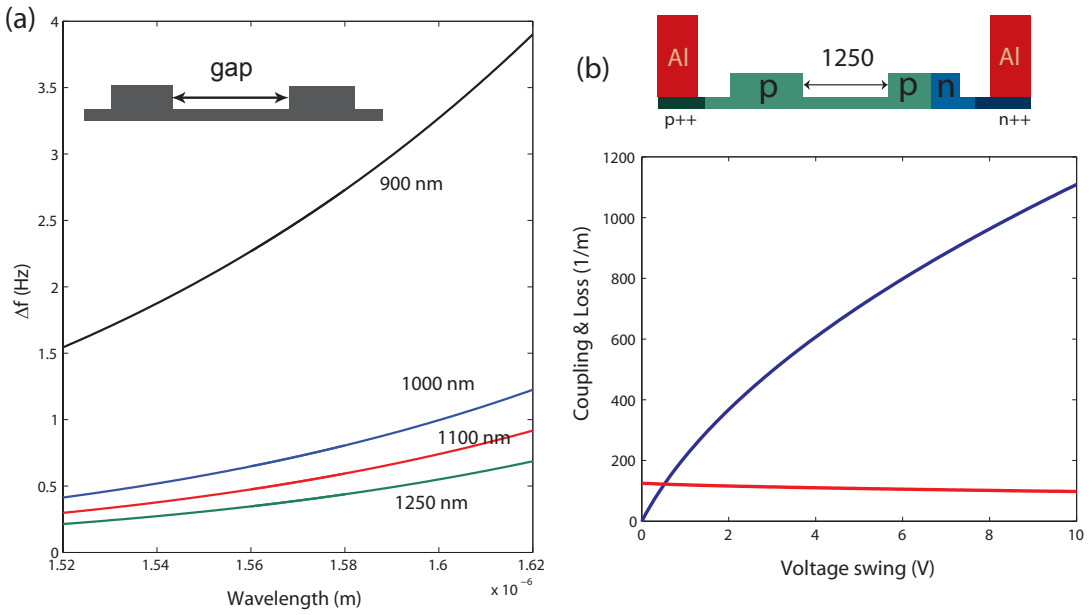

Figure 6.9: (a) The simulated frequency difference between the even and the odd mode in a coupled-waveguide structure. (b) The simulated amplitude coupling and loss (1/m) for the modulation region where the coupled-waveguide is doped into a PN diode and operating with the depletion mode.

cross-sectional doping profile is shown in Fig. 6.9(b). As a reverse biased voltage is applied, the depletion-width of the junction on the right broadens and depletes carriers away from the junction center, resulting in a change of refractive index (as discussed in Chapter 1). For demonstrating the CWR to be used in a large-scale array, on one hand, the optical loss introduced by the doping has to be small, on the other hand, the coupling between the even and the odd modes resulting from the modulation (enabled by the doping) has to be high. To quantify the loss induced by the doping and the coupling between the even and the odd mode in the modulation region, we assume that the modes are uniformly distributed inside the coupled-waveguide (except that the odd mode has a π phase shift in one side of the coupled-waveguide) and the p- and n-doping

are of equal concentration (i.e. P = N). Under this assumption we obtain:

$$|\kappa| \approx \Big|\frac{n\pi}{n_{eff}\lambda W}\Big(- 8.8 \times 10^{-22}\frac{N}{2} - 8.5 \times 10^{-18}\frac{P}{2}\Big)\Big(\frac{4\epsilon_0\epsilon_r}{qN}(V_{bi} - V)\Big)^{0.5}\Big| \tag{6.10}$$

and

$$\alpha_{doping} \approx \Big(- 8.5 \times 10^{-18}N - 6 \times 10^{-18}P\Big)\Bigg(\frac{2W - \Big(\frac{4\epsilon_0\epsilon_r}{qN}(V_{bi} - V)\Big)^{0.5}}{2W}\Bigg), \tag{6.11}$$

where W is the waveguide width, $V_{bi} = 0.7V$ is the built-in potential for silicon, and q is the unit charge. Based on these equations, we can calculate both the amplitude loss and coupling as shown in Fig. 6.9(b). In Fig. 6.9(b), we see that the loss continues to reduce as the applied voltage swing increases, this is due to fact there is an increase in the average depletion width. In addition, the coupling also goes higher as applied voltage swing increases as expected. Therefore, the trend we get from the depletion mode modulator works well in this case: a larger coupling and a smaller loss with increased driving voltage. However, here again we do have to note that the coupling cannot be too strong such that f_M is smaller than the Rabi oscillation frequency (= $v_g \times |\kappa|/2\pi$). Therefore, the non-recirpocal phase might vanish when operating the modulator with high RF powers. Regarding to point 4), the bending radius inside the CWR has to be carefully designed, such that both the even and the odd modes are on resonance. In fact, this criteria is less stringent once the dopants are introduced into the waveguides which broadens the resonance linewidths of the CWR.

6.4 Experimental methods and results

To confirm that minimal intrinsic couplings between the even and the odd mode in the CWR are introduced through the adiabatic tapers (Fig. 6.3), we first mea-

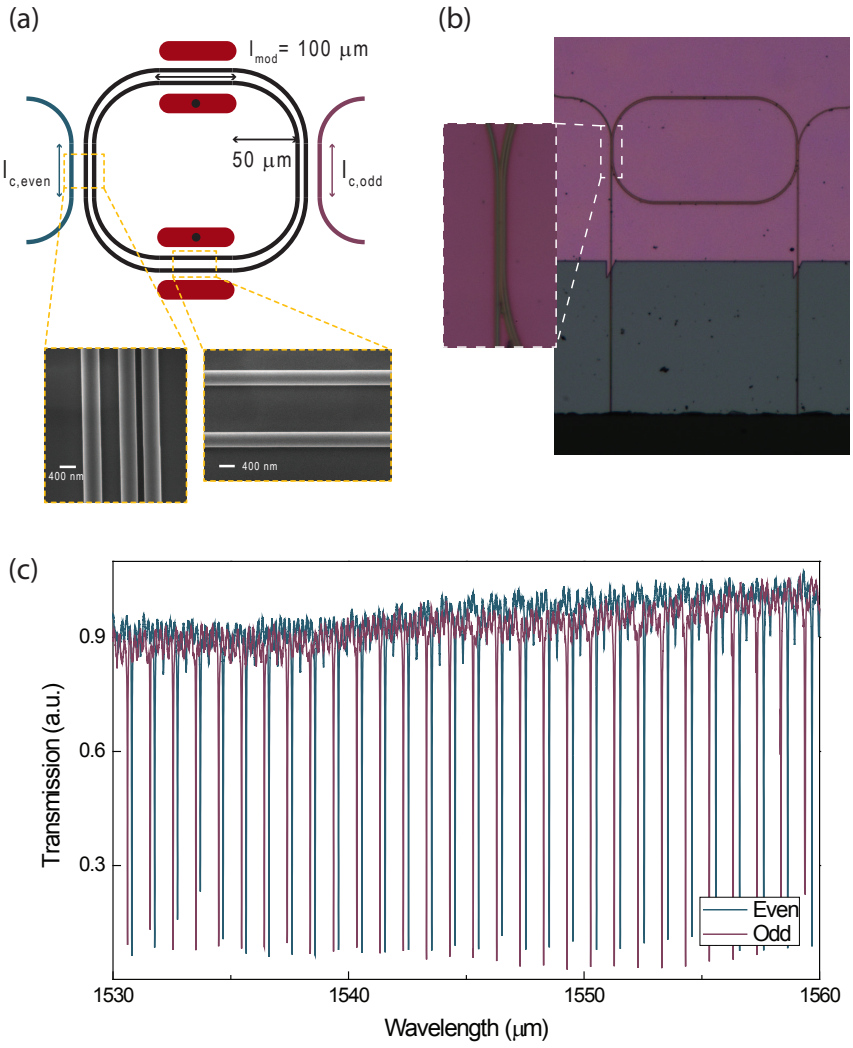

Figure 6.10: (a) The proposed CWR structure and SEM snapshots of the coupling region and the modulation region. (b) Optical microscope image of a CWR without doping and metal connections. The inset shows the coupling region. (c) The transmission spectra of the CWR when coupling through the left (even mode, blue) and the right (odd mode, purple) waveguides.

sure the transmission spectrum of a device that consists of only one CWR and without any active components as shown in Fig. 6.10(c). The fabrication of our devices are standard methods described in Chapter 3. In Fig. 6.10(a), the SEM (scanning electron microscopy) shows that the coupling region have a much

smaller gap then the modulation region of the CWR. Figure 6.10(b) shows the optical microscope image of the fabricated device before introducing the doping and electrodes. In Fig. 6.10(c), we see sharp resonance dips when light is transmitting either through the blue waveguide (on the left) or the purple waveguide (on the right), and the measured loaded quality factor Q_L for both cases are around 65,000. This indicates that the intrinsic loss is dominated by the waveguide in-plane scattering loss, and the intrinsic coupling between the even and the odd mode inside the CWR is negligible. Note that the bending radius of the fabricated CWR is 50 μm. The intrinsic coupling between the two modes might substantially increase if a smaller bending radius is chosen.

The FSR differences between the two modes are very small. This is also shown in the spectra in Fig. 6.10(c), where the frequency detuning of the two modes ($|\delta_1 - \delta_2|$ in Eqs. (6.8) and (6.9)) vary slowly accross wavelength. This result means that the design of the coupling length (l_c, see Fig. 6.10(a)) of the CWR is critical to overlap the resonances of the two optical modes instead of relying on the dispersion of the modes.

After observing sharp resonances for both the even and the odd mode in a passive CWR, an active CWR (with doping and metal included) is fabricated, using the same fabrication methods described in Chapter 3. The optical microscope image of the device is shown in Fig. 6.11(a). In Fig. 6.11(a), we can clearly see the metal pads and electrodes (bright, white). There are four optical input/output ports (orange circle) as defined in Fig. 6.11(a). The waveguide between port 1 and 2 corresponds to the blue waveguide, and the waveguide between port 3 and 4 corresponds to the purple waveguide in Fig. 6.3. If we define port 1 as the input port, then port 2 becomes the through port, and port

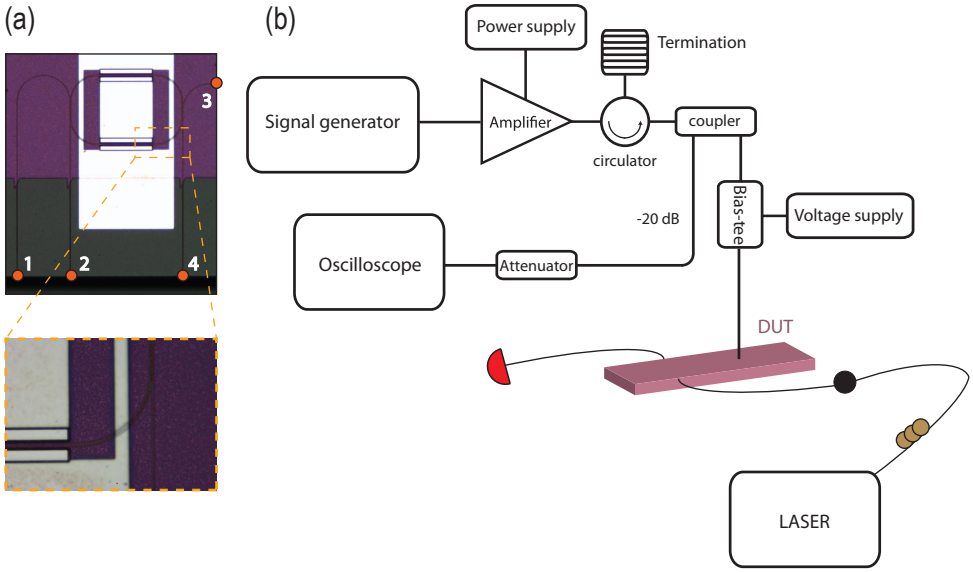

Figure 6.11: (a) Microscope image of an active CWR. (b) The test setup for measuring the transmission of the through and the drop ports of an active CWR.

3 becomes the drop port. Similarly, if we define port 3 as the input port, then port 4 becomes the through port, and port 1 becomes the drop port. Notice that in the following experiment, the transmission from port 1 to port 2 (even mode) through lensed fibers is quite difficult to measure since they are sitting on the same facet. Therefore, the even mode resonances cannot be probed through its transmission spectrum. However, the even mode resonances are present as they are experimentally shown in a passive CWR in Fig. 6.10(c). The modulators have a length of 100 μm for each inside the CWR, and the coupling length (l_c) varies for different devices ranging from 10 to 35 μm. The bending radius of the CWR is fixed at 50 μm, which is the same as the passive CWRs shown in Figs. 6.10(a) and 6.10(b).

The test setup is shown in Fig. 6.11(b). A signal generator goes through an RF amplifier (optional, only necessary if RF power is higher than 24 dBm), and

1 % of the RF power is dropped to monitor in the oscilloscope. The rest of the RF wave goes through a bias-tee, which adds a DC bias to the signal, and goes into a high speed RF probe that touches the metal pads on the chip. For the optical path, light emitted from a continuous-wave c-band laser is sent through an optical fiber that goes through polarization controllers and couples into the waveguide at the chip facet using an polarization maintained (PM) lensed fiber. The output light from the waveguide is emitted from the facet on the other end of the chip, then it is collected with another PM lensed fiber that connects to a photodetector to read out the optical power. The RF frequency from the signal generator is 4 GHz, this is to match the frequency spacing of the two modes (see Fig. 6.9). The DC biased applied through the bias-tee is set at -3 V to avoid operating into the forward bias regime that would add additional loss to the CWR. The optical input power from the lensed fiber is about 1 dBm. A circulator is added after the RF amplifier to avoid strong reflections from our devices that would hamper the performance of the amplifier, since we know that the device will not be strictly impedance matched to the impedance of our testing environment (50 Ω).

Cavity resonances for the avtive CWR are observed in the through port transmission spectrum. As shown in Fig. 6.12(a), clear periodic resonance dips are measured for the transmission from port 3 to port 4 (defined in Fig. 6.11(a)). These dips correspond to the resonances for the odd mode of the CWR. The FSR of the odd mode is about 1 nm, and the Q of the odd mode is about 6,000. Notice that there are no direct measurement of the even mode. However, both the FSR and the Q should be very similar to the odd mode as shown in the transmission spectra of the passive CWR (see Fig. 6.10(c)).

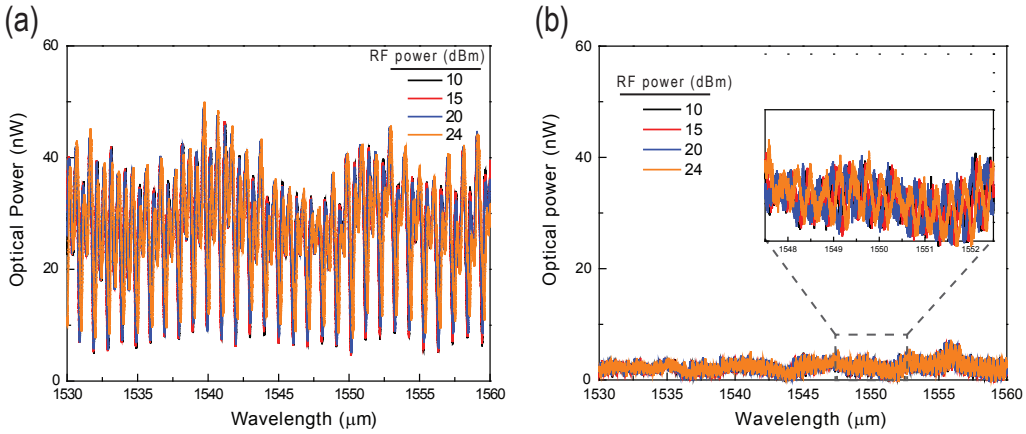

Figure 6.12: The optical power transmitted through the CWR (a) through and (b) drop ports.

No significant change to the spectra is observed when RF power is applied because of the high loss measured in the CWR. In the ideal case, an obvious change of amplitude in the odd mode transmission dip is expected, because the coupling between the odd mode to the even mode will result in extra losses for the odd mode. However, as shown in Fig. 6.12(a), the amplitude of the dips did not change much, and the slight shift in the resonance position is a result of excess heat induced in by the high RF power. On the other hand, a significant increase in the drop port power (transmission from port 3 to port 1) is expected because a portion of the input (odd mode) photon is now converted to even mode photons and then coupled out to the other side of the CWR. Nevertheless, as shown in Fig. 6.12(b) and its inset, as the RF power increases from 10 to 24 dBm, this experiment show no signs of such a mode conversion in the CWR. The reason why the mode conversion is so weak is that the resonator loss is much higher (loss coefficient calculated to be 1,600 1/m) than expected (loss coefficient a few hundreds of 1/m, see Fig. 6.9(b)), and large amount of stray light obscures the minute signal coming out of the drop port.

The photonic transition in the CWR is observed using a beat note experiment. Because the photonic transition in the CWR is very weak, a beat note experiment is implemented, and the experimental setup is illustrated in Fig. 6.13. The setup is very similar to Fig. 6.11(b). The differences between these two setups are all in the optical paths. In Fig. 6.13, before input light from the laser arrives at the chip, 1 % of light is splitted apart from the main light path. This light path is now called the reference arm. The output light from the chip is then combined with the reference arm (which goes through a variable optical attenuator (VOA) to balance the power in the two arms) are then recombined in another 50/50 coupler. Then the detector reads out the power of light from one of the 50/50 coupler output ports that is amplified in a c-band EDFA (erbium-doped fiber amplifier). The idea of this measurement is explained as follows: since the majority of the photons transmitted through the CWR into the drop port should be higher (transmission from port 1 to port 3) or lower (transmission from port 3 to port 1) in frequency of f_M from the frequency of the input photons, after the output is recombined with the reference arm, light should exhibit a slowly varying envelope with frequency f_M. This envelope is then converted into the electrical domain through a photodetector, and the amplitude of this envelope is measured in the spectrum analyzer. Because the spectrum analyzer can have a very low noise level when a very small filter bandwidth is used, a very small amount of photonic transitions can be easily observed.

The photonic transitions exist in the CWR. This is shown in the experimental results for CWRs with three different coupling lengths ($l_c = l_{c,even} = l_{c,odd}$) in Fig. 6.14. For the case when l_c is 11 μm (Figure 6.14(a)), the RF power of the drop port beat notes (blue and yellow circles) show periodic peaks across the entire measured wavelength range (this range is limited by the EDFA gain spectrum). Note

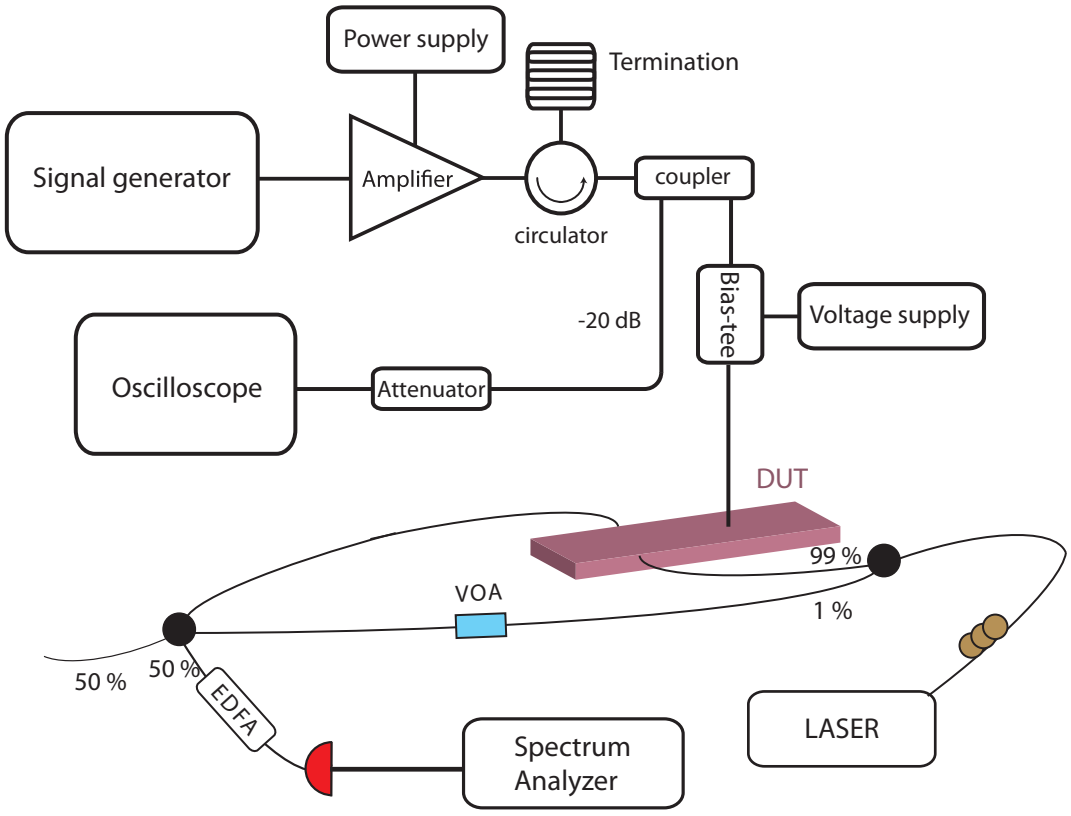

Figure 6.13: The experimental setup for the beat note measurement of a single CWR resonator.

that the blue (yellow) circles corresponds to the drop port beat note measured for light input from port 3 (1) and exit from port 1 (3). These peaks matches the resonance positions of each of the odd resonance modes in the measured through port spectrum (black circles) in the CWR as shown by the red dotted lines. The period of the peaks is also very close to the FSR of the odd-mode resonances. In addition, the RF power of the peaks are very similar for both cases, which validates the theory represented by Eqs.(6.8) and (6.9). These observations are strong indications that these peaks are resulted from the optical beating between the photonic-transitioned light and the light in the reference arm. Because the coupling is still relatively weak when compared to the loss

inside the CWR (under-coupled), the resonance dips in the through port transmission spectrum are far away from 0 optical power. To estimate the amount of photons that experienced this photonic transition in the CWR, the drop port optical power is calculated based on the EDFA gain and the detector efficiency. The results (only converted optical and RF power to transmission over a wavelength span of three FSRs) are shown in the right hand side of Fig. 6.14(a), and the theory curves based on Eqs. (6.8) and (6.9) (fitting parameter: detuning = $\pi/15$, t_{even} = 0.96, t_{odd} = 0.98) are overlayed on the converted data. From these results, the drop port transmission is indeed very small at about 0.5 %. This matches the observation in Fig. 6.12(b) that no obvious change is observed when directly looking at the drop port optical power as RF power is increased. As shown in Fig. 6.14(b), as l_c increases to 22 μm, the resonance dips indeed become more prominent (the coupling strength is now much stronger and approaches the critical coupling condition). However, the drop port RF beat notes becomes slightly weaker than the case in Fig. 6.14(a). In addition, noticeable red-shift for peaks in the drop port RF beat notes from the odd-mode resonances are observed. This can be explained by the fact that the even and the odd mode are spectrally misaligned, and the peaks are more spectrally aligned with the even-mode resonances due to its stronger coupling with the bus-waveguide. To prove this point, as shown in the right hand side of Fig. 6.14(b), we see good agreements between the theory (fitting parameter: detuning = $\pi/4$, t_{even} = 0.65, t_{odd} = 0.94) and the experiments, and the transmission into the drop port is now slightly lower at around 0.2 to 0.3 %. As the l_c is further increased to 33 μm, although obvious odd mode resonances are observed, the RF beat notes in the drop port is buried in the noise of the spectrum analyzer. The is resulted from the fact that the resonance detuning between the even and the odd modes is

even larger than in Fig. 6.14(b). This is again proved in the theory curves (fitting parameters: detuning = $2\pi/5$, $t_{even} = 0.58$, $t_{odd} = 0.87$) shown in the right hand side of Fig. 6.14(c). Notice that the global parameters for the theory curves in all three cases in Fig. 6.14 are the resonator optical loss (round-trip-loss (RTL) = 65 %) and the mode coupling strength ($|\kappa| \times l_{mod} = \pi/85$) for the modulator.

The projected transmission through the CWR is 30 % if the loss can be reduced. In Fig. 6.14, the transmission through the CWR is relatively small (0.5 %) because the loss is high (for all cases in Fig. 6.14) and the detuning between the even and the odd mode is significant (for the cases in Fig. 6.14(b) and 6.14(c)). The detuning between the even and the odd mode is determined by the geometry of the CWR, whereas the measured loss of the CWR (RTL = 65 % corresponds to a loss coefficient $\alpha \approx 1{,}800$ 1/m) is much greater than the expected value (≈ 100 1/m as shown in Fig. 6.9(b)). This is because the waveguide loss dominates the overall loss, which is again unexpected based on the high Q resonances dips observed in the passive CWRs (Fig. 6.10(c)). Therefore, it is reasonable to predict that the overall loss of the CWR can be much improved to about 300 1/m (adding a 4 dB/cm loss from the fabrication waveguide), which corresponds to an RTL of about 16 %. In Fig. 6.15, the transmissions of the CWR versus both different mode coupling strength ($C = |\kappa| \times l_{mod}$) and coupling to the waveguides (assumed to be equal for both the even and the odd modes as $\sqrt{1 - t^2}$) are calculated based on different RTL. The red dot and dashed lines in each figure represent the fitting parameter ($t = 0.95$ and $C = \pi/85$) in Fig. 6.14(a) (the case with minimal detuning between the two modes). The corresponding transmission spectra for both the thru and the drop port are also shown in the figures. As shown in Fig. 6.15(a), when the loss is high (which is the case for Fig. 6.15(a)), the transmission is very small at around 0.5 % as expected. As

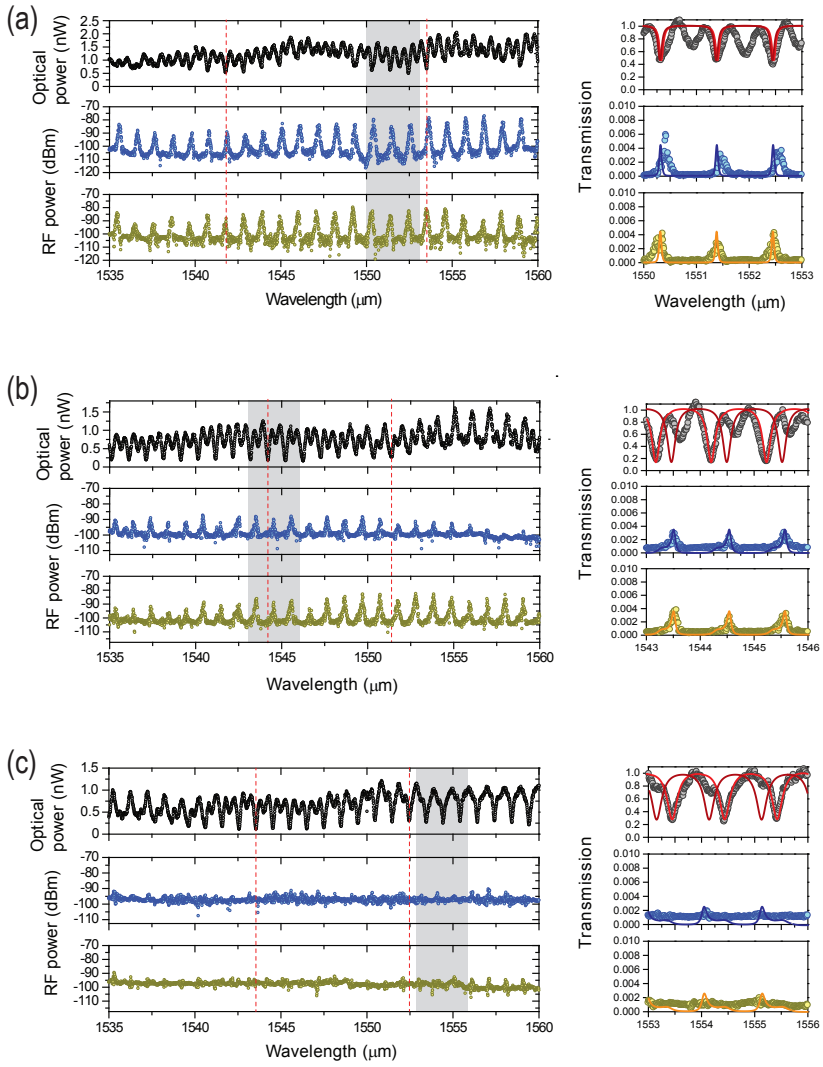

Figure 6.14: The measured transmission spectra of the through port (black, transmission from port 3 to port 4), the drop port beat note (blue, transmission from port 3 to port 1), and the drop port beat note when chip input is reversed (yellow, transmission from port 1 to port 3) for l_c = (a) 11 μm, (b) 22 μm, and 33 μm. The right hand side of the figures show the estimated transmission and theoretical curve fits (solid).

the RTL in the CWR is reduced to 32 %, the drop port transmission becomes 10 %. When RTL is 16 %, the drop port transmission improves to 30 %. Note that the mode coupling coefficient for $C = \pi/85$ corresponds to a photonic transition

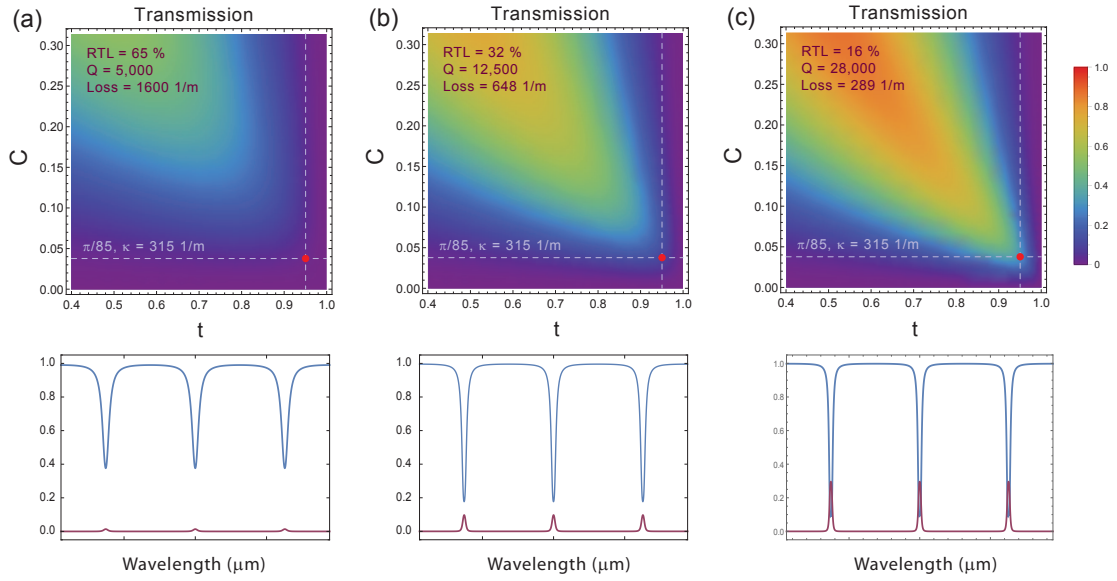

Figure 6.15: Theoretical calculation of the drop port transmission with different waveguide coupling strength ($\sqrt{1-t^2}$) and mode coupling strength ($C = |\kappa| \times l_{mod}$) of a CWR for RTL = (a) 65 %, (b) 32 %, and (c) 16 %. The red dot corresponds to the case for the CWR in Fig. 6.14(a) with negligible detuning between the resonance wavelengths of the even and the odd mode. The bottom figures are the simulated transmission in the through (blue) and the drop (purple) ports for the condition set at the red dots.

rate of 2.2 GHz, which is already close to twice of the modulation frequency at 8 GHz (see Chapter 2). Therefore, continue increasing the RF power will break the rotating-wave approximation (strong coupling regime), and the non-reciprocal phases will be obscured by the intereference from the higher order oscillations.

6.5 Summary

In this chapter, I show photonic transition in a coupled-waveguide-resonator that simultaneously carries two optical modes. These two modes couple inside

and transmit through the drop port of the CWR. This demonstration is one step closer toward realizing an effective magnetic field for light.

CHAPTER 7

SUMMARY AND FUTURE WORK

I have shown in this dissertation, how to generate photonic transitions on the silicon photonics platform using electrically driven refractive index modulation. This is much more flexible than optically driven photonic transitions [86] because the modulation distribution can be easily controlled. The photonic transitions are also very rarely exploited in nanophotonics. Interesting and rich physics that draw analogy with atom physics are waiting to be explored (for example, a photonic three level system can be considered, which will potentially show interesting physical phenomenon such as the electromagnetically-induced-transparency [152–154]).

The fundamental limitation of using silicon to modulate the refractive index is that considerable loss is always associated. Therefore, other materials that do not introduce excessive loss when modulation is applied (Pockel's effect such as $LiNbO_3$) can potentially be used in large scale photonic transition arrays described in Chapter 6. Another interesting way to modulate light in a waveguide is to use opto-mechanical strcutures [155]. Opto-mechanical modulation is achieved by deforming the waveguide through mechanical vibrations, which is equivalent to a hybrid photon-phonon mode. This type of modulation is also loss-free and the optical resonators can simultaneously possess high Q and high mechanical frequency [156].

The FSRC modulators are inherently large because the FSR has to match the operating frequency. However, slow light waveguides [157] can further reduce the size of the microring to reduce power consumption and device footprint. In addition, the phases of each of the modulator segments can be arbitrarily tuned

to control the coupling coefficients between the neighboring FSR modes.

The non-reciprocal phases induced by an effective magnetic flux for light can be further improved by balancing the power in the two modes between the two modulator. Since the mode effective index of the two optical modes between the two modulators are different, some of the light in the even mode can be tapped out to balance the optical power between the two modes. This will significantly increase the visibility of the non-reciprocal fringes (the isolation extinction ratio) without increasing the modulator power, but at the expense of higher optical insertion loss.

Realizing a two-dimensional array of photonic transition elements (such as the one demonstrated in Chapter 6) is the next step to demonstrate fully-protected photonic topological insulators [128], effective magnetic field waveguides [129], and interesting beam steering effect [158]. The main obstacles keeping these effects to be realized are the inhomogenious microresonator fabrication, the photonic transition efficiency through one resonator, and the electrical wiring of the two-dimensional modulator array.

BIBLIOGRAPHY

[1] B. Jalali and S. Fathpour. Silicon Photonics. *Journal of Lightwave Technology*, 24(12):4600–4615, December 2006.

[2] Michal Lipson. Guiding, Modulating, and Emitting Light on Silicon-Challenges and Opportunities. *Journal of Lightwave Technology*, 23(12):4222, December 2005.

[3] Richard Soref. Silicon photonics technology: past, present, and future. volume 5730, pages 19–28, 2005.

[4] D.J. Paul. Silicon photonics: a bright future? *Electronics Letters*, 45(12):582, 2009.

[5] Michael Hochberg and Tom Baehr-Jones. Towards fabless silicon photonics. *Nature Photonics*, 4(8):492–494, August 2010.

[6] Tom Baehr-Jones, Thierry Pinguet, Patrick Lo Guo-Qiang, Steven Danziger, Dennis Prather, and Michael Hochberg. Myths and rumours of silicon photonics. *Nature Photonics*, 6(4):206–208, April 2012.

[7] Radhakrishnan Nagarajan, Masaki Kato, Jacco Pleumeekers, Peter Evans, Damien Lambert, Arnold Chen, Vince Dominic, Atul Mathur, Prashant Chavarkar, Mark Missey, Andrew Dentai, Sheila Hurtt, Johan Bck, Ranjani Muthiah, Sanjeev Murthy, Randal Salvatore, Charles Joyner, Jon Rossi, Richard Schneider, Mehrdad Ziari, Huan-Shang Tsai, Jeffrey Bostak, Michael Kauffman, Stephen Pennypacker, Timothy Butrie, Michael Reffle, Dave Mehuys, Matthew Mitchell, Alan Nilsson, Stephen Grubb, Fred Kish, and David Welch. Large-scale photonic integrated circuits for long-haul transmission and switching. *Journal of Optical Networking*, 6(2):102, 2007.

[8] P.J. Winzer, A.H. Gnauck, C.R. Doerr, M. Magarini, and L.L. Buhl. Spectrally efficient long-haul optical networking using 112-Gb/s polarization-multiplexed 16-qam. *Journal of Lightwave Technology*, 28(4):547–556, February 2010.

[9] J.U. Knickerbocker, G.S. Patel, P.S. Andry, C.K. Tsang, L.P. Buchwalter, E. Sprogis, Hua Gan, R.R. Horton, R. Polastre, S.L. Wright, C. Schuster, C. Baks, F. Doany, J. Rosner, and S. Cordes. Three dimensional silicon

integration using fine pitch interconnection, silicon processing and silicon carrier packaging technology. In *Custom Integrated Circuits Conference, 2005. Proceedings of the IEEE 2005*, pages 659–662, September 2005.

[10] B. Analui, D. Guckenberger, D. Kucharski, and A. Narasimha. A fully integrated 20-gb/s optoelectronic transceiver implemented in a standard 0.13- cmos soi technology. *IEEE Journal of Solid-State Circuits*, 41(12):2945–2955, December 2006.

[11] A. Narasimha, B. Analui, Yi Liang, T.J. Sleboda, S. Abdalla, E. Balmater, S. Gloeckner, D. Guckenberger, M. Harrison, R.G.M.P. Koumans, D. Kucharski, A. Mekis, S. Mirsaidi, Dan Song, and T. Pinguet. A Fully Integrated 4 times; 10-Gb/s DWDM Optoelectronic Transceiver Implemented in a Standard 0.13 #956;m CMOS SOI Technology. *IEEE Journal of Solid-State Circuits*, 42(12):2736–2744, December 2007.

[12] Mehdi Asghari and Ashok V. Krishnamoorthy. Silicon photonics: Energy-efficient communication. *Nature Photonics*, 5(5):268–270, May 2011.

[13] Xuezhe Zheng, Frankie Liu, Jon Lexau, Dinesh Patil, Guoliang Li, Ying Luo, Hiren Thacker, Ivan Shubin, Jin Yao, Kannan Raj, Ron Ho, John E. Cunningham, and Ashok Krishnamoorthy. Ultra-low power arrayed cmos silicon photonic transceivers for an 80 gbps wdm optical link. page PDPA1. OSA, 2011.

[14] A.J. Seeds. Microwave photonics. *IEEE Transactions on Microwave Theory and Techniques*, 50(3):877–887, March 2002.

[15] Jos Capmany, Beatriz Ortega, and Daniel Pastor. A tutorial on microwave photonic filters. *Journal of Lightwave Technology*, 24(1):201, January 2006.

[16] Jos Capmany and Dalma Novak. Microwave photonics combines two worlds. *Nature Photonics*, 1(6):319–330, June 2007.

[17] D. Guckenberger. Microwave photonic applications for silicon photonics. In *Conference on Optical Fiber Communication - incudes post deadline papers, 2009. OFC 2009*, pages 1–3, March 2009.

[18] Jianping Yao. Microwave photonics. *Journal of Lightwave Technology*, 27(3):314–335, February 2009.

[19] Maroof H. Khan, Hao Shen, Yi Xuan, Lin Zhao, Shijun Xiao, Daniel E.

Leaird, Andrew M. Weiner, and Minghao Qi. Ultrabroad-bandwidth arbitrary radiofrequency waveform generation with a silicon photonic chip-based spectral shaper. *Nature Photonics*, 4(2):117–122, February 2010.

[20] Jos Capmany, Guifang Li, Christina Lim, and Jianping Yao. Microwave photonics: Current challenges towards widespread application. *Optics Express*, 21(19):22862, September 2013.

[21] K. Ohata, K. Maruhashi, M. Ito, S. Kishimoto, K. Ikuina, T. Hashiguchi, K. Ikeda, and N. Takahashi. 1.25gbps wireless gigabit ethernet link at 60ghz-band. In *Microwave Symposium Digest, 2003 IEEE MTT-S International*, volume 1, pages 373–376 vol.1, June 2003.

[22] Dengke Zhang, Xue Feng, and Yidong Huang. Simulation of 60-ghz microwave photonic filters based on serially coupled silicon microring resonators. *Chinese Optics Letters*, 10(2):021302, February 2012.

[23] Akihiko Hirata, T. Kosugi, H. Takahashi, R. Yamaguchi, F. Nakajima, T. Furuta, H. Ito, H. Sugahara, Y. Sato, and T. Nagatsuma. 120-ghz-band millimeter-wave photonic wireless link for 10-gb/s data transmission. *IEEE Transactions on Microwave Theory and Techniques*, 54(5):1937–1944, May 2006.

[24] F. Vacondio, M. Mirshafiei, J. Basak, Ansheng Liu, Ling Liao, M. Paniccia, and L.A. Rusch. A Silicon Modulator Enabling RF Over Fiber for 802.11 OFDM Signals. *IEEE Journal of Selected Topics in Quantum Electronics*, 16(1):141–148, January 2010.

[25] Anatol Khilo, Cheryl M. Sorace, and Franz X. Krtner. Broadband linearized silicon modulator. *Optics Express*, 19(5):4485, February 2011.

[26] A.M. Gutierrez, A. Brimont, G. Rasigade, M. Ziebell, D. Marris-Morini, J.-M. Fedeli, L. Vivien, J. Marti, and P. Sanchis. Ring-assisted mach zehnder interferometer silicon modulator for enhanced performance. *Journal of Lightwave Technology*, 30(1):9–14, January 2012.

[27] Jaime Cardenas, Paul A. Morton, Jacob B. Khurgin, Austin Griffith, Carl B. Poitras, Kyle Preston, and Michal Lipson. Linearized silicon modulator based on a ring assisted mach zehnder inteferometer. *Optics Express*, 21(19):22549, September 2013.

[28] Matthew Streshinsky, Ali Ayazi, Zhe Xuan, Andy Eu-Jin Lim, Guo-Qiang

Lo, Tom Baehr-Jones, and Michael Hochberg. Highly linear silicon traveling wave mach-zehnder carrier depletion modulator based on differential drive. *Optics Express*, 21(3):3818, February 2013.

[29] Kevin K. Lee, Desmond R. Lim, Lionel C. Kimerling, Jangho Shin, and Franco Cerrina. Fabrication of ultralow-loss Si/SiO_2 waveguides by roughness reduction. *Optics Letters*, 26(23):1888, December 2001.

[30] P. Dumon, W. Bogaerts, V. Wiaux, J. Wouters, S. Beckx, J. Van Campenhout, D. Taillaert, B. Luyssaert, P. Bienstman, D. Van Thourhout, and R. Baets. Low-loss SOI photonic wires and ring resonators fabricated with deep UV lithography. *IEEE Photonics Technology Letters*, 16(5):1328–1330, May 2004.

[31] W. Bogaerts, R. Baets, P. Dumon, V. Wiaux, S. Beckx, D. Taillaert, B. Luyssaert, J. Van Campenhout, P. Bienstman, and D. Van Thourhout. Nanophotonic waveguides in silicon-on-insulator fabricated with CMOS technology. *Journal of Lightwave Technology*, 23(1):401–412, January 2005.

[32] Tai Tsuchizawa, Koji Yamada, Hiroshi Fukuda, Toshifumi Watanabe, Shingo Uchiyama, and Seiichi Itabashi. Low-Loss Si Wire Waveguides and their Application to Thermooptic Switches. *Japanese Journal of Applied Physics*, 45(8S):6658, August 2006.

[33] Fengnian Xia, Lidija Sekaric, and Yurii Vlasov. Ultracompact optical buffers on a silicon chip. *Nature Photonics*, 1(1):65–71, January 2007.

[34] J. Schmidtchen, A. Splett, B. Schppert, K. Petermann, and G. Burbach. Low loss singlemode optical waveguides with large cross-section in silicon-on-insulator. *Electronics Letters*, 27(16):1486, 1991.

[35] S. Lardenois, D. Pascal, L. Vivien, E. Cassan, S. Laval, R. Orobtchouk, M. Heitzmann, N. Bouzaida, and L. Mollard. Low-loss submicrometer silicon-on-insulator rib waveguides and corner mirrors. *Optics Letters*, 28(13):1150, July 2003.

[36] M. A. Webster, R. M. Pafchek, G. Sukumaran, and T. L. Koch. Low-loss quasi-planar ridge waveguides formed on thin silicon-on-insulator. *Applied Physics Letters*, 87(23):231108, December 2005.

[37] Walid Mathlouthi, Haisheng Rong, and Mario Paniccia. Characterization of efficient wavelength conversion by four-wave mixing in sub-micron silicon waveguides. *Optics Express*, 16(21):16735, October 2008.

[38] Po Dong, Wei Qian, Shirong Liao, Hong Liang, Cheng-Chih Kung, Ning-Ning Feng, Roshanak Shafiiha, Joan Fong, Dazeng Feng, Ashok V. Krishnamoorthy, and Mehdi Asghari. Low loss shallow-ridge silicon waveguides. *Optics Express*, 18(14):14474, July 2010.

[39] Jaime Cardenas, Carl B. Poitras, Jacob T. Robinson, Kyle Preston, Long Chen, and Michal Lipson. Low loss etchless silicon photonic waveguides. *Optics Express*, 17(6):4752, March 2009.

[40] Lian-Wee Luo, Gustavo S. Wiederhecker, Jaime Cardenas, Carl Poitras, and Michal Lipson. High quality factor etchless silicon photonic ring resonators. *Optics Express*, 19(7):6284, March 2011.

[41] Austin Griffith, Jaime Cardenas, Carl B. Poitras, and Michal Lipson. High quality factor and high confinement silicon resonators using etchless process. *Optics Express*, 20(19):21341, September 2012.

[42] Austin G. Griffith, Ryan K. W. Lau, Jaime Cardenas, Yoshitomo Okawachi, Aseema Mohanty, Romy Fain, Yoon Ho Daniel Lee, Mengjie Yu, Christopher T. Phare, Carl B. Poitras, Alexander L. Gaeta, and Michal Lipson. Silicon-chip mid-infrared frequency comb generation. *Nature Communications*, 6, February 2015.

[43] J. Komma, C. Schwarz, G. Hofmann, D. Heinert, and R. Nawrodt. Thermo-optic coefficient of silicon at 1550 nm and cryogenic temperatures. *Applied Physics Letters*, 101(4):041905, July 2012.

[44] Richard A. Soref and B.R. Bennett. Electrooptical effects in silicon. *IEEE Journal of Quantum Electronics*, 23(1):123–129, January 1987.

[45] Hugo L. R. Lira, Sasikanth Manipatruni, and Michal Lipson. Broadband hitless silicon electro-optic switch for on-chip optical networks. *Optics Express*, 17(25):22271, December 2009.

[46] Po Dong, Wei Qian, Hong Liang, Roshanak Shafiiha, Dazeng Feng, Guoliang Li, John E. Cunningham, Ashok V. Krishnamoorthy, and Mehdi Asghari. Thermally tunable silicon racetrack resonators with ultralow tuning power. *Optics Express*, 18(19):20298, September 2010.

[47] Qianfan Xu, Bradley Schmidt, Sameer Pradhan, and Michal Lipson. Micrometre-scale silicon electro-optic modulator. *Nature*, 435(7040):325–327, May 2005.

[48] Qianfan Xu, Sasikanth Manipatruni, Brad Schmidt, Jagat Shakya, and Michal Lipson. 125 Gbit/s carrier-injection-based silicon micro-ring silicon modulators. *Optics Express*, 15(2):430, January 2007.

[49] Ansheng Liu, Ling Liao, Doron Rubin, Hat Nguyen, Berkehan Ciftcioglu, Yoel Chetrit, Nahum Izhaky, and Mario Paniccia. High-speed optical modulation based on carrier depletion in a silicon waveguide. *Optics Express*, 15(2):660, January 2007.

[50] L. Liao, A. Liu, D. Rubin, J. Basak, Y. Chetrit, H. Nguyen, R. Cohen, N. Izhaky, and M. Paniccia. 40 Gbit/s silicon optical modulator for high-speed applications. *Electronics Letters*, 43(22):1196, 2007.

[51] William M. Green, Michael J. Rooks, Lidija Sekaric, and Yurii A. Vlasov. Ultra-compact, low RF power, 10 Gb/s silicon Mach-Zehnder modulator. *Optics Express*, 15(25):17106, 2007.

[52] Qianfan Xu, David Fattal, and Raymond G. Beausoleil. Silicon microring resonators with 1.5-m radius. *Optics Express*, 16(6):4309, March 2008.

[53] Ansheng Liu, Ling Liao, Doron Rubin, Juthika Basak, Yoel Chetrit, Hat Nguyen, Rami Cohen, Nahum Izhaky, and Mario Paniccia. Recent development in a high-speed silicon optical modulator based on reverse-biased pn diode in a silicon waveguide. *Semiconductor Science and Technology*, 23(6):064001, June 2008.

[54] F. Y. Gardes, A. Brimont, P. Sanchis, G. Rasigade, D. Marris-Morini, L. O'Faolain, F. Dong, J. M. Fedeli, P. Dumon, L. Vivien, T. F. Krauss, G. T. Reed, and J. Mart. High-speed modulation of a compact silicon ring resonator based on a reverse-biased pn diode. *Optics Express*, 17(24):21986, November 2009.

[55] Po Dong, Shirong Liao, Dazeng Feng, Hong Liang, Dawei Zheng, Roshanak Shafiiha, Cheng-Chih Kung, Wei Qian, Guoliang Li, Xuezhe Zheng, Ashok V. Krishnamoorthy, and Mehdi Asghari. Low V_pp, ultralow-energy, compact, high-speed silicon electro-optic modulator. *Optics Express*, 17(25):22484, December 2009.

[56] Xi Xiao, Hao Xu, Xianyao Li, Yingtao Hu, Kang Xiong, Zhiyong Li, Tao Chu, Yude Yu, and Jinzhong Yu. 25 Gbit/s silicon microring modulator based on misalignment-tolerant interleaved PN junctions. *Optics Express*, 20(3):2507, January 2012.

[57] G. T. Reed, G. Mashanovich, F. Y. Gardes, and D. J. Thomson. Silicon optical modulators. *Nature Photonics*, 4(8):518–526, August 2010.

[58] Sasikanth Manipatruni, Kyle Preston, Long Chen, and Michal Lipson. Ultra-low voltage, ultra-small mode volume silicon microring modulator. *Optics Express*, 18(17):18235, August 2010.

[59] Po Dong, Roshanak Shafiiha, Shirong Liao, Hong Liang, Ning-Ning Feng, Dazeng Feng, Guoliang Li, Xuezhe Zheng, Ashok V. Krishnamoorthy, and Mehdi Asghari. Wavelength-tunable silicon microring modulator. *Optics Express*, 18(11):10941, May 2010.

[60] Antonio R. Zanatta and Ivan B. Gallo. The Thermo Optic Coefficient of Amorphous SiN Films in the Near-Infrared and Visible Regions and Its Experimental Determination. *Applied Physics Express*, 6(4):042402, April 2013.

[61] Kazuhiro Ikeda, Robert E. Saperstein, Nikola Alic, and Yeshaiahu Fainman. Thermal and Kerr nonlinear properties of plasma-deposited silicon nitride/ silicon dioxide waveguides. *Optics Express*, 16(17):12987, August 2008.

[62] Alexander Gondarenko, Jacob S. Levy, and Michal Lipson. High confinement micron-scale silicon nitride high Q ring resonator. *Optics Express*, 17(14):11366, July 2009.

[63] Jacob S. Levy, Alexander Gondarenko, Mark A. Foster, Amy C. Turner-Foster, Alexander L. Gaeta, and Michal Lipson. CMOS-compatible multiple-wavelength oscillator for on-chip optical interconnects. *Nature Photonics*, 4(1):37–40, January 2010.

[64] Yoshitomo Okawachi, Kasturi Saha, Jacob S. Levy, Y. Henry Wen, Michal Lipson, and Alexander L. Gaeta. Octave-spanning frequency comb generation in a silicon nitride chip. *Optics Letters*, 36(17):3398, September 2011.

[65] Jacob S. Levy, Mark A. Foster, Alexander L. Gaeta, and Michal Lipson. Harmonic generation in silicon nitride ring resonators. *Optics Express*, 19(12):11415, June 2011.

[66] Nicols Sherwood-Droz and Michal Lipson. Scalable 3d dense integration of photonics on bulk silicon. *Optics Express*, 19(18):17758, August 2011.

[67] S.J. Spector, C.M. Sorace, M.W. Geis, M.E. Grein, J.U. Yoon, T.M. Lyszczarz, E.P. Ippen, and F.X. Kartner. Operation and Optimization of Silicon-Diode-Based Optical Modulators. *IEEE Journal of Selected Topics in Quantum Electronics*, 16(1):165–172, January 2010.

[68] Amy C. Turner-Foster, Mark A. Foster, Jacob S. Levy, Carl B. Poitras, Reza Salem, Alexander L. Gaeta, and Michal Lipson. Ultrashort free-carrier lifetime in low-loss silicon nanowaveguides. *Optics Express*, 18(4):3582, February 2010.

[69] F. Y. Gardes, D. J. Thomson, N. G. Emerson, and G. T. Reed. 40 Gb/s silicon photonics modulator for TE and TM polarisations. *Optics Express*, 19(12):11804, June 2011.

[70] D.J. Thomson, F.Y. Gardes, J.-M. Fedeli, S. Zlatanovic, Youfang Hu, B.P.P. Kuo, E. Myslivets, N. Alic, S. Radic, G.Z. Mashanovich, and G.T. Reed. 50-Gb/s Silicon Optical Modulator. *IEEE Photonics Technology Letters*, 24(4):234–236, February 2012.

[71] Po Dong, Long Chen, and Young-kai Chen. High-speed low-voltage single-drive push-pull silicon Mach-Zehnder modulators. *Optics Express*, 20(6):6163, March 2012.

[72] Mark Y. Liu and Stephen Y. Chou. High modulation depth and short cavity length silicon FabryPerot modulator with two grating Bragg reflectors. *Applied Physics Letters*, 68(2):170–172, January 1996.

[73] Takasumi Tanabe, Masaya Notomi, Satoshi Mitsugi, Akihiko Shinya, and Eiichi Kuramochi. All-optical switches on a silicon chip realized using photonic crystal nanocavities. *Applied Physics Letters*, 87(15):151112, October 2005.

[74] Mohammad Soltani, Siva Yegnanarayanan, and Ali Adibi. Ultra-high Q planar silicon microdisk resonators for chip-scale silicon photonics. *Optics Express*, 15(8):4694, 2007.

[75] M. Soltani, S. Yegnanarayanan, Qing Li, and A. Adibi. Systematic Engineering of Waveguide-Resonator Coupling for Silicon Microring/Microdisk/Racetrack Resonators: Theory and Experiment. *IEEE Journal of Quantum Electronics*, 46(8):1158–1169, August 2010.

[76] Michael R. Watts, William A. Zortman, Douglas C. Trotter, Ralph W.

Young, and Anthony L. Lentine. Vertical junction silicon microdisk modulators and switches. *Optics Express*, 19(22):21989, October 2011.

[77] Joshua N. Winn, Shanhui Fan, John D. Joannopoulos, and Erich P. Ippen. Interband transitions in photonic crystals. *Physical Review B*, 59(3):1551–1554, January 1999.

[78] Zongfu Yu and Shanhui Fan. Complete optical isolation created by indirect interband photonic transitions. *Nature Photonics*, 3(2):91–94, February 2009.

[79] Zongfu Yu and Shanhui Fan. Optical isolation based on nonreciprocal phase shift induced by interband photonic transitions. *Applied Physics Letters*, 94(17):171116, April 2009.

[80] Hwi Kim and Byoungho Lee. Efficient frequency conversion in slab waveguide by cascaded nonreciprocal interband photonic transitions. *Optics Letters*, 35(19):3165, October 2010.

[81] Hugo Lira, Zongfu Yu, Shanhui Fan, and Michal Lipson. Electrically Driven Nonreciprocity Induced by Interband Photonic Transition on a Silicon Chip. *Physical Review Letters*, 109(3):033901, July 2012.

[82] Zongfu Yu and Shanhui Fan. Photonic Transition in Nanophotonics. In Zhigang Chen and Roberto Morandotti, editors, *Nonlinear Photonics and Novel Optical Phenomena*, number 170 in Springer Series in Optical Sciences, pages 343–364. Springer New York, 2012.

[83] Michel Castellanos Muoz, Alexander Y. Petrov, Liam OFaolain, Juntao Li, Thomas F. Krauss, and Manfred Eich. Indirect transitions of a signal interacting with a moving refractive index front. In *SPIE Photonics Europe*, pages 913606–913606. International Society for Optics and Photonics, 2014.

[84] Michel Castellanos Muoz, Alexander Yu Petrov, Liam OFaolain, Juntao Li, Thomas F. Krauss, and Manfred Eich. Optically induced indirect photonic transitions in a slow light photonic crystal waveguide. *Physical review letters*, 112(5):053904, 2014.

[85] C. Monroe, D. M. Meekhof, B. E. King, and D. J. Wineland. A Schrdinger Cat Superposition State of an Atom. *Science*, 272(5265):1131–1136, May 1996.

[86] Po Dong, Stefan F. Preble, Jacob T. Robinson, Sasikanth Manipatruni, and Michal Lipson. Inducing Photonic Transitions between Discrete Modes in a Silicon Optical Microcavity. *Physical Review Letters*, 100(3):033904, January 2008.

[87] Richard L. Espinola, Jerry I. Dadap, Richard M. Osgood, Jr., Sharee J. McNab, and Yurii A. Vlasov. C-band wavelength conversion in silicon photonic wire waveguides. *Optics Express*, 13(11):4341, 2005.

[88] Haisheng Rong, Ying-Hao Kuo, Ansheng Liu, Mario Paniccia, and Oded Cohen. High efficiency wavelength conversion of 10 Gb/s data in silicon waveguides. *Optics Express*, 14(3):1182, 2006.

[89] Ying-Hao Kuo, Haisheng Rong, Vanessa Sih, Shengbo Xu, Mario Paniccia, and Oded Cohen. Demonstration of wavelength conversion at 40 Gb/s data rate in silicon waveguides. *Optics Express*, 14(24):11721, 2006.

[90] Amy C. Turner, Mark A. Foster, Alexander L. Gaeta, and Michal Lipson. Ultra-low power parametric frequency conversion in a silicon microring resonator. *Optics Express*, 16(7):4881, March 2008.

[91] Amy C. Turner-Foster, Mark A. Foster, Reza Salem, Alexander L. Gaeta, and Michal Lipson. Frequency conversion over two-thirds of an octave in silicon nanowaveguides. *Optics Express*, 18(3):1904, February 2010.

[92] J. Fujita, M. Levy, R. M. Osgood Jr, L. Wilkens, and H. Dtsch. Waveguide optical isolator based on MachZehnder interferometer. *Applied Physics Letters*, 76(16):2158–2160, April 2000.

[93] Richard L. Espinola, Tomoyuki Izuhara, Ming-Chun Tsai, Richard M. Osgood, Jr., and Horst Dtsch. Magneto-optical nonreciprocal phase shift in garnet/silicon-on-insulator waveguides. *Optics Letters*, 29(9):941, 2004.

[94] Horst Dtsch, Norbert Bahlmann, Oleksandr Zhuromskyy, Manfred Hammer, Ludger Wilkens, Reinald Gerhardt, Peter Hertel, and Anatoly F. Popkov. Applications of magneto-optical waveguides in integrated optics: review. *Journal of the Optical Society of America B*, 22(1):240, 2005.

[95] Yuya Shoji, Tetsuya Mizumoto, Hideki Yokoi, I.-Wei Hsieh, and Richard M. Osgood Jr. Magneto-optical isolator with silicon waveguides fabricated by direct bonding. *Applied Physics Letters*, 92(7):071117, February 2008.

[96] Ming-Chun Tien, Tetsuya Mizumoto, Paolo Pintus, Herbert Kromer, and John E. Bowers. Silicon ring isolators with bonded nonreciprocal magneto-optic garnets. *Optics Express*, 19(12):11740, June 2011.

[97] Lei Bi, Juejun Hu, Peng Jiang, Dong Hun Kim, Gerald F. Dionne, Lionel C. Kimerling, and C. A. Ross. On-chip optical isolation in monolithically integrated non-reciprocal optical resonators. *Nature Photonics*, 5(12):758–762, December 2011.

[98] S. Ghosh, S. Keyvavinia, W. Van Roy, T. Mizumoto, G. Roelkens, and R. Baets. Ce:YIG/Silicon-on-Insulator waveguide optical isolator realized by adhesive bonding. *Optics Express*, 20(2):1839, January 2012.

[99] A. E. Kaplan and P. Meystre. Enhancement of the Sagnac effect due to nonlinearly induced nonreciprocity. *Optics Letters*, 6(12):590, December 1981.

[100] Katia Gallo, Gaetano Assanto, Krishnan R. Parameswaran, and Martin M. Fejer. All-optical diode in a periodically poled lithium niobate waveguide. *Applied Physics Letters*, 79(3):314–316, July 2001.

[101] Victor Grigoriev and Fabio Biancalana. Nonreciprocal switching thresholds in coupled nonlinear microcavities. *Optics Letters*, 36(11):2131, June 2011.

[102] M. S. Kang, A. Butsch, and P. St J. Russell. Reconfigurable light-driven opto-acoustic isolators in photonic crystal fibre. *Nature Photonics*, 5(9):549–553, September 2011.

[103] Li Fan, Jian Wang, Leo T. Varghese, Hao Shen, Ben Niu, Yi Xuan, Andrew M. Weiner, and Minghao Qi. An All-Silicon Passive Optical Diode. *Science*, 335(6067):447–450, January 2012.

[104] Christopher R. Doerr, Nicolas Dupuis, and Liming Zhang. Optical isolator using two tandem phase modulators. *Optics Letters*, 36(21):4293, November 2011.

[105] Dimitrios L. Sounas, Christophe Caloz, and Andrea Al. Giant nonreciprocity at the subwavelength scale using angular momentum-biased metamaterials. *Nature Communications*, 4, September 2013.

[106] C. R. Doerr, L. Chen, and D. Vermeulen. Silicon photonics broadband modulation-based isolator. *Optics Express*, 22(4):4493, February 2014.

[107] Yisu Yang, Christophe Galland, Yang Liu, Kang Tan, Ran Ding, Qi Li, Keren Bergman, Tom Baehr-Jones, and Michael Hochberg. Experimental demonstration of broadband Lorentz non-reciprocity in an integrable photonic architecture based on Mach-Zehnder modulators. *Optics Express*, 22(14):17409, July 2014.

[108] Po Dong. Travelling-wave Mach-Zehnder modulators functioning as optical isolators. *Optics Express*, 23(8):10498, April 2015.

[109] Hermann A. Haus. *Waves and fields in optoelectronics*. Prentice Hall, Incorporated, 1984.

[110] R. C. Williamson. Sensitivitybandwidth product for electro-optic modulators. *Optics Letters*, 26(17):1362, September 2001.

[111] Wesley D. Sacher and Joyce K. S. Poon. Dynamics of microring resonator modulators. *Optics Express*, 16(20):15741, September 2008.

[112] Benjamin G. Lee, Benjamin A. Small, Keren Bergman, Qianfan Xu, and Michal Lipson. Transmission of high-data-rate optical signals through a micrometer-scale silicon ring resonator. *Optics Letters*, 31(18):2701, 2006.

[113] J. Cardenas, C.B. Poitras, K. Luke, Lian-Wee Luo, P.A. Morton, and M. Lipson. High Coupling Efficiency Etched Facet Tapers in Silicon Waveguides. *IEEE Photonics Technology Letters*, 26(23):2380–2382, December 2014.

[114] Lawrence D. Tzuang, Mohammad Soltani, Yoon Ho Daniel Lee, and Michal Lipson. High RF carrier frequency modulation in silicon resonators by coupling adjacent free-spectral-range modes. *Optics Letters*, 39(7):1799, April 2014.

[115] W.D. Sacher and J.K.S. Poon. Characteristics of Microring Resonators With Waveguide-Resonator Coupling Modulation. *Journal of Lightwave Technology*, 27(17):3800–3811, September 2009.

[116] Wesley D. Sacher, William M. Green, Solomon Assefa, Tymon Barwicz, Steven M. Shank, Yurii A. Vlasov, and Joyce Poon. Controlled Coupling in Silicon Microrings for High-Speed, High Extinction Ratio, and Low-Chirp Modulation. page PDPA8. OSA, 2011.

[117] W. D. Sacher, W. M. J. Green, S. Assefa, T. Barwicz, H. Pan, S. M. Shank, Y. A. Vlasov, and J. K. S. Poon. Coupling modulation of microrings at rates beyond the linewidth limit. *Optics Express*, 21(8):9722, April 2013.

[118] K. Y. Lau. Efficient narrowband direct modulation of semiconductor injection lasers at millimeter wave frequencies of 100 GHz and beyond. *Applied Physics Letters*, 52(26):2214–2216, June 1988.

[119] Kam Y. Lau. Narrow-band modulation of semiconductor lasers at millimeter wave frequencies (gt;100 GHz) by mode locking. *IEEE Journal of Quantum Electronics*, 26(2):250–261, February 1990.

[120] Vladimir S. Ilchenko, Anatoliy A. Savchenkov, Andrey B. Matsko, and Lute Maleki. Whispering-gallery-mode electro-optic modulator and photonic microwave receiver. *Journal of the Optical Society of America B*, 20(2):333, 2003.

[121] Mani Hossein-Zadeh and Anthony F. J. Levi. A new electrode design for microdisk electro-optic RF modulator. In *Conference on Lasers and Electro-Optics/Quantum Electronics and Laser Science Conference (2003), paper CTuW3*, page CTuW3. Optical Society of America, June 2003.

[122] J.P. Reithmaier, W. Kaiser, L. Bach, A. Forchel, V. Feies, M. Gioannini, I. Montrosset, T.W. Berg, and B. Tromborg. Modulation speed enhancement by coupling to higher order resonances: a road towards 40 GHz bandwidth lasers on InP. In *International Conference on Indium Phosphide and Related Materials, 2005*, pages 118–123, May 2005.

[123] M. Hossein-Zadeh and A.F.J. Levi. Ring resonator-based photonic microwave receiver modulator with picowatt sensitivity. *IET Optoelectronics*, 5(1):36–39, February 2011.

[124] Brian A. Daniel, Drew N. Maywar, and Govind P. Agrawal. Dynamic mode theory of optical resonators undergoing refractive index changes. *Journal of the Optical Society of America B*, 28(9):2207, September 2011.

[125] Ali W. Elshaari and Stefan F. Preble. Engineered Transitions in Photonic Cavities. *Optics and Photonics Journal*, 02(04):255–259, 2012.

[126] Mohammad Soltani, Qing Li, Siva Yegnanarayanan, and Ali Adibi. Toward ultimate miniaturization of high Q silicon traveling-wave microresonators. *Optics Express*, 18(19):19541, September 2010.

[127] Kejie Fang, Zongfu Yu, and Shanhui Fan. Photonic Aharonov-Bohm Effect Based on Dynamic Modulation. *Physical Review Letters*, 108(15):153901, April 2012.

[128] Kejie Fang, Zongfu Yu, and Shanhui Fan. Realizing effective magnetic field for photons by controlling the phase of dynamic modulation. *Nature Photonics*, 6(11):782–787, November 2012.

[129] Qian Lin and Shanhui Fan. Light Guiding by Effective Gauge Field for Photons. *Physical Review X*, 4(3):031031, August 2014.

[130] Luqi Yuan and Shanhui Fan. Dynamic localization of light from a time-dependent effective gauge field for photons. *arXiv:1502.06037 [physics]*, February 2015. arXiv: 1502.06037.

[131] Y. Aharonov and D. Bohm. Significance of Electromagnetic Potentials in the Quantum Theory. *Physical Review*, 115(3):485–491, August 1959.

[132] Norman F. Ramsey. A New Molecular Beam Resonance Method. *Physical Review*, 76(7):996–996, October 1949.

[133] N. F. Ramsey. Molecular beams. January 1985.

[134] Ch J. Bord. Atomic interferometry with internal state labelling. *Physics letters A*, 140(1):10–12, 1989.

[135] B. Dubetsky and M. A. Kasevich. Atom interferometer as a selective sensor of rotation or gravity. *Physical Review A*, 74(2):023615, August 2006.

[136] K. Kobayashi and M. Seki. Microoptic grating multiplexers and optical isolators for fiber-optic communications. *IEEE Journal of Quantum Electronics*, 16(1):11–22, January 1980.

[137] Kejie Fang, Zongfu Yu, and Shanhui Fan. Experimental demonstration of a photonic Aharonov-Bohm effect at radio frequencies. *Physical Review B*, 87(6):060301, February 2013.

[138] Enbang Li, Benjamin J. Eggleton, Kejie Fang, and Shanhui Fan. Photonic AharonovBohm effect in photonphonon interactions. *Nature Communications*, 5, January 2014.

[139] Lawrence D. Tzuang, Kejie Fang, Paulo Nussenzveig, Shanhui Fan, and Michal Lipson. Non-reciprocal phase shift induced by an effective magnetic flux for light. *Nature Photonics*, 8(9):701–705, September 2014.

[140] Zheng Wang, Y. D. Chong, John D. Joannopoulos, and Marin Soljai. Reflection-Free One-Way Edge Modes in a Gyromagnetic Photonic Crystal. *Physical Review Letters*, 100(1):013905, January 2008.

[141] S. Raghu and F. D. M. Haldane. Analogs of quantum-Hall-effect edge states in photonic crystals. *Physical Review A*, 78(3):033834, September 2008.

[142] Zheng Wang, Yidong Chong, J. D. Joannopoulos, and Marin Soljai. Observation of unidirectional backscattering-immune topological electromagnetic states. *Nature*, 461(7265):772–775, October 2009.

[143] Yin Poo, Rui-xin Wu, Zhifang Lin, Yan Yang, and C. T. Chan. Experimental Realization of Self-Guiding Unidirectional Electromagnetic Edge States. *Physical Review Letters*, 106(9):093903, March 2011.

[144] M. Patterson, S. Hughes, S. Combri, N.-V.-Quynh Tran, A. De Rossi, R. Gabet, and Y. Jaoun. Disorder-Induced Coherent Scattering in Slow-Light Photonic Crystal Waveguides. *Physical Review Letters*, 102(25):253903, June 2009.

[145] F. Morichetti, A. Canciamilla, M. Martinelli, A. Samarelli, R. M. De La Rue, M. Sorel, and A. Melloni. Coherent backscattering in optical microring resonators. *Applied Physics Letters*, 96(8):081112, February 2010.

[146] R. O. Umucallar and I. Carusotto. Artificial gauge field for photons in coupled cavity arrays. *Physical Review A*, 84(4):043804, October 2011.

[147] Mohammad Hafezi, Eugene A. Demler, Mikhail D. Lukin, and Jacob M. Taylor. Robust optical delay lines with topological protection. *Nature Physics*, 7(11):907–912, November 2011.

[148] Mikael C. Rechtsman, Julia M. Zeuner, Yonatan Plotnik, Yaakov Lumer, Daniel Podolsky, Felix Dreisow, Stefan Nolte, Mordechai Segev, and Alexander Szameit. Photonic Floquet topological insulators. *Nature*, 496(7444):196–200, April 2013.

[149] Stefano Longhi. Effective magnetic fields for photons in waveguide and coupled resonator lattices. *Optics letters*, 38(18):3570–3573, 2013.

[150] G. Q. Liang and Y. D. Chong. Optical Resonator Analog of a Two-Dimensional Topological Insulator. *Physical Review Letters*, 110(20):203904, May 2013.

[151] Alexander B. Khanikaev, S. Hossein Mousavi, Wang-Kong Tse, Mehdi Kargarian, Allan H. MacDonald, and Gennady Shvets. Photonic topological insulators. *Nature Materials*, 12(3):233–239, March 2013.

[152] Yong-qing Li and Min Xiao. Electromagnetically induced transparency in a three-level Λ{}-type system in rubidium atoms. *Physical Review A*, 51(4):R2703–R2706, April 1995.

[153] Mehmet Fatih Yanik, Wonjoo Suh, Zheng Wang, and Shanhui Fan. Stopping Light in a Waveguide with an All-Optical Analog of Electromagnetically Induced Transparency. *Physical Review Letters*, 93(23):233903, December 2004.

[154] Qianfan Xu, Sunil Sandhu, Michelle L. Povinelli, Jagat Shakya, Shanhui Fan, and Michal Lipson. Experimental Realization of an On-Chip All-Optical Analogue to Electromagnetically Induced Transparency. *Physical Review Letters*, 96(12):123901, March 2006.

[155] Mian Zhang, Gustavo S. Wiederhecker, Sasikanth Manipatruni, Arthur Barnard, Paul McEuen, and Michal Lipson. Synchronization of Micromechanical Oscillators Using Light. *Physical Review Letters*, 109(23):233906, December 2012.

[156] Xiankai Sun, King Y. Fong, Chi Xiong, Wolfram H. P. Pernice, and Hong X. Tang. GHz optomechanical resonators with high mechanical Q factor in air. *Optics Express*, 19(22):22316, October 2011.

[157] Yurii A. Vlasov, Martin O'Boyle, Hendrik F. Hamann, and Sharee J. McNab. Active control of slow light on a chip with photonic crystal waveguides. *Nature*, 438(7064):65–69, November 2005.

[158] Kejie Fang and Shanhui Fan. Controlling the Flow of Light Using the Inhomogeneous Effective Gauge Field that Emerges from Dynamic Modulation. *Physical Review Letters*, 111(20):203901, November 2013.